ROYAUME DU MAROC
Université Mohammed V
- RABAT -
جامعة محمد الخامس
- الرباط -
Faculté des sciences
كلية العلوم

CENTRE D'ETUDES DOCTORALES - SCIENCES ET TECHNOLOGIES

N° d'ordre : 3870

THESE

En vue de l'obtention du : ***DOCTORAT***

Structure de Recherche : *Laboratoire de Recherche en Informatique et Télécommunications*
Discipline : *Sciences de l'ingénieur*
Spécialité : *Informatique et Télécommunications*

Présentée et soutenue le 02 /12 /2023 par :

HANAE BELMAJOUB

Artificial Intelligence Techniques for Automatic Segmentation and Characterization of the Coastal Upwelling System

JURY

Moulay Driss RAHMANI	PES, Université Mohammed V, Faculté des Sciences- Rabat.	President
Abdellah ADIB	PES, Université Hassan II, Faculté des Sciences et Techniques- Mohammadia	Rapporteur/ Examinateur
Ahmed DRISSI EL MALIANI	PH, Université Mohammed V, Faculté des Sciences- Rabat.	Rapporteur/ Examinateur
Hicham LAANAYA	PH, Université Mohammed V, Faculté des Sciences- Rabat.	Rapporteur/ Examinateur
Salma MOULINE	PES, Université Mohammed V, Faculté des Sciences- Rabat.	Examinateur
Anass EL AOUNI	CR, Mercator Océan International, Toulouse, France	Invité
Khalid MINAOUI	PES, Université Mohammed V, Faculté des Sciences- Rabat.	Directeur de Thèse

Année Universitaire : 2023-2024

✉ Faculté des Sciences, avenue Ibn Battouta, BP. 1014 RP, Rabat –Maroc
☎ 00212 (05) 37 77 18 76 📠 00212(05) 37 77 42 61; http://www. fsr.um5.ac.ma

DEDICACE

I am incredibly grateful to all my friends for your support. Your camaraderie and encouragement have been constant sources of motivation and inspiration. Our stimulating discussions, diverse perspectives, and shared aspirations have greatly enhanced the quality and depth of my work.

I would not have made it this far without the support of my family, and deserves endless gratitude: I am deeply grateful to my Mom Badia and Dad Abdelfettah for their unwavering love, support, and encouragement throughout my academic journey. Their sacrifices, guidance, and belief in me have been instrumental in reaching this milestone. Their constant presence and words of wisdom have motivated me to overcome challenges and pursue my aspirations. I am truly fortunate to have such exceptional parents who have shaped me into the person I am today. Thank you for being my pillars of strength and for instilling in me the values of perseverance and dedication.

I would like to express my sincere gratitude to my sisters Hanane and Oumaima, my brother-in-law Atman, and my friend Lamyae for their constant support and encouragement throughout my studies. Their unwavering faith in my abilities and their words of motivation has been a constant source of inspiration. Their presence in my life gave me a sense of belonging and reminded me of the importance of family. Thank you for always being there. Your love and encouragement have had significant impact on my journey, and I am truly grateful to have such wonderful sisters and brother.

My wonderful nephew Jadou, who affectionately calls me ”KaKi”. Your luminous presence in my life brings me boundless joy and inspiration. Your innocent laugh and endearing nickname remind me of the beauty of simplicity and the importance of cherishing every moment. Thank you for being a constant source of happiness and for reminding me of the true essence of love and innocence.

ACKNOWLEDGEMENTS

This PhD thesis has been prepared within the laboratory of research in computer science and telecommunications (LRIT) at the Faculty of Sciences of Mohammed V University in Rabat under the supervision and direction of Professor **Khalid MINAOUI**.

I am immensely grateful to my thesis supervisor, Mr. **Khalid MINAOUI**, Professor of Higher Education (PES) at the Faculty of Sciences, Mohammed V University, Rabat, for his efforts, support, trust, dedicated guidance, and invaluable advice throughout my PhD journey. No words can adequately convey or express the depth of my gratitude for all he has done. His depth of expertise, breadth of knowledge, thoughtful advice, and encouragement have not only shaped the trajectory of my research but have also been instrumental in bringing this work to fruition. I consider myself incredibly fortunate to have had such an exceptional mentor, and I am truly grateful to him not only for his contributions to my academic development but also for being a source of inspiration and guidance. Thank you for everything.

It is with the utmost honor and profound gratitude that I extend my sincere appreciation to Mr. **Moulay Driss RAHMANI**, PES at the Faculty of Sciences Rabat, for graciously agreeing to preside over my thesis committee.

I would like to express my deep gratitude to Mr. **Abdellah ADIB**, PES at the Faculty of Science and Technology of Mohammedia, for generously accepting to report, evaluate, and provide valuable feedback on this thesis.

I would also like to extend my gratitude to Mr. EL MALIANI DRISSI Ahmed, Accredited Professor (PH) at the Faculty of Sciences, Rabat, for agreeing to report this thesis and for taking the time to meticulously evaluate this work.

My thanks also go to Mr. **Hicham LAANAYA** PH at the Faculty of Sciences, Rabat, for graciously accepting to report my thesis. I am grateful for his detailed examination and the time he dedicated to evaluating this work.

I would like to extend a special and heartfelt thank you to Mme. **Salma MOULINE**, PES at the Faculty of Sciences Rabat, who not only agreed to examine

my thesis but who has also been a remarkable source of learning and inspiration throughout my academic career. Your mentorship has been instrumental and I am privileged to have had you as my teacher.

I would like to express my gratitude to Mr. **Anass EL AOUNI**, Research Manager at Mercator Ocean International, France, for his considerable efforts in guiding me through my thesis. I am grateful to him for the discussions we had, which greatly enriched my understanding of the subject. His willingness to share his knowledge and provide valuable information, explanations, and thoughtful insights into the field were instrumental in guiding my research. Thank you very much.

I would like to express my deep gratitude and sincere thanks to the exceptional team of innovative students (”Younes, Sami, Youssef, Othmane, Anass, Ayoub, and Houda”) with whom I have had the privilege of collaborating on various competitions and projects. Each and every one of you played a key role in my discovery of the fascinating world of inventions and innovations. The experiences shared, the challenges met and the successes celebrated together have been a constant source of inspiration and enrichment for me. A special tribute to my thesis supervisor, for it was thanks to him that I was able to discover and enter this field. I'm also grateful to Professor Bekali Karfa Younes, with whom we worked closely. His sound advice and expertise contributed greatly to the achievement of our objectives.

I would like to take this opportunity to express my gratitude to the entire teaching staff of the LRIT for the quality of the training I have received, and their passion for research, which they have provided throughout my years of study.

ABSTRACT

Analyzing the physical processes within an upwelling system is pivotal for comprehending its current variability as well as its past and future developments. This natural phenomenon, modulated by dynamic variables, is integral to regulating oceanic conditions and maintaining vital marine resources. Concurrently, advancements in artificial intelligence and signal processing are forging new paths for a more precise and efficient understanding, monitoring, and management of upwelling systems. This thesis introduces interdisciplinary research centered on the automatic detection of upwelling systems. It leverages image and signal processing and utilizes diverse data from various satellite sources. The goals of this study include: (1) Enhancing the automatic identification and extraction of the upwelling phenomenon along the Moroccan Atlantic coast. This is achieved by applying artificial intelligence algorithms to biological and physical satellite data. (2) Employing deep learning to monitor coastal upwelling in different areas, utilizing satellite images of sea surface temperature (SST). (3) Conducting statistical analysis on the spatio-temporal variation of upwelling in the North West Africa (NWA) region. This involves proposing and scrutinizing various new indices associated with upwelling. This research aims to amalgamate insights from oceanography, artificial intelligence, image processing, and signal processing to foster a comprehensive understanding of upwelling systems and their multifaceted impacts.

keywords: Upwelling system, Image processing, Artificial intelligence, Moroccan Atlantic coast, Automatic extraction of the upwelling, Sea surface temperature, Signal processing, New indices.

RÉSUMÉ

L'analyse des processus physiques au sein d'un système d'upwelling est essentielle pour comprendre sa variabilitè actuelle ainsi que ses évolutions passées et futures. Ce phénomène naturel, modulé par des variables dynamiques, fait partie intégrante de la régulation des conditions océaniques et du maintien des ressources marines vitales. Parallèlement, les progrès de l'intelligence artificielle et du traitement des signaux ouvrent de nouvelles voies pour une compréhension, une surveillance et une gestion plus prècises et plus efficaces des systèmes de remontée d'eau. Cette thèse présente une recherche interdisciplinaire centrée sur la détection automatique des systèmes de remontée d'eau. Elle s'appuie sur le traitement des images et des signaux et utilise diverses données provenant de différentes sources satellitaires. Les objectifs de cette étude sont les suivants: (1) Améliorer l'identification automatique et l'extraction du phénomène de remontée des eaux le long de la côte atlantique marocaine. Pour ce faire, des algorithmes d'intelligence artificielle sont appliqués à des données satellitaires biologiques et physiques. (2) L'utilisation de l'apprentissage profond pour surveiller l'upwelling côtier dans différentes zones, en utilisant des images satellitaires de la température de surface de la mer (SST). (3) Réalisation d'une analyse statistique sur la variation spatio-temporelle de la remontée des eaux dans la région de l'Afrique du Nord-Ouest (NWA). Cela implique de proposer et d'examiner divers nouveaux indices associés à l'upwelling. Cette recherche vise à fusionner les connaissances de l'océanographie, de l'intelligence artificielle, du traitement des images et du traitement des signaux pour favoriser une compréhension globale des systèmes d'upwelling et de leurs impacts à multiples facettes.

Mots clés: Système d'upwelling, Traitement de l'image, Intelligence artificielle, côte atlantique Marocaine, Extraction automatique de l'upwelling, température de surface de la mer, Traitement du signal, Nouveaux Indices.

RÉSUMÉ DÉTAILLÉ

Une exploration des phénomènes océanographiques requiert une compréhension approfondie de la dynamique et de la circulation des océans. Cette compréhension repose sur ,l'analyse des multiples mécanismes à l'œuvre dans les océans. Parmi les missions cruciales des océanographes figure l'étude des systèmes d'upwelling le long des côtes marines. L'upwelling côtier se caractérise par une remontée d'eaux profondes depuis le plateau continental, compensant ainsi la dérive des eaux de surface vers le large, grâce à l'effet conjugué du vent favorable et de la rotation de la Terre, notamment la force de Coriolis.

Cette ascension des eaux froides le long des côtes s'accompagne généralement d'une richesse en nutriments, ce qui stimule naturellement le processus de photosynthèse dans la couche euphotique. Ces systèmes engendrent des structures océaniques puissantes susceptibles d'influencer significativement la distribution de la couche euphotique, créant ainsi des fluctuations notables dans les ressources halieutiques. En fait, il est important de noter que près de 25% des captures mondiales de poissons proviennent des quatre principaux courants d'écosystèmes d'upwelling, à savoir le courant des Canaries, le courant du Benguela, le courant du Humboldt et le courant de la Californie. Ces courants couvrent plus de 5% de la surface totale des océans.

La détection et l'analyse de l'upwelling revêtent une importance économique significative, étant donné qu'ils constituent la principale source d'enrichissement des écosystèmes côtiers. Face à la limitation et à la discontinuité des mesures in-situ, le traitement d'image satellitaire s'avère une ressource cruciale pour mettre en évidence les structures méso-échelles caractéristiques des zones d'upwelling.

Bien que plusieurs méthodes de traitement d'images classiques existent pour extraire et identifier les zones d'upwelling, elles se heurtent souvent à des difficultés lors de l'identification des remontées d'eau. Toutefois, dans ce contexte, les avancées technologiques en matière d'intelligence artificielle ouvrent de nouvelles perspectives pour une compréhension ,une délimitation, une surveillance et une gestion plus précises et efficaces de l'upwelling.

Cette thèse se concentre spécifiquement sur l'upwelling d'Afrique du Nord-Ouest, et propose une étude interdisciplinaire portant sur la détection automatique des systèmes d'upwelling, en s'appuyant sur le traitement des images et des signaux et en exploitant diverses données provenant de sources satellitaires variées. Cette thèse explore plusieurs aspects, notamment:

- Améliorer l'identification et l'extraction automatique du phénomène d'upwelling le long de la côte atlantique Marocaine, en recourant à des algorithmes d'intelligence artificielle appliqués aux données satellitaires biologiques et physiques.

- Identifier et surveiller les remontées d'eaux côtières dans différentes zones littorales à l'aide de l'apprentissage profond, en utilisant des images satellitaires de la température de surface de la mer.

- Effectuer une analyse statistique de la variation spatio-temporelle de l'upwelling dans la région de la NWA (Nord-Ouest de l'Afrique), en proposant et examinant différents nouveaux indices associés à l'upwelling.

Le premier chapitre de cette thèse débute par une exposition de la physique fondamentale sous-tendant l'upwelling côtier. Il aborde également les divers mécanismes et indicateurs intervenant dans le processus d'upwelling, les réponses écologiques aux événements d'upwelling côtier, l'identification des principaux écosystèmes d'upwelling, ainsi que l'introduction des données utilisées tout au long de cette thèse.

Le deuxième chapitre commence par présenter les méthodes conventionnelles couramment employées pour traiter les images en vue de segmenter les régions d'upwelling à partir des données de température de surface de la mer (SST) et de concentration de chlorophylle (CHL-a). En outre, il passe en revue les approches précédemment élaborées pour la détection de l'upwelling le long des côtes marocaines, en décrivant les avantages et les limites associés à chacune de ces méthodes. Par la suite, nous exploitons les capacités des réseaux neuronaux profonds et des algorithmes d'apprentissage automatique de pointe afin d'améliorer la précision, l'efficacité et la robustesse de la détection des remontées d'eau.

Le troisième chapitre presente de nouvelles techniques d'apprentissage profond visant à surveiller et à améliorer l'identification des régions de remontée d'eau à l'aide de données satellitaires physiques et biologiques. Composé de trois contributions distinctes, ce chapitre débute par la mise en œuvre d'une architecture de réseau neuronal convolutif (CNN) personnalisée, inspirée de la conception U-Net. Cette technique se concentre sur la détection précise et la localisation exacte des régions de remontée d'eau dans des zones géographiques désignées. Par la suite, une stratégie de raffinement impliquant des réseaux résiduels profonds (ResNets) est introduite, améliorant encore la précision de la détection des remontées d'eau sous le nom de "DeepRes-UpwellNet". Enfin, le chapitre se conclut par l'introduction de "DeepCoast$_{up}$-Net", une architecture conųe pour l'identification complète des régions de remontée d'eau dans les principales zones côtières, exploitant efficacement le potentiel de l'imagerie satellitaire SST.

Le suivi temporel de l'upwelling à partir de données satellitaires constitue une tâche complexe et exigeante, nécessitant l'analyse systématique d'images quotidiennes, voire hebdomadaires. Pour rendre cette surveillance plus opérationnelle et efficiente, diverses méthodes, qu'elles soient simples ou sophistiquées, ont été élaborées pour synthétiser la localisation de l'upwelling le long de la côte sur une période donnée. La majorité de ces méthodes repose sur l'utilisation d'indices basés sur les différences de température entre les eaux côtières et les eaux en pleine mer.

Le quatrième chapitre de cette thèse entreprend une étude complete de l'activité d'upwelling le long de la côte atlantique marocaine. Il débute par un examen approfondi des indices établis et largement reconnus dans la littérature, conųs pour analyser de manière quantitative les fluctuations saisonnières et interannuelles de la dynamique de l'upwelling. Ensuite, en s'appuyant sur la technique d'extraction de l'upwelling, un nouvel indice d'upwelling est formulé, basé sur les images de la température de surface de la mer. Cet indice présente plusieurs avantages par rapport à ses prédécesseurs, notamment en termes de simplicité, d'efficacité et de précision dans les calculs, dans le but de fournir une compréhension plus détaillée de la dynamique de la remontée des eaux dans cette région. De plus, en utilisant ce nouvel indice proposé comme base, une étude complète sera menée pour examiner les variations spatio-temporelles de la dynamique de la remontée des eaux au Maroc. Enfin, en se fondant sur la méthode d'extraction de l'upwelling présentée dans le troisième chapitre, deux indices additionnels seront développés en utilisant conjointement les images de la température de surface de la mer et de la concentration de chlorophylle. Une étude comparative approfondie basée sur ces indices sera ensuite présentée.

ACRONYMS

AVHRR : Advanced Very High Resolution Radiometer

BN : Batch Normalization.

CCMP : Cross-Calibrated Multi-Platform.

CCUS : Current Upwelling System.

CHLa : Chlorophyll-a.

CNN: Convolutional Neural Network.

CSET : Cross-Shore Ekman Transport.

CUI : Coastal Upwelling Index.

DC : Dice Coefficient.

EBCUS : Eastern Boundary Current upwelling Systems.

FCM : Fuzzy C-Means.

FCN : Fully Convolutional Network.

GHRSST : Group for High Resolution Sea Surface Temperature.

MODIS : Moderate Resolution Imaging Spectroradiometer.

NW : North-Western.

NWA : North-West African.

RELU: Rectified Linear Unit.

ResNets : Residual Networks.

RMSprop : Root Mean Square Propagation.

SDL : Soft Dice Loss.

SST: Sea Surface Temperature.

LIST OF FIGURES

LIST OF TABLES

LIST OF PUBLICATIONS

- **Belmajdoub, Hanae** and El Aouni, Anass and Minaoui, Khalid: Convolutional neural networks for coastal upwelling monitoring along the Atlantic Coast of Morocco. Journal of Remote Sensing Letters, Taylor & Francis,2023,14(8),pp 775-785.
- **Belmajdoub, Hanae** and Minaoui, Khalid and El Aouni, Anass and Hilmi, Karim and Saadane, Rachid and Chehri, Abdellah: A New Upwelling Index for the Moroccan Atlantic Coast for the Period between 1982-2021. Journal of Remote Sensing, MDPI, 2023, 15(14),pp.3459.
- **Belmajdoub, Hanae** and Minaoui, Khalid and El Aouni, Anass EL Abidi Zineb: Monitoring Upwelling Regions in Major Coastal Zones Using Deep Learning and Sea Surface Temperature Images. Submitted to International Journal of Remote Sensing, Taylor & Francis.
- **Belmajdoub, Hanae** and Minaoui, Khalid : Revolutionizing Upwelling Monitoring in Major Coastal Areas from Physical and Biological Satellite Observations using Transformer Models. Undergoing Preparation.
- **Belmajdoub, Hanae** and Mafamane, Rachid and Bekali Karfa, Younes, and Ouadou, Mourad and Minaoui, Khalid: Face Recognition based on CNN,

Hog and Haar Cascade Methods using Raspberry Pi v4 Model B. Smart Embedded Systems and Applications, CRC Press, pp. 195.

- **Belmajdoub, Hanae** and Elabidi, Zineb and Minaoui, Khalid: Automatic detection of Moroccan coastal upwelling from chlorophyll-a concentration images using the Expectation-Maximization method. International Symposium on Signal, Image, Video and Communications (ISIVC). 2022, pp.1-5.
- **Belmajdoub, Hanae** and Minaoui, Khalid: DeepRes-UpwellNet: A Robust Framework for Coastal Upwelling Monitoring Along the Moroccan Atlantic Coast. IEEE International Conference on Advances in Data-driven Analytics and Intelligent Systems.
- **Belmajdoub, Hanae** and Minaoui, Khalid: Delineation of Upwelling along the Northwest African coast using Attention-Coastal-Up-Net. Under preparation for International Symposium on Signal, Image, Video and Communications (ISIVC) 2024.
- Elabidi, Zineb and **Belmajdoub, Hanae** and Minaoui, Khalid: Fusion and Deep Learning Methods for Upwelling Coast Extraction from Biological and Physical Satellite Images. International Conference on Advanced Technologies for Humanity (ICATH'2023).
- Zaguir, Siham and **Belmajdoub, Hanae** and Minaoui, Khalid: Predicting Sea Surface Temperature along Morocco's Atlantic Coast Using LSTM and Satellite-Derived Data. Euro-Mediterranean Conference for Environmental Integration (EMCEI-5).
- Licer, Marwa and Minaoui, Khalid and **Belmajdoub, Hanae**: Evaluation of Machine-Learning Models for Predicting the daily Maximum Air Tempera-

ture: A Case Study Laâyoune in Morocco. Euro-Mediterranean Conference for Environmental Integration (EMCEI-5).

- Licer, Marwa and Minaoui, Khalid and Saadane, Rachid and **Belmajdoub, Hanae**: Advanced PAPR Reduction Techniques for MultiBand OFDM in WBANs. IEEE International Conference on Advances in Data-driven Analytics and Intelligent Systems.

CONTENTS

GENERAL INTRODUCTION

The research delineated in this thesis aims to employ advanced image and signal processing, coupled with computer vision techniques, to investigate and define areas linked to the upwelling phenomenon, particularly within the Northwest Africa (NWA) region. This analysis relies on imagery that records sea surface temperature (SST) and chlorophyll-a concentration (CHL-a). The primary objective is to harness the potential of artificial intelligence-driven image processing algorithms to detect and extract upwelling patterns and monitor their spatial and temporal evolution.

Understanding oceanographic phenomena necessitates a profound grasp of ocean dynamics and circulation, underpinned by the examination of multifarious mechanisms operational within the oceans. A pivotal task for oceanographers is the exploration of coastal upwelling systems, characterized by the ascension of deep waters from the continental shelf, compensating for the offshore drift of surface waters. This is facilitated by the synergistic effect of favorable winds, Earth's rotation, and notably, the Coriolis force.

This upward movement of cold waters is typically accompanied by nutrient enrichment, stimulating photosynthesis in the euphotic zone. These systems forge potent oceanic structures, impacting the distribution of the euphotic layer and inducing variations in fisheries resources. It's pertinent to note that around 25% of global fish catches are sourced from major upwelling ecosystem currents, covering over 5% of the total oceanic surface area.

The detection and analytical exploration of upwelling is economically pivotal, serving as the primary enrichment source for coastal ecosystems. Given the limitations and discontinuity of in-situ measurements, satellite imagery emerges as a vital resource, illuminating the characteristic mesoscale structures of upwelling zones.

While conventional methods for extracting and identifying upwelling zones exist, they often grapple with challenges due to spatiotemporal variability. In this milieu, advancements in AI, encompassing convolutional neural networks (CNNs) and machine learning, offer novel avenues for precise and efficient delineation, monitoring, and management of upwelling.

Acknowledging the significance of identifying these productive zones, this thesis posits two primary objectives. The first is the autonomous and efficient discernment of icy, nutrient-rich waters associated with coastal upwelling using AI techniques applied to biological and physical satellite imagery. Concurrently, the second objective is to propose enhanced upwelling indices and explore the intricate spatiotemporal dynamics characterizing these regions.

To realize the project's objectives, several key considerations were pivotal, in shaping the research trajectory. The discourse revolves around these themes, enriching our comprehension of upwelling systems and their inherent dynamics. The initial focus is on examining the limitations inherent in current segmentation methods in accurately detecting Moroccan coastal upwelling. The lack of a universally applicable segmentation technique prompted an investigation, assessing how automated demarcation could aid in formulating new indices for analyzing spatiotemporal dynamics.

The thesis is structured into four main chapters, each contributing to peer-reviewed journals or international conferences. A synopsis of each chapter is provided below:

Chapter 1: Offers a detailed overview of coastal upwelling, elucidating its mechanisms and influenced geographical regions. It introduces fundamental concepts of remote sensing and the specific satellite imagery utilized in this research.

Chapter 2: Concentrates on computer vision techniques for identifying and segmenting upwelling patterns, reviewing classical methodologies and their limitations. It discusses the evolution of upwelling identification through the incorporation of deep learning methods.

Chapter 3: Proposes efficient AI-based methods for identifying upwelling from satellite images, demonstrating the robustness of convolutional neural networks in identifying upwelling from diverse data sources.

Chapter 4: Presents new indices derived from satellite observations, designed to provide insights into the dynamic characteristics of upwelling phenomena. It examines methodologies for extracting upwelling patterns, revealing their dynamic nature, and formulating new indices for assessing the spatio-temporal dynamics of upwelling.

CHAPTER

1 PHYSICAL PROCESSES OF COASTAL UPWELLING AND REMOTE SENSING.

1.1 Introduction

This chapter is devoted to elucidating the fundamental physics underlying coastal upwelling, the various mechanisms and indicators involved in the upwelling process, ecological responses to coastal upwelling events, identifying the main upwelling ecosystems, and introducing the various data used throughout this thesis.

1.2 Upwelling

The American Meteorological Society glossary [1] defines upwelling as ”an ascending motion of subsurface water by which water from deeper layers is brought into the surface layer and is removed from the area of upwelling by divergent horizontal flow”. While the National Oceanic and Atmospheric Administration [2] defines upwelling as ”a process in which cold, deep water rises to the surface”. Based on the processes involved, different forms of oceanic upwelling can be distinguished, depending on the mechanisms induced by the wind.

Coastal upwelling occurs when winds blowing for a sufficient period in a specific direction drive warm water away from the coast, allowing cold water to rise

---

[1] `http://amsglossary.allenpress.com/glossary/`

[2] `https://oceanservice.noaa.gov/facts/upwelling.html`

to the ocean surface. This is the most well-known type of upwelling, and the one most closely linked to human activities [Feely et al. [2008]], [Huyer [1983]], [Bakun [1990]].

Equatorial upwelling occurs around the equator, where trade winds from the southern hemisphere reach the northern hemisphere, resulting in a consistent wind direction on both sides of the equator. This generates a divergence at the equator's surface, which transports nutrient-rich water upward from below [Wyrtki [1981]], [Picaut [1983]].

Southern Ocean upwelling is classified as a type of coastal upwelling and results from the presence of strong easterly winds that surround Antarctica throughout the year. A unique feature of this region is the absence of continents in a band of open latitudes between South America and the tip of the Antarctic Peninsula. This geographical feature facilitates the upwelling process by providing a pathway for deep water masses from the global ocean to rise to the surface [Anderson et al. [2009]].

1.2.1 Coastal upwelling

Coastal upwelling is the best-known type of upwelling, and the most closely related to human activities because it provides important productive fisheries around the globe. This oceanographic phenomenon is characterized as a wind-driven, near-shore circulation induced within a stratified rotating ocean [O'Brien and Hurlburt [1972]]. Several key elements can be discerned from this definition:

Wind: The dynamics of coastal upwelling are predominantly influenced by the force of winds.

Near-shore: This phenomenon primarily occurs in coastal zones.

Stratification: The fluid exhibits vertical water masses with distinct properties such as density, temperature, and salinity.

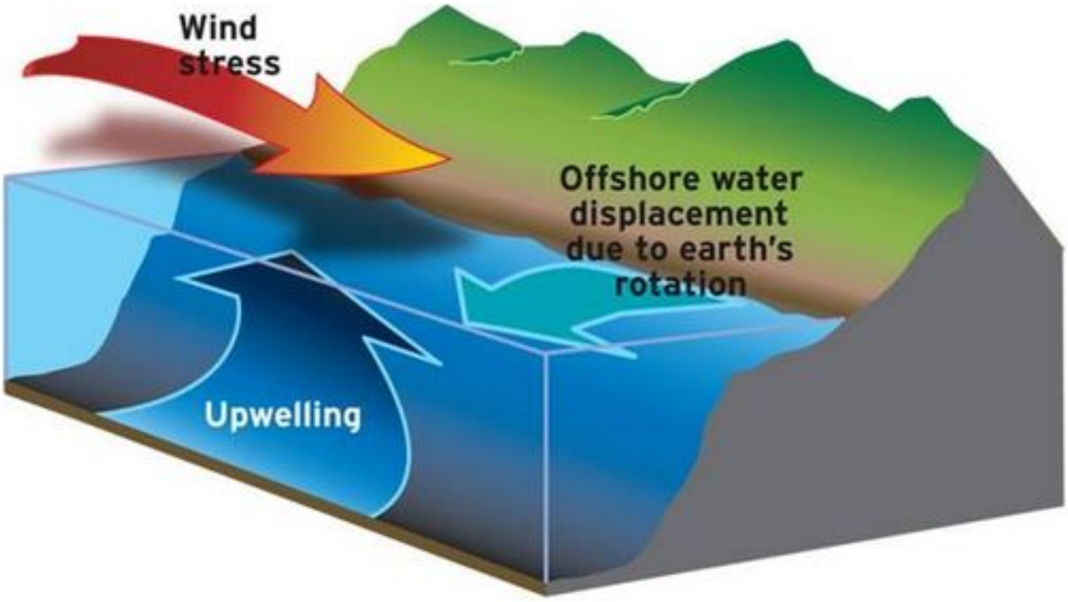

Figure 1.1: Northern Hemisphere Coastal Upwelling Scheme: Illustrating Southward Winds Inducing a 90° rightward Net Movement of Surface Water, resulting in Upwelling [3]

Rotation: The Coriolis effect, resulting from the Earth's rotation, plays a significant role in shaping the dynamics of the upwelling phenomenon.

1.2.2 The Mechanisms of Coastal Upwelling

The underlying mechanism of coastal upwelling involves winds blowing persistently over the sea surface for a prolonged period in a specific direction, as described by [Stewart [2008]] (a concise representation of coastal upwelling is shown in Figure 1.1). The result is wind-water interaction and mean transverse water transport [Ekman [1905]]. This phenomenon is called *Ekman transport* and results in a net movement of the Ekman layer at an angle of 90° to the right (left) of the wind in the northern (southern) hemispheres, respectively.

---

[3] `https://www.fisheries.noaa.gov/`

To better understand how winds induce upwelling, let's look at the Northern Hemisphere scenario. When winds blow from north to south parallel to the coast for long periods (known as wind stress), the Coriolis effect due to the Earth's rotation causes Ekman transport offshore at the ocean surface. This results in a net movement of the Ekman layer of around 90° to the right of the wind direction. To maintain mass continuity, deeper water rises to replace displaced surface water. As a result, the upwelled water is nutrient-enriched, saltier and colder than the water typically found at the ocean surface [Zhang et al. [2012]].

1.2.3 Ecological impact of upwelling

Due to the upwelling process, deep and cold water ascends to the ocean's surface, carrying with it essential nutrients such as nitrate, phosphate, and silicate, as well as dissolved gases like oxygen and carbon dioxide. These nutrients and residual gases are not used deep down due to the limited penetration of sunlight. Upon reaching the surface, they play an important role in stimulating the process of photosynthesis carried out by minute algae known as phytoplankton. The upwelling event triggers a bloom of phytoplankton, which can manifest in diverse shapes and forms. These phytoplankton collectively serve as the foundation of the marine food webs. Figure 1.2 illustrates the ecological impact of upwelling, which is characterized by the upwelling of tiny ocean organisms, essential minerals and various nutrients, including phytoplankton.

In the climatic context, the upwelling phenomenon exerts a cooling influence on the coastal air. Consequently, this temperature change fosters the formation of sea fog or low stratus clouds in the proximity of coastal regions, a characteristic occurrence in upwelling areas during the summer season. The presence of warmer air above the boundary layer hinders vertical convection, resulting in increased

---

[4] `https://oceanservice.noaa.gov/facts/upwelling.html`

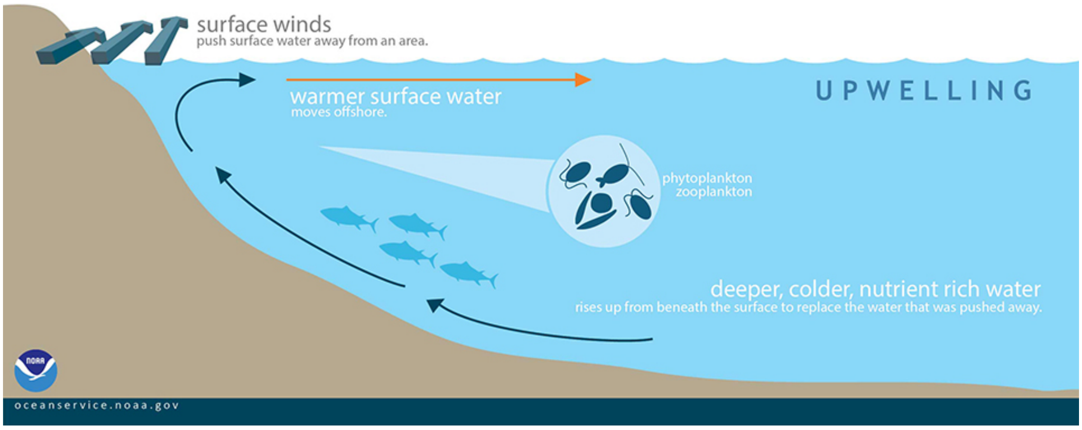

Figure 1.2: Ecological impact of upwelling: The phenomenon of upwelling facilitates the ascent of tiny ocean organisms, minerals, and various nutrients (such as phytoplankton) from the deeper layers of the water layer. Phytoplankton is an essential component of the marine food chain and plays a central role in the development of the seafood network [4].

atmospheric stability and reduced precipitation. This climatic pattern offers an explanation for the arid conditions observed in lands neighboring coastal upwelling zones, as seen in regions such as the Atacama desert (Chile), the Namib desert (southwest Africa), Baja California desert (U.S.A), and the Atlantic coastal desert of Morocco [Troupin [2011]].

1.2.4 Upwelling features

- **Thermal Front**: The thermal front denotes the boundary region that demarcates the transition zone between the cold waters of upwelling and the warmer masses of offshore waters. To qualify as an upwelling front, a temperature variation of $1°C$ or more must occur within a spatial extent of 10km [Tamim et al. [2015]]. Each thermal front is distinguished by three primary components [Nieto et al. [2012]]: its identity, including specific characteristics that differentiate it from other fronts; its state, encompassing its length, position, direction, and intensity; and its behavior, which encompasses its speed of movement and deformation characteristics.

- **Filaments**: Mesoscale cross-shore structures positioned along the upwelling front are referred to as filaments. These elongated, shallow tongues of cold upwelled water originate from the coastline. Due to their significant biological and chemical roles and their impact on primary production [Troupin et al. [2012]], numerous surveys have been conducted to study the filament processes [Haynes et al. [1993]], [Barton and Arístegui [2004]], [Pelegrí et al. [2005]].

1.2.5 Detecting Upwelling Events

As stated by the National Oceanic and Atmospheric Administration, upwelling is a process whereby deep, cold water ascends towards the ocean's surface. This characteristic cooling of upwelled water allows for the easy identification of upwelling events through SST images. Figure 1.3 illustrates a compilation of SST measurements acquired by the Moderate Resolution Imaging Spectroradiometer (MODIS) sensor aboard the Terra satellite, spanning from January 1, to December 31, 2007. These data were accessed from the Ocean Color web page (`https://oceancolor.gsfc.nasa.gov`).

In the depths of the ocean, upwelling currents carry valuable nutrients and dissolved gases, which remain untapped due to limited sunlight [Bakun [1990]]. However, when these upwelled waters reach the surface, they become essential for fueling the process of photosynthesis in tiny algae called phytoplankton [Margalef [1978]]. The phytoplankton possess a greenish pigment called chlorophyll, which gives them their distinctive color [Pottier [2006]]. As phytoplankton populations thrive and multiply, they cause the ocean to take on a green hue. Detecting these regions of upwelling becomes possible through ocean color images, such as the CHL-a concentration map in Figure 1.4. This map, compiled using MODIS

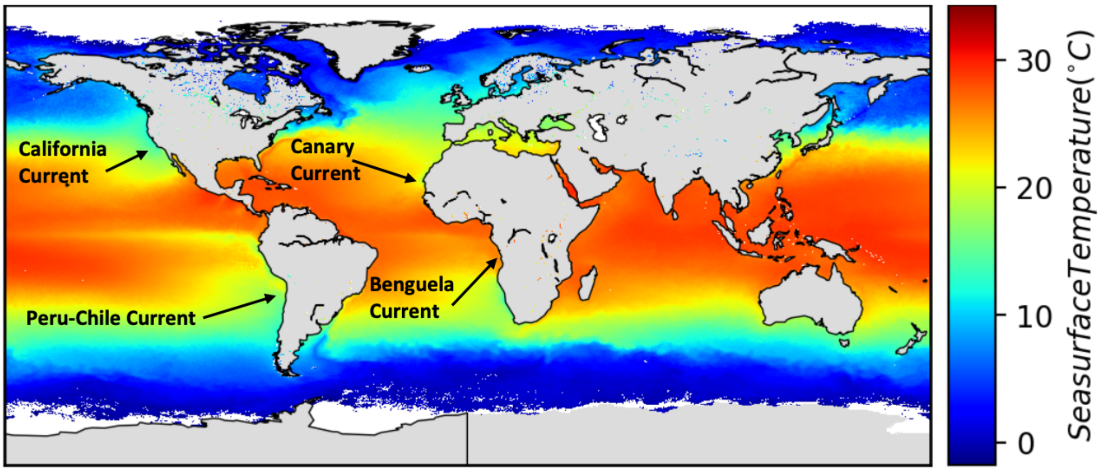

Figure 1.3: Climatology of Sea Surface Temperature from January 1st to December 31st, 2007 highlighting the four main upwelling ecosystems in the world.

images captured throughout the year 2007, reveal coastal areas with high CHL-a concentration, indicative of upwelling regions.

By analyzing global surface temperature and CHL-a distribution, four prominent upwelling systems can be identified:

The **Canary Current**, situated off the northwest coast of Africa.

The **Benguela upwelling**, occurs along the coasts of Namibia and South Africa.

The **Peru-Chile upwelling system**, is also known as the Humboldt Current.

The **California upwelling system** found along the western coast of North America.

These upwelling systems are strategically located in the eastern part of the primary subtropical gyres, earning them the designation of **Eastern Boundary Upwelling Systems** (EBUS). By understanding the significance of upwelling regions, we can gain valuable insights into marine ecosystems and their productivity.

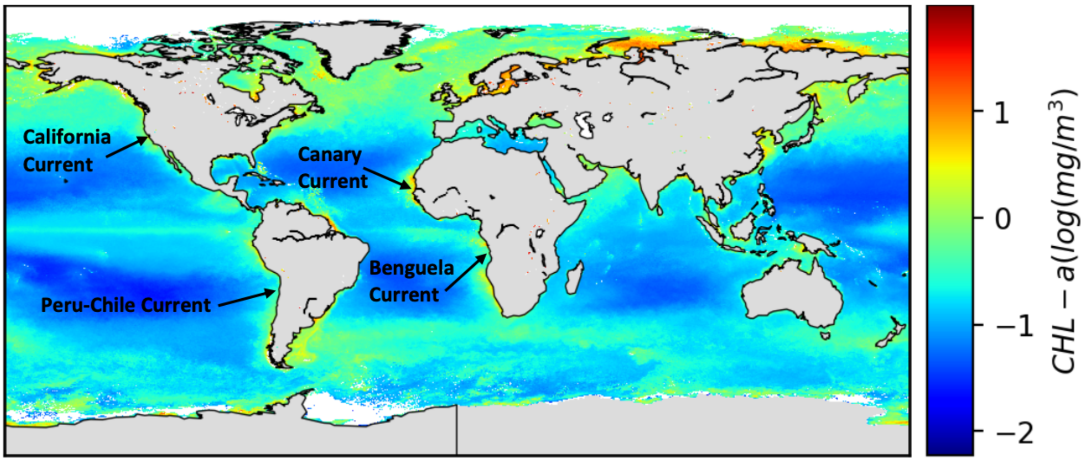

Figure 1.4: Climatology of chlorophyll-a concentration from January 1st to December 31st, 2007 highlighting the four main upwelling ecosystems in the world.

1.3 Remote Sensing and Satellite Images

Remote sensing enables the systematic observation and study of diverse phenomena through the utilization of specialized instruments. Specifically, satellites serve as an important tool in monitoring and analyzing the Earth's oceans by acquiring vital data related to temperature, surface salinity, sea level, water color, and surface winds. This approach offers unparalleled spatial and temporal coverage, surpassing conventional methods reliant on boats or other in-situ techniques.

1.3.1 Remote Sensing

Remote sensing is a scientific discipline that facilitates the non-invasive observation of Earth, ocean, and atmospheric systems from a distance, devoid of any physical contact [Lillisand et al. [2000]]. This technique operates on the principle of exploiting electromagnetic radiation emitted from a source, which subsequently interacts with targets on the Earth's surface, exhibiting distinct responses based on their physical, chemical, and biological properties. These responses may include reflection, emission, or backscattering towards a sensor [Boyd [2005]]. Remote sensing can be classified into two primary categories: ”active” remote sensing, wherein a signal is emitted by a satellite or aircraft, and its reflection from the object is detected by the sensor, and ”passive” remote sensing, wherein the sensor detects the reflected sunlight [Schowengerdt [2006]]. This powerful approach equips researchers with invaluable data, enabling comprehensive investigations of various environmental elements and processes across extensive spatial and temporal scales.

1.3.1.1 Type of Resolution

In remote sensing and satellite imagery, four fundamental types of resolution are recognized: spatial resolution, spectral resolution, temporal resolution, and radiometric resolution.

Spatial Resolution: Satellite imagery is composed of a collection of pixels, where each pixel corresponds to measurements taken from a specific small area on the Earth’s surface, essentially treated as an individual unit [Unger Holtz [2007]]. An important characteristic of satellite images is spatial resolution, which determines the smallest dimension of the Earth’s surface over which the sensor can independently acquire measurements. This resolution is affected not only by the sensor’s technical specifications but also by its altitude above the Earth. Figure 1.5 provides a visual example of different spatial resolutions. Higher spatial resolution corresponds to smaller pixel sizes, allowing for finer details and greater precision in representing Earth’s features. Understanding spatial resolution is fundamental in satellite image analysis, as it directly impacts the level of detail and information obtained from the imagery, affecting a wide array of applications in remote sensing and geospatial studies.

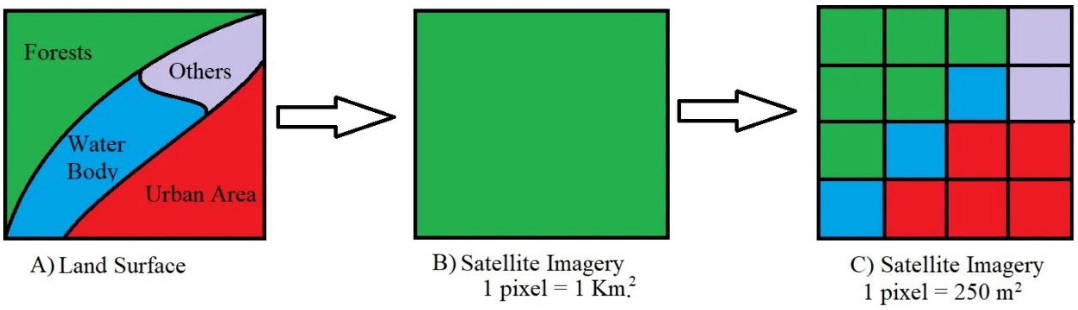

Figure 1.5: Example of low and high spatial resolutions [5].

Spectral Resolution: Our vast universe is permeated with electromagnetic radiation spanning a wide range of wavelengths, from the minute gamma rays with wavelengths to the much longer radio waves with wavelengths (see Figure 1.6). Within an image, distinct classes of features and details can often be discerned by analyzing their responses across different wavelength ranges [Unger Holtz [2007]]. This attribute, known as spectral resolution or frequency spectrum, encompasses both the number and width of bands present in a given sensor [Congalton [2010]]. The higher spectral resolution entails a larger number of bands and narrower spectral widths, enabling finer discrimination between various features and rock types. For example, to differentiate between specific rock types, a comparison at much finer wavelength ranges is required. As a result, a sensor equipped with higher spectral resolution enhances the capacity to resolve intricate details and classify diverse elements present in the observed imagery.

Radiometric resolution: The radiometric resolution of an image complements the spatial resolution by determining its actual information content [Shi et al. [2012]]. This resolution is contingent on the imaging system's sensitivity to the magnitude of electromagnetic energy during image acquisition, enabling it to dis-

---

[5] https://pangeography.com/types-of-resolution-in-remote-sensing/
[6] https://skywatch.com/

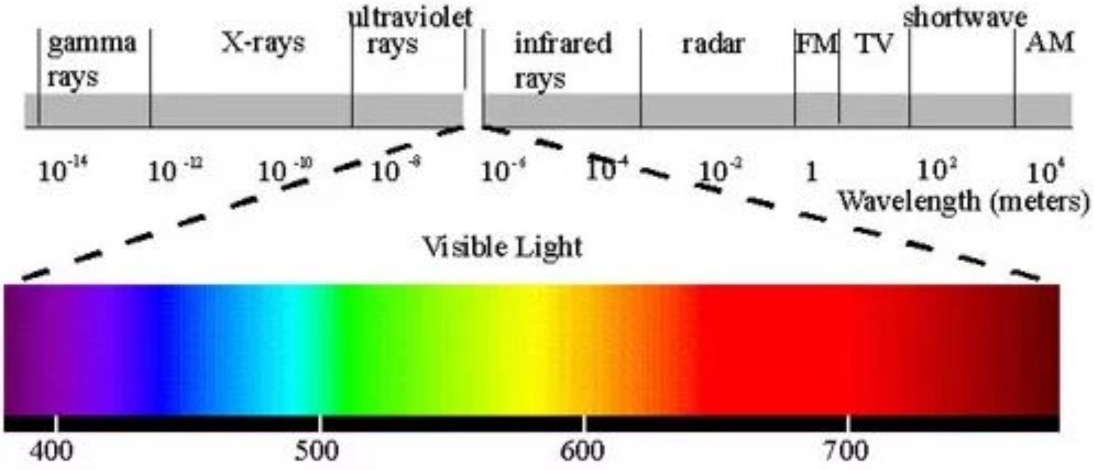

Figure 1.6: Different spectral bands and their wavelengths. [6]

criminate even the subtlest differences in energy. A sensor with finer radiometric resolution [Lillesand et al. [2015]] exhibits heightened sensitivity to detect small variations in reflected or emitted energy, thereby capturing a broader dynamic range of the acquired signal. Essentially, radiometric resolution corresponds to the number of bits used to record the image, facilitating the sensor's capacity to discern minute fluctuations in electromagnetic energy. Electromagnetic energy travels in waves spanning a wide spectrum, ranging from long waves (radio) with lower energy to short waves (gamma rays) with higher energy [Parkinson and Wollack [2010]]. Emphasizing the dynamics of the acquired signal, radiometric resolution proves essential in extracting rich information from the image and enabling comprehensive analysis and interpretation of various features and phenomena.

Temporal Resolution: In remote sensing, considering temporal resolution alongside spatial, spectral, and radiometric resolutions becomes crucial. Temporal resolution relates to the precision of time-based measurements and signifies the minimum time interval within which a specific feature can be captured twice.

The absolute temporal resolution of a remote sensing system is determined by the repeat cycle of a satellite, indicating how quickly it can image the same area at the same viewing angle for a second time. The capability to acquire imagery of the same Earth's surface area at different time intervals holds paramount importance in leveraging remote sensing data [Lillesand et al. [2015]. This allows for the detection of spectral changes in features over time, enabling the collection and comparison of multi-temporal imagery. Temporal resolution, representing the revisit time of the sensor, is especially valuable for monitoring surface changes on Earth, both natural (e.g. Earth's color variations, sea conditions, forest monitoring) and human-induced (e.g. urban development, deforestation). The effectiveness of good temporal resolution is further enhanced by a satellite's agility to view different angles and directions. Although it is rare to find a sensor that excels in all types of resolution with high quality, some sensors strike a balance between them, aligning with their specific objectives.

1.3.2 Satellite Images

In this study, we utilize data acquired from the Moderate Resolution Imaging Spectroradiometer (MODIS), which is provided by the National Aeronautic and Space Administration (NASA). MODIS is a scientific instrument installed on two satellites: Terra (launched in 2000) and Aqua (launched in 2002). Aqua's orbit is designed to cross the equator from south to north in the afternoon (EOS PM), whereas Terra's orbit traverses the equator from north to south in the morning. As a result, Terra MODIS and Aqua MODIS together provide global coverage every 1 to 2 days, offering 36 spectral bands ranging from 0.4 µm to 14.4 µm, encompassing the visible to infrared regions (refer to Table 1.1 for detailed information). These satellites provide daily, weekly, monthly, and annual images at two distinct spatial resolution levels: 4.64 km and 9.26 km, respectively [Huete et al. [2002]].

The MODIS instrument proves highly suitable for monitoring and measuring various parameters of the Earth's surface, contributing to an enhanced understanding of global dynamics and processes occurring in terrestrial, oceanic, and lower atmospheric environments [Walker et al. [2012]]. Through the use of MODIS data, we gain valuable insights into a wide range of earth-related phenomena, allowing us to improve our knowledge of global environmental changes and their underlying mechanisms. The combination of Aqua MODIS and Terra MODIS, with their extensive spectral coverage and frequent global revisits, empowers conduct comprehensive studies and addresses scientific questions related to the dynamics and behavior of our planet.

1.3.2.1 Sea Surface Temperature

The measurement of SST offers a comprehensive perspective on the temperature distribution of the ocean's skin layer, encompassing the first few micrometers of the surface [Rayner et al. [2003]. Utilizing satellite-based SST data, such as NASA's (National Aeronautic and Space Administration) MODIS, enables to obtain synoptic views of the ocean's dynamics and frequent revisits to the same areas, which surpasses the limitations of ships and buoys [Mitra and Zaman [2020]]. MODIS satellites have been continuously providing global SST data since 2000, presenting daily, weekly (8-day), and monthly images with spatial resolutions of 4.63 and 9.26 km for both day and night observations [Minnett [2003]]. As an example, The figure 1.7 showcases an 8-day SST image from MODIS, capturing the North-West African upwelling.

Primary Use	Band	Bandwidth	Spectral Radiance	Required SNR
Land/Cloud/Aerosols Bondaries	1	620-670	21.8	128
	2	841-876	24.7	201
Land/Cloud/Aerosols Properties	3	459-479	35.3	243
	4	545-565	29.0	228
	5	1230-1250	5.4	74
	6	1628-1652	7.3	275
	7	2105-2155	1.0	110
Ocean Color/ Phytoplankton/ Biogeochemistry	8	405-420	44.9	880
	9	438-448	41.9	838
	10	483-493	32.1	802
	11	526-536	27.9	754
	12	546-556	21.0	750
	13	662-672	9.5	910
	14	673-683	8.7	1087
	15	743-753	10.2	586
	16	862-877	6.2	516
Atmospheric Water Vaper	17	890-920	10.0	167
	18	931-941	3.6	57
	19	915-965	15.0	250
Surface/Cloud Temperature	20	3.660-3.840	0.45	0.05(300K)
	21	3.929-3.989	2.38(335K)	2.00
	22	3.929-3.989	0.67(300K)	0.07
	23	4.020-4.080	0.79(300K)	0.07
Atmospheric Temperature	24	4.433-4.498	0.17(250K)	0.25
	25	4.482-4.549	0.59(275K)	0.25
Cirrus Clouds Water Vapor	26	1.360-1.390	6.00	150
	27	6.535-6.895	1.16(240K)	0.25
	28	7.175-7.475	2.18(250K)	0.25
Cloud Propreties Ozone	29	8.400-8.700	9.58(300K)	0.05
	30	9.580-9.880	3.69(250K)	0.25
Surface/Cloud Temperature	31	10.780-11.280	9.55(300K)	0.05
	32	11.770-12.270	8.94(300K)	0.05
Cloud Top Altitude	33	13.185-13.485	4.52(260K)	0.25
	34	13.485-13-785	3.76(250K)	0.25
	35	13.785-14.085	3.11(250K)	0.25
	36	14.085-14.385	2.08(220K)	0.35

Table 1.1: Characteristics of 36 Spectral Bands in MODIS: bands from 1 to 19 are in µm, bands 20 to 36 are in nm, Spectral Radiance values are (W/m^2-µm-sr), and SNR = Signal-to-noise ratio, NE(Δ)T = Noise equivalent temperature difference.

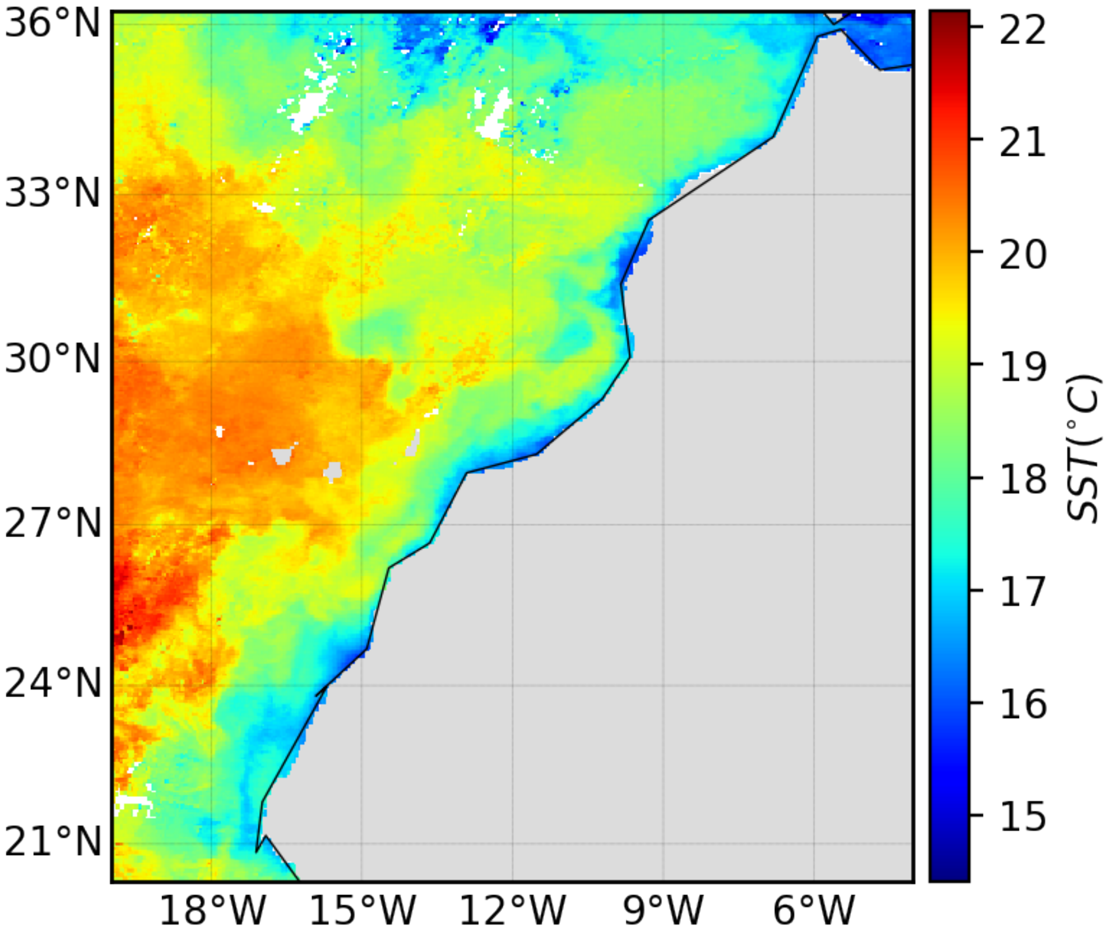

Figure 1.7: Modis 8-day SST image obtained during the first week of January 2019 reveals a typical upwelling scenario over the North-West African margin. Each pixel in the image represents a specific temperature value in degrees Celsius.

This thesis focuses on the utilization of NASA's MODIS for SST analysis. Since 2000, MODIS satellites have been instrumental in providing comprehensive global SST data. Additionally, for earlier data, the study incorporates information from The European Space Agency (ESA) Climate Change Initiative Sea Surface Temperature Project (ESA SST_cci). This ESA project has successfully and accurately determined surface temperatures of the world's oceans from 1981 to the present, using data derived from various satellites. The dataset offers independently quantified SSTs of high quality, specifically suited for climate research purposes. Furthermore, as part of the ESA SST_cci project, the GHRSST (Group for High-Resolution Sea Surface Temperature) Multi-Product Ensemble (GMPE) dataset has been created. Its primary objective is to enable seamless comparisons between the ESA's spatially complete analyses and other level 4 SST analysis products.

1.3.2.2 Ocean Color

Ocean color data differs significantly from SST data, as it results from the interaction between visible solar radiation and suspended particles in the ocean [Pottier et al. [2008]]. These interactions lead to distinct spectral characteristics for phytoplankton and dissolved organic matter. Consequently, ocean color data can be calibrated to provide datasets of CHL-a measured in units of mg/m^3 [Carder et al. [2004]]. CHL-a concentration data serves as a valuable indicator of the live phytoplankton biomass in the ocean's surface layer [Pottier et al. [2008]].

To obtain this valuable information, the MODIS terra instrument utilizes a 3-band ocean color algorithm (OC3) in conjunction with the NOAA-MSL12 software [Hlaing et al. [2013]]. Moreover, atmospheric correction is achieved using the NOAA NIR-SWIR combined approach, developed by the NOAA/NESDIS Center for Satellite Applications and Research (STAR). As a result, the MODIS CHL-a products offer quantitative data on global ocean bio-optical properties, facilitating the examination of various oceanic factors influencing global change, and enabling the assessment of the oceans' roles in the global carbon cycle and other biogeochemical cycles.

The Level 3 standard mapped image (SMI) CHL-a dataset derived from MODIS terra observations provides data daily, weekly (8-day), and monthly temporal resolutions, with a spatial resolution of 4.6 km at the equator. Figure 1.8 exemplifies a

MODIS 8-day image capturing the North-West African upwelling, demonstrating the dataset's utility in monitoring oceanic phenomena and environmental changes on a regional scale. This dataset offers invaluable insights into the dynamics of marine ecosystems and their responses to various environmental influences.

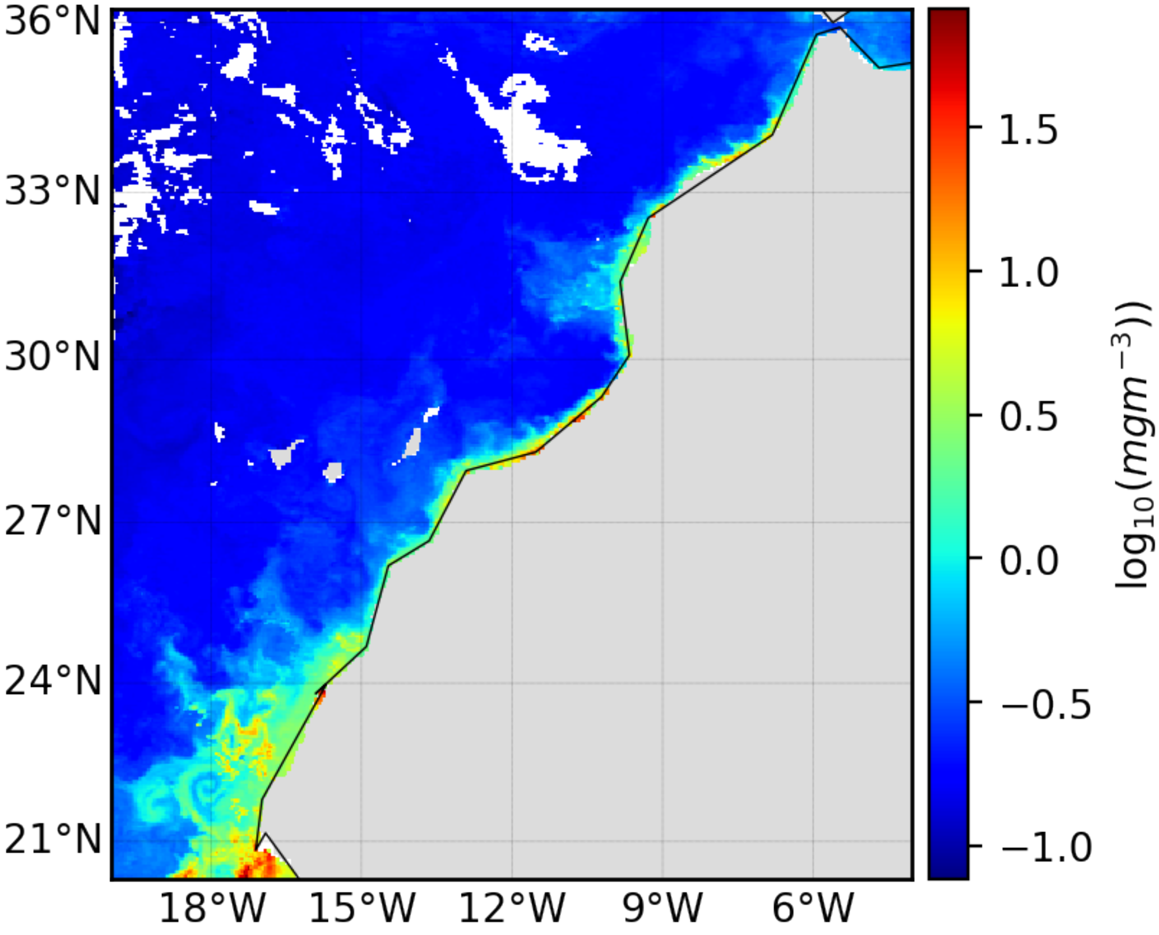

Figure 1.8: Modis 8-day of CHL-a image obtained during the first week of January 2019 reveals a typical upwelling scenario over the North-West African margin. Each pixel in the image represents the chlorophyll concentration value in $\log(mg/m^3)$.

1.3.2.3 wind speed

Ocean winds are routinely monitored in the vicinity of the ocean surface using various methods such as buoys, platforms, and ships. Typically, the standard reference height for these near-surface ocean wind measurements is 10 meters above sea level. Both in situ (on-site) and remote sensing (from afar) techniques are employed to collect these measurements, with a particular emphasis on satellite-based observations [Wentz [1992].

Satellite-based measurements of ocean surface winds rely on two main types of microwave instruments: passive microwave radiometers and active microwave scatterometers. The movement of air above the ocean surface triggers a rapid response, creating a distinctive roughness pattern that varies based on the relative speed and direction of the wind in relation to the ocean surface [Risien and Chelton [2008]. This roughness generates specific ”brightness” characteristics, which, when combined with appropriate microwave wavelengths and processing algorithms, allow for the accurate calculation of near-surface wind speeds [Liu [2002]].

This thesis will leverage data from the Cross-Calibrated Multi-Platform (CCMP) Ocean Surface Wind Vector Analyses, which play a pivotal role in NASA’s Making Earth System Data Records for Use in Research Environments (MEaSUREs) Program.

The CCMP dataset encompasses a comprehensive and continuous time-series of ocean surface wind vector analyses, spanning from July 1987 to December 2020. This Level 3 dataset provides a high-resolution (0.25°) gridded analysis, derived through the combination of cross-calibrated satellite winds. These satellite wind measurements are collected by Remote Sensing Systems (RSS) using various microwave satellite instruments, including SSM/I, SSMIS, AMSR, TMI, WindSat, QuikScat, and SeaWinds. Notably, Figure 1.9 illustrates the observations of wind speed and direction over the North-West African upwelling, demonstrating the dataset’s utility in studying regional oceanic phenomena and processes.

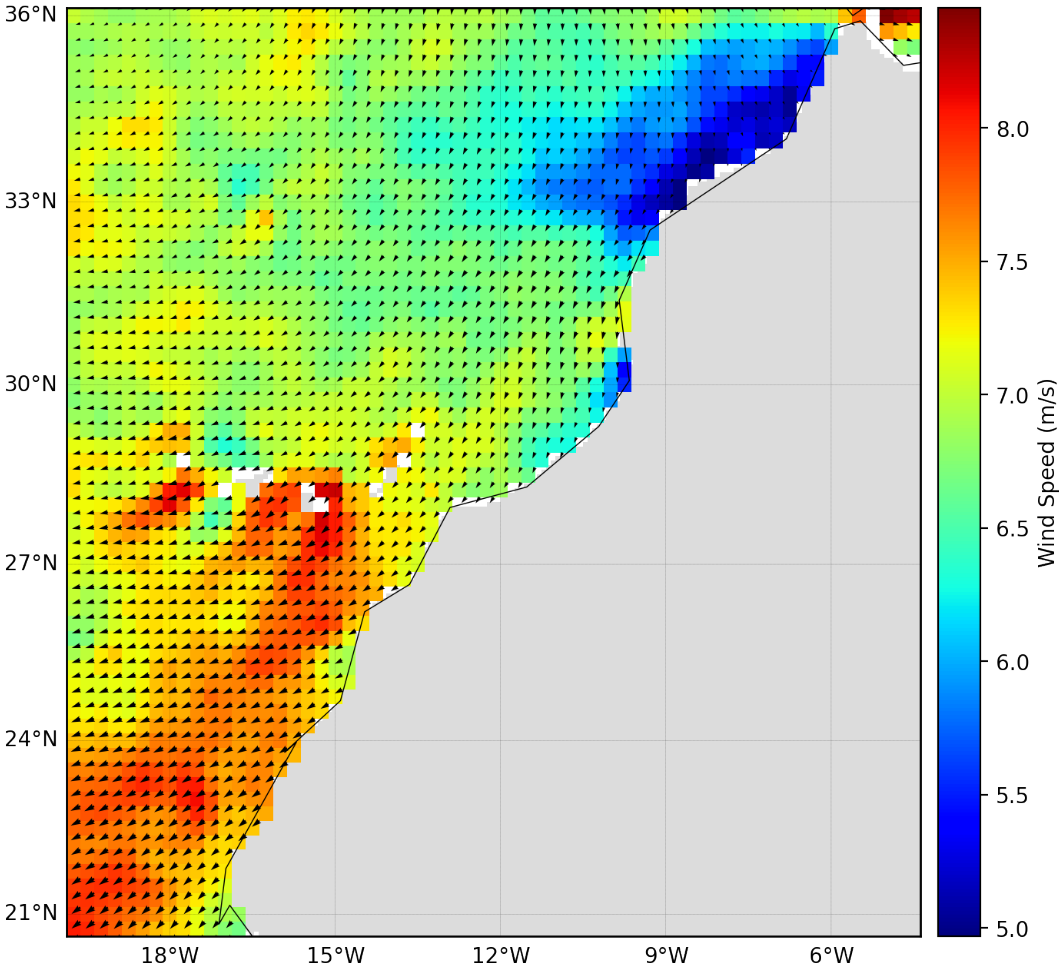

Figure 1.9: Ocean winds: QuikScat wind speed ($ms^{-}1$) during December 2019 reveals the dominant wind directions (black arrow) driving upwelling off the northwestern margin of Africa.

1.4 Importance of Investigating Upwelling Systems

The identification and delineation of upwelling regions are of considerable importance because of their profound impact on marine ecosystems, economies, and the global environment. These areas are essential centers of biological productivity, supporting marine biodiversity and sustaining fisheries that underpin the livelihoods and food security of coastal communities [Strass [1992]].

Although they cover only a small part of the ocean's surface, upwelling regions, such as the upwelling ecosystem of the Canary Islands off the northwest coast of Africa, play an essential role in the ocean's overall biological productivity. Their average productivity is estimated at around six times that of the open ocean [Ryther [1969]]. These regions are distinguished by their temperature and nutrient-rich characteristics compared to the surrounding open ocean. Cold water upwelling from deeper layers harbors significantly higher nutrient concentrations, sustaining a dynamic ecosystem with robust primary production when exposed to sunlight [Ryther [1969]].

The importance of upwelling systems goes beyond ecological factors since they also exert a considerable socio-economic influence. For example, the upwelling system of the Canary Islands supports a population of around 58 million people, almost 70% of whom depend on this system [Sherman and Hempel [2008]]. This vast coastal population extends over several countries, including Morocco, the Canary Islands (Spain), Mauritania, Guinea, Gambia, Cape Verde and Senegal. Fishing in this region contributes significantly to the GDP (Gross Domestic Product) of these nations, offering direct and indirect employment opportunities. In 2006, fishing in Morocco contributed 3% to the country's GDP and generated some 500,000 jobs [Kämpf and Chapman [2016]]. Similarly, Senegal's fishing industry contributed 11% to its GDP and supported around 700,000 jobs [Kämpf and Chapman [2016]]. However, the increasing exploitation of fishery resources has raised concerns about the sustainability of fish stocks and the overall ecological balance of these regions. Preserving biodiversity, the environment, and fisheries resources requires the regulation of fish populations based on a comprehensive understanding of the physical and biological dynamics of upwelling zones [Chassot et al. [2011]]. Continuous monitoring and research into the variability of coastal upwelling is therefore essential [Troupin [2011]].

Upwelling System	Surface $\times 10^6$	Productivity ($gCm^{-2}yr^{-1}$)
California	2.2	<150
Humbolt	2.5	150-300
Canary	1.1	>300
Benguela	1.5	>300

Table 1.2: Comparative Overview of Four EBUS Characteristics. Productivity mean is in grams of Carbon for each m^2 in each year ($gCm^{-2}yr^{-1}$)

The combined surface area of the four upwelling systems is remarkable. The largest among them is the Humboldt system, encompassing an impressive $2.5 \times 10^6 Km$ of the total ocean surface. Notably, all EBUS, except the California upwelling system, exhibit a productivity level of 300 $gCm^{-2}yr^{-1}$ or higher.

To better understand and effectively utilize the benefits of upwelling, many researchers are engaged in the task of precisely delineating these regions, prompting them to explore advanced methodologies. Notably, various computer vision approaches, including supervised and unsupervised methods, have been designed for segmentation and upwelling identification. These techniques have been adapted to extract and identify upwelling regions. The next chapter of this thesis will examine these techniques in detail, elucidating their complexities and contributions to understanding upwelling dynamics.

1.5 Conclusion

In this first chapter of our thesis, we explored the fundamental concepts of coastal upwelling and remote sensing, highlighting their ecological impact and importance. Coastal upwelling plays an essential role in influencing marine ecosystems by bringing nutrient-rich deep waters to the surface, increasing primary productivity and supporting marine life. We studied the mechanisms behind upwelling and focused on their ecological consequences. In addition, we discussed the distinctive features associated with upwelling and its importance as an indicator of larger-scale oceanic variations. Moving on to remote sensing and satellite imagery, we unveiled their potential for monitoring and understanding upwelling processes at larger spatial scales and over longer periods.

CHAPTER

2

COMPUTER VISION APPROACHES FOR UPWELLING SEGMENTATION AND IDENTIFICATION: FROM CLASSICAL METHODS TO DEEP LEARNING.

In the initial segment of this chapter, we turn our attention to the classical approaches commonly used in image processing. The focus is on the segmentation of upwelling regions from SST and CHL-a images. The main objective of this part is to carry out an in-depth review of previously proposed methods for the detection of upwelling phenomena, with particular emphasis on their application in the Northwest African region. Throughout this review, particular attention will be paid to describing the advantages and limitations associated with each of these methods.

Despite the invaluable knowledge offered by conventional methods, they often run into difficulties when it comes to identifying upwelling. In response to these challenges, we will explore the realm of deep learning (DL) and artificial intelligence (AI) in the second part of this chapter. This transition aims to exploit the capabilities of deep neural networks and state-of-the-art machine learning algorithms to improve the accuracy, efficiency, and robustness of upwelling detection.

2.1 Classical Image Segmentation Methods

Image segmentation has remained a fundamental challenge in the field of computer vision since its inception. It is an essential element of various visual understanding systems, involving the division of images (or video frames) into several segments and objects. Its importance is underlined by its central role in a wide spectrum of applications, covering fields such as medical image analysis (e.g. tumor boundary extraction and tissue volume measurement), autonomous vehicles (e.g. identification of navigable surfaces and pedestrian detection), Segmentation of satellite images (e.g., delineation of upwelling boundaries, as well as analysis of satellite images for applications such as land-use classification and coastal erosion monitoring). video surveillance...

The problem of image segmentation can take several different forms, each responding to specific objectives. Semantic segmentation, for example, involves assigning semantic labels to individual pixels effectively labeling them with categories of objects (e.g. humans, car, trees, and the sky) in the image as a whole. As a result, this approach imposes a higher computational demand than whole-image classification, which predicts a single label for the entire image. Instance-based segmentation extends the scope of semantic segmentation not only by classifying pixels, but also by identifying and delimiting each object of interest in the image, for example, by delimiting people.

Over the years, numerous image segmentation techniques have been developed in this field. These methods can be classified into four broad categories: thresholding, edge detection-based techniques, region-based techniques, and clustering-based methods. Each of these approaches differs from the others, and the choice of method depends on the specific segmentation objectives and the characteristics of the input images.

2.1.1 Thresholding

In image processing and computer vision, thresholding is a widely used technique for image segmentation. The main idea behind thresholding is to divide an image into meaningful regions, typically by converting a grayscale image into a binary image, where pixels are classified as either belonging to the foreground (object of interest) or the background. This process involves setting a threshold value and comparing each pixel's intensity with this threshold to determine its final classification.

In the following section, we will describe some classical thresholding methods

Global Thresholding:

Global thresholding is the simplest form of thresholding. It involves selecting a single threshold value that is applied to all pixels in the image. Each pixel's intensity is compared to this global threshold, and if its value is greater, the pixel is assigned to the foreground; otherwise, it is assigned to the background. Global thresholding works well when the image has a well-defined bimodal histogram, where there are distinct peaks representing the foreground and background intensities.

Otsu's Method:

Otsu's method is an automatic thresholding technique that determines the optimal threshold value by maximizing the inter-class variance [Otsu [1979]]. It searches for the threshold that minimizes the intra-class variance (variance within foreground and background regions) while maximizing the inter-class variance (variance between foreground and background regions). This method is suitable for images with bi-modal or multi-modal intensity distributions.

Adaptive Thresholding:

Adaptive thresholding methods take into account local variations in the image's intensity by using different thresholds for different regions. This approach is useful when the illumination conditions are not uniform throughout the image. Adaptive methods calculate local thresholds based on a neighborhood around each pixel. Common adaptive thresholding techniques include Mean Adaptive Thresholding and Gaussian Adaptive Thresholding.

2.1.2 Edge detection-based techniques

Image segmentation can also be achieved by identifying edges, which are typically characterized by significant changes in intensity between two objects [[Pal and Pal, 1993]]. Essentially, all the outlines in an image emerge from variations in the intensity function due to factors like texture, shadow, or disparities in depth that mark the boundaries of objects. Various edge models, such as step, ramp, and roof profiles, are categorized based on their intensity characteristics [Gonzalez and Woods, 2002].

In essence, edge detection involves analyzing the derivatives of the image's intensity function. This entails examining the local extrema of the gradient (first derivative) and identifying the points where the intensity function crosses zero. It also considers the Laplacian (second derivative), all while being mindful of the potential presence of noise in the image that needs to be accounted for during the segmentation process.

Gradient edge detection:

The prevalent technique for edge detection involves the application of a gradient operator, with numerous adaptations documented in the literature[Maini and Aggarwal [2009]]. In mathematical terms, when dealing with an image function represented as $f(x, y)$, the computation of the gradient, denoted as $G(f(x, y))$, along with the gradient direction, $\theta(x, y)$, follows this formula:

$$G = (G_x, G_y) = (\frac{\partial f}{\partial x}, \frac{\partial f}{\partial y}) \tag{2.1}$$

$$\theta = arctan(\frac{G_x}{G_y}) \tag{2.2}$$

Where,

$$G_x = f(x+1, y) - f(x-1, y) \tag{2.3}$$

$$G_y = f(x, y+1) - f(x, y-1) \tag{2.4}$$

The gradient is characterized by two principal measures:

- The gradient's magnitude M, offers insights into the edge's intensity

$$M = \sqrt{G_x^2 + G_y^2} \tag{2.5}$$

- The gradient's direction (θ) is consistently orthogonal to the edge's orientation.

Canny edge detection:

The Canny edge detector, introduced in 1986 by John Canny [Canny [1986]], is a widely recognized gradient-based algorithm designed to meet three fundamental criteria:

- Accurate Detection: This criterion ensures that the algorithm minimizes errors when identifying contours, resulting in a low error rate.
- Precise Localization: Canny's edge detector strives to ensure that the detected contours closely match the actual contours in the image, minimizing the distance between them.
- Distinctive Response: It also aims for distinct and unique responses for edges, preventing false positive identifications.

2.1.3 Region-based techniques

Region-based algorithms work through iterative processes, with their primary objective being the segmentation of an image into distinct regions. These regions, denoted as R_i, are essentially collections of adjacent pixels that share a common attribute of homogeneity. This homogeneity can pertain to various properties, including color, gray level, texture, shape, or other defining characteristics. In essence, these algorithms aim to group pixels that exhibit similar properties while effectively separating clusters of pixels that differ significantly in their properties [Nikolaou and Papamarkos [2009]].

Region growing:

Region growing is a pixel aggregation process centered on combining neighboring pixels into a coherent region, guided by predefined criteria [Adams and Bischof [1994]]. This algorithm comprises two key components. Firstly, it involves selecting starting points, often referred to as seeds, which is a pivotal and intricate step. The second element revolves around assessing similarity, typically gauged by comparing a pixel's intensity value to the region's mean. Region growing holds great appeal, particularly in the context of semantic image segmentation [Fan et al. [2005]]. However, it's advisable to avoid initiating the algorithm with seeds located in regions of non-homogeneity, as this could lead to substantial dissimilarity measures and early termination of the growth process. The application of this method to SST, CHL-a images has proven valuable for detecting upwelling zones [Tamim et al. [2014c], Belmajdoub et al. [2022]]. Nevertheless, there are significant challenges associated with this method, as it require prior knowledge of criteria that can vary substantially from one image to another. This poses a significant constraint on segmentation due to factors like the initial seed point placement, choice of stopping conditions, computational demands, and sensitivity to noise.

Mathematical morphology:

Mathematical morphology (MM) stands as a distinct domain within the realm of image processing, enabling the examination and manipulation of geometric structures. Its inception can be attributed to the work of Matheron and Serra [Kingman [1975], Serra [1982]]. The term ”morphology” aptly describes its purpose, as it focuses on the analysis of object shapes and forms. Moreover, it is deeply rooted in mathematics, employing set theory and lattice algebra as fundamental tools for its analytical framework [Serra and Soille [2012]]. This method offers a broad spectrum of practical applications, notably in the realm of detecting thermal patterns within SST images [Holyer and Peckinpaugh [1989], Marcello et al. [2005]].

2.1.4 Clustering based methods

Clustering-based methods are a class of techniques used in data analysis and image processing to group data points or objects into clusters or subgroups based on their similarity or proximity to each other. These methods aim to identify inherent patterns or structures within the data without the need for predefined classes or labels. In the context of image processing, clustering-based methods can be applied to segment an image into regions or groups of pixels that share similar characteristics, such as color, intensity, texture, or other relevant features. This segmentation helps in identifying distinct regions or objects within the image. Among the frequently employed algorithms within clustering-based approaches are K-means and Fuzzy C-means.

K-means:

K-means stands as a straightforward unsupervised learning approach designed for tackling clustering problems. Its operation entails the partitioning of an image into a predetermined number of clusters, each characterized by a centroid. The algorithm’s initiation phase involves the random placement of centroids across the image. Subsequently, each pixel is assigned to the cluster represented by the nearest centroid. Following this assignment step, the centroids are re-calculated based on the new assignments, and this iterative process continues until the centroids reach a stable position. After this procedure, the image has been segmented into ”K” distinct clusters, where the pixels within each cluster exhibit similarity among themselves.

Fuzzy C-means:

Fuzzy C-means clustering is similar to K-means but allows for a more flexible assignment of data points to clusters. Instead of assigning data points to a single cluster, it assigns them membership degrees indicating their degree of belongingness to each cluster. This allows for soft boundaries between clusters, making it useful when data points may belong to multiple clusters simultaneously. Clustering-based methods are widely used in various applications, including image segmentation, data analysis, pattern recognition, and machine learning, to uncover underlying structures and relationships within data. The FCM algorithm is designed to partition a finite set of ”n” pixels, denoted as $(X = x_1, ..., x_n)$, into a collection of ”c” fuzzy clusters based on a specified criterion. After applying this algorithm to the pixel set, it provides two key outcomes: a list of ”c” cluster centers represented as $(C = c_1, ..., c_c)$, and a fuzzy partition matrix. This partition matrix quantifies the degree to which each pixel, such as x_k, belongs to a particular cluster, denoted as c_i.

The FCM algorithm’s primary objective is to minimize a mathematical function called the c-means functional:

$$J_m(X; U, V) = \sum_{k=1}^{n} \sum_{i=1}^{c} (u_{ik})^m ||x_k - v_i||^2 \tag{2.6}$$

Here, ”n” is the length of the vector X and signifies the number of pixels in an image. Additionally, ”$V = (v_1, v_2, ..., v_n)$” is the vector of cluster prototypes, and ”$U = [u_{ik}]$” is the fuzzy partition matrix that signifies the degree of membership for each pixel, x_k, to a specific cluster, c_i, and $||x_k - v_i||$ is the Euclidean norm. The parameter ”m” in the FCM algorithm controls the degree of fuzziness in membership values and can range within the interval $[1, \infty[$. When ”m” increases, it amplifies the level of fuzziness in the partitions.

The function described in (Eq.(2.6)) serves as a way to quantify the overall variance between each pixel x_k and the cluster prototypes v_i. The process of minimizing this objective function, as defined in (Eq.(2.6)), presents a nonlinear optimization challenge. This challenge can be addressed by utilizing the subsequent cluster centroids and membership functions:

$$v_i = \frac{\sum_{k=1}^{n}(u_{ik}^{m})x_k}{\sum_{k=1}^{n}(u_{ik}^{m})} 1 \leq i \leq c \tag{2.7}$$

$$u_{ik} = \frac{1}{\sum_{j=1}^{c}(\frac{||x_k - v_i||}{||x_k - v_j||})^{(\frac{2}{m-1})}}, 1 \leq i \leq c, 1 \leq k \leq n \tag{2.8}$$

The objective is to enhance a sequence of fuzzy cluster sets through a series of iterations using those equations until the objective function can no longer be further improved. The application of this method holds great potential for effectively detecting coastal upwelling, particularly when the area of interest exhibits distinct characteristics, featuring a cold and uniform zone in contrast to the warm and diverse offshore waters [El Aouni et al. [2015], Tamim et al. [2019]].

2.2 Review of existing approaches proposed for upwelling detection using classical methods

Recognizing the significance of locating coastal upwelling zones [Ryther [1969]], several studies have aimed to identify these cooler regions by employing various segmentation techniques. Among these methods, the application of edge detection approaches seeks to objectively outline genuine upwelling fronts within thermal infrared images while disregarding spurious edges [Cayula and Cornillon [1995], Sholva et al. [2013], Evans et al. [2005]]. An improved frontal detection algorithm, rooted in the method originally developed by [Cayula and Cornillon [1992]], was implemented in a study by [Nieto et al. [2012]] to detect mesoscale frontal structures in the Canary upwelling system. Furthermore, [Oram et al. [2008]] introduced a gradient-based edge detection approach designed to mitigate issues related to cloudiness in remote sensing images, thus enabling the automatic detection of significant upwelling features within the Southern California Bight region.

Some studies have explored the use of CHL-a images for upwelling segmentation. For instance, [Belmajdoub et al. [2022]], [Khalid et al. [2017]] and [El Aouni et al. [2015]] investigated ocean color satellite images to detect upwelling along the Atlantic coast of Morocco, utilizing techniques such as expectation-maximization, hard clustering, and fuzzy clustering, respectively.

Others have employed various algorithms to identify upwelling in SST images. [Cayula and Cornillon [1992]] presented an unsupervised classification approach using k-means clustering to train a neural network for this purpose. Additional studies, such as [Nascimento and Franco [2009a]], [Nascimento and Franco [2009b]], proposed algorithms based on the FCM technique to detect upwelling. [Sousa et al. [2008]] also utilized the FCM algorithm to identify upwelling regions in the coastal waters of Portugal.

In particular, some preliminary studies were conducted in the southern part of Morocco to identify and extract upwelling. In [Tamim et al. [2014b]], the FCM algorithm was employed in conjunction with adaptive clustering to partition and automatically extract upwelling, while another FCM technique with Gustafson-Kessel clustering was used in [Tamim et al. [2014a]] to identify upwelling in the same area. Both Otsu and region-growing algorithms were applied in [Tamim et al. [2013]] and [Tamim et al. [2014c]] respectively, to separate cold coastal upwelling from warmer offshore waters. The combination of these two algorithms was used in [Tamim et al. [2014d]] to locate upwelling from SST images. Additionally, [Tamim et al. [2019]] employed k-means and FCM techniques to automatically determine the appropriate number of clusters in SST images.

However, while these methods deliver precise segmentation in the southern part of the Moroccan Atlantic coast, they encounter limitations when aiming for robust segmentation across the entirety of the Moroccan upwelling system, encompassing the central and northern regions. The primary challenge stems from the significant variability in temperature distribution along the latitudinal axis. This variation is influenced by differences in solar energy distribution across the entire system, often leading to northern offshore temperatures resembling those observed in the southern upwelling regions. It is essential to emphasize that traditional clustering algorithms predominantly consider pixel temperatures, neglecting their geographical context. Consequently, these algorithms tend to misclassify northern offshore temperatures as indicative of upwelling water without considering their actual geographical location.

To overcome this challenge, recent literature has introduced two novel algorithms designed to identify and delineate upwelling regions along the Moroccan coast, particularly in the southern and central areas, using satellite-derived physical and biological observations. The initial approach proposed by [El Aouni et al.

[2020]] involves a natural comparison of coastal water temperature with offshore water temperature, evaluated perpendicular to the coastline. This approach entails normalizing temperatures based on latitude, with offshore temperatures playing a pivotal role (further details regarding this method and its segmentation results will be presented in the subsequent section, as these outcomes serve as a basis for the upcoming chapters). The second method, as proposed by [El Aouni et al. [2019]], adopts a region-specific clustering strategy, encompassing two fundamental stages. The initial stage aims to decompose SST images into coherent regions. Subsequently, a straightforward algorithm is developed to identify and merge pixel groups that best replicate the characteristic configuration of upwelling zones.

2.3 Upwelling extraction based on a nonlinear transformation

In this section, we will detail the method developed by [El Aouni et al. [2020]] to detect and track upwelling regions from SST and CHL-a images. This method can be summarized as follows steps :

2.3.0.1 Ekman pre-processing

The method described in El Aouni et al. [2020] is primarily based on the Ekman theory, which is the main driver of the upwelling phenomenon. As described in Ekman [1905], the movement of surface water to the right of the wind direction, caused by Ekman transport, can result in coastal upwelling in certain regions such as the northwest African margin. Therefore, to detect the occurrence of upwelling, it is common practice to compare the temperature/chlorophyll-a concentration of coastal water with offshore water. To incorporate this information into the preprocessing stage, a meridional normalization of SST/CHL-a images was proposed in El Aouni et al. [2020]. This normalization involves dividing the image into perpendicular lines along the coastline and comparing the temperature of coastal water with offshore water. Each line was normalized by dividing its temperature/chlorophyll-a concentration pixels by the maximal temperature/chlorophyll-a observed in the offshore region. This normalization step improved the identification of upwelling areas and preserved the thermal structures of the original image. Additionally, a moving average algorithm was applied to mitigate fluctuations in the vector of maximal temperatures/chlorophyll-a. The resulting normalized image (Fig. 2.1(b),(e)) exhibited clear distinctions between offshore and coastal information, enhancing the visualization and analysis of upwelling.

2.3.0.2 Segmentation

Once the images are normalized, the method proceeds by applying the FCM algorithm. They apply this algorithm with two classes to separate cold and nutrient-high water from the warmer in the offshore. Then make use of a region growing algorithm to remove the noises in the offshore and finally extract the upwelling region as shown in (Fig. 2.1(c),(f)) . We must mention that this is the segmentation method developed in El Aouni et al. [2020] allows us to identify the upwelling region form SST images over the whole Atlantic coast of Morocco, and this is mainly due to the physics taken into-account by their method. In our work we have also applied this method on CHL-a images.

2.4 Upwelling extraction based on Expectation-Maximization of CHL-*a* images.

In this section, we propose a simple, promising and intuitive tool dedicated to the identification and extraction of the upwelling region on CHL-a images covering the Atlantic coast of Morocco [Belmajdoub et al. [2022]]. Our method is based on the expectation-maximization algorithm to separate upwelling from non-

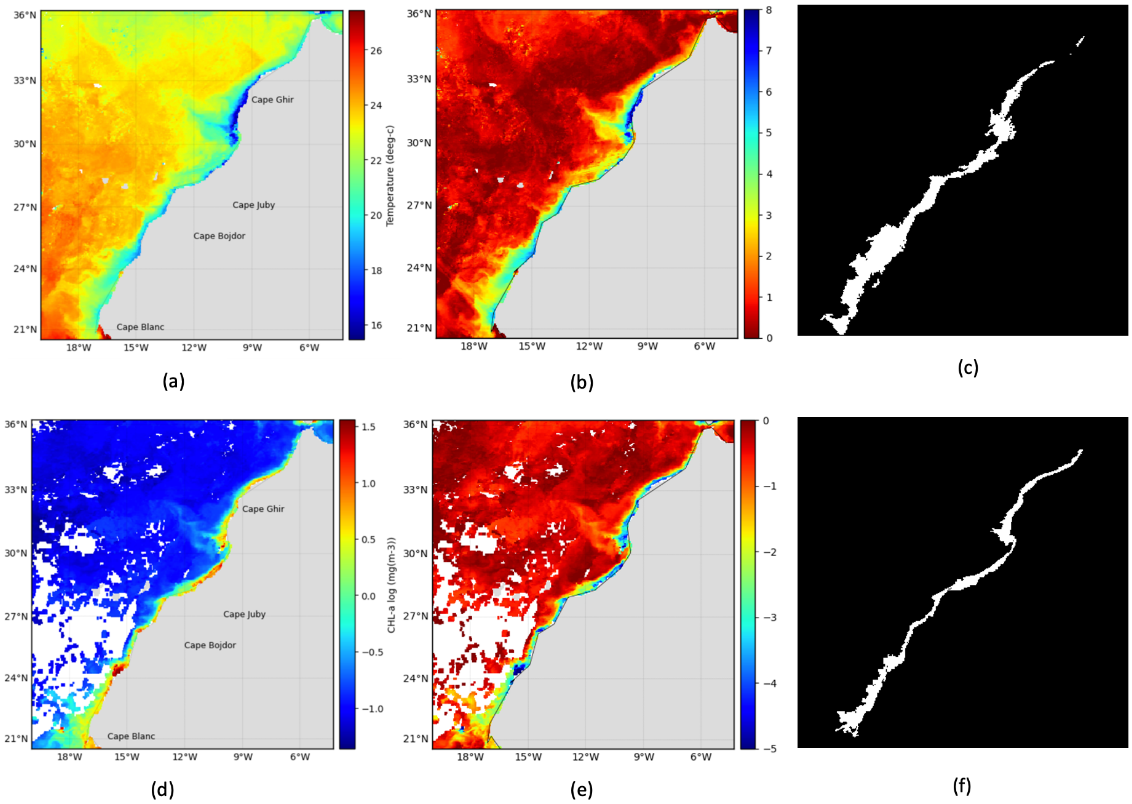

(a) (b) (c) (d) (e) (f)

Figure 2.1: (a):SST (C°), (b): Normalized SST image, (c): Result of segmentation for SST image, (d): CHL-a [$\log(mg/m^3)$], (e): Normalized CHL-a image, (f): Result of segmentation for CHL-a image.

upwelling regions. To eliminate noisy structures in offshore waters not belonging to the extracted area, a region growth algorithm is applied. The present work not only proposes a method for extracting Moroccan upwelling, but also provides the calculation and analysis of one of the famous upwelling indices based on CHL-a observation for the last five years (2016-2020).

2.4.1 Region of interest

The database used in this work is captured by the near-polar satellite TERRA-MODIS, from NASA's ocean color website (`http://oceancolor.gsfc.nasa.gov/`). Each satellite image is obtained from mean of 8 days, represented by a 378 × 378 pixel map with spatial resolution 4 × 4Km covering the Moroccan Atlantic coast spans from ($21°N$ to $36°N$ and $6°E$ to $19°E$). The weekly synthetic data allows to minimize the number of pixels contaminated by clouds, and build an agreement between the variability of pixel values and the necessity to provide continuous spatio-temporal coverage [El Aouni et al. [2015]]. In this study, we use 230 CHL-a images to supply a coarse segmentation of upwelling areas, during the period of $[2016 - 2020]$. Fig. 2.2 shows two CHL-a images selected from our database demonstrating upwelling scenarios encountered throughout this study. The gray color region on the CHL-a images in Fig. 2.2 corresponds to Moroccan land, and the white pixels in the ocean correspond to the cloud.

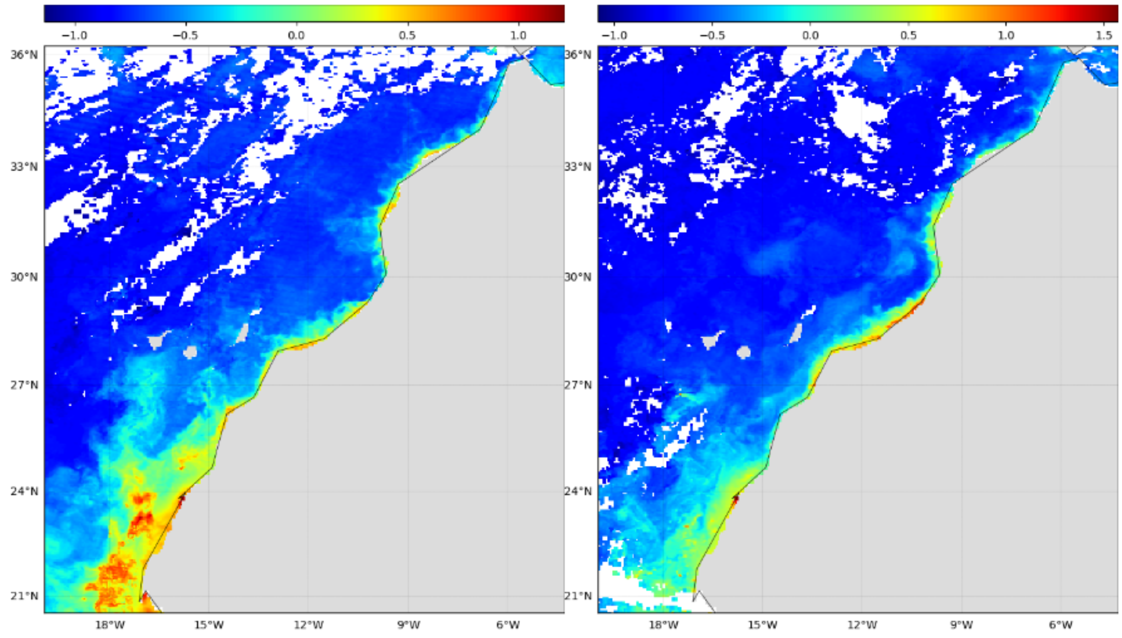

(a) (b)

Figure 2.2: Example of eight-day CHL-a $[\log(mg/m^3)]$ images selected from our database, showing a typical upwelling scenario from biological observations; (a):$[2016 - 01 - 01]$, (b):$[2017 - 02 - 09]$

2.4.2 Expectation-Maximisation algorithm

Expectation-Maximisation (EM) is a classification algorithm that relies on likelihood maximization to build adequate statistical models of the data [Bradley et al. [1998]]. It is usually used in artificial vision or in image processing, more specifically for segmentation (medical, satellite images, etc.). Or simply in clustering to provide labeled clusters sharing the same static properties. EM begins by estimating (step E) the missing information based on the current parameters. Followed by maximizing (step M), to find new estimates of these statistical parameters [El Assaad et al. [2016]]. In each step, we maximize the lower bound function, which yields estimates with higher likelihood than the previous iteration and eventually converges to a maximum.

With: K is the current number of Gaussians, σ is the standard deviation, θ^0 is the estimate at 0 iteration, μ is the mean, and ϵ threshold for the convergence of the algorithm.

In our model, the hidden variables are the mean and standard deviation of each Gaussian distribution. We begin by estimating these parameters and execute the algorithm iteratively to find the maximum likelihood for our estimates. For convergence, we execute it until the values stop increasing.

2.4.3 Optimal number of clusters

In unsupervised classification, determining the optimal number of clusters is a non-trivial task, as it is often not known beforehand. Selecting the appropriate number of classes requires careful consideration. Numerous methods have been proposed to automate the determination of the optimal number of clusters that best align with the data distribution [Griffa et al. [2007]]. In a study by [Tamim et al. [2014a]], the authors employed validity indices to evaluate different values of ”c” (the number of clusters) and assessed the quality of the resulting partition.

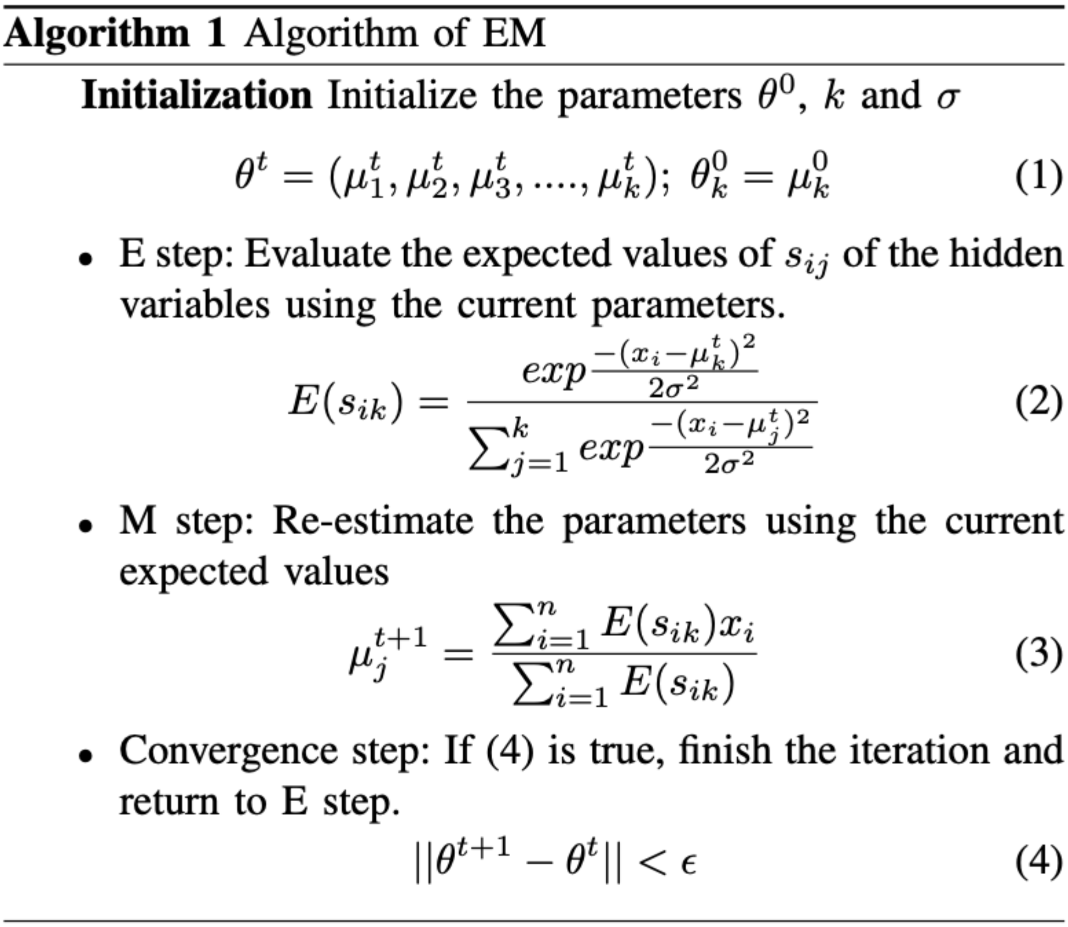

Algorithm 1 Algorithm of EM

Initialization Initialize the parameters θ^0, k and σ

$$\theta^t = (\mu_1^t, \mu_2^t, \mu_3^t, ..., \mu_k^t);\ \theta_k^0 = \mu_k^0 \qquad (1)$$

- E step: Evaluate the expected values of s_{ij} of the hidden variables using the current parameters.

$$E(s_{ik}) = \frac{exp\frac{-(x_i-\mu_k^t)^2}{2\sigma^2}}{\sum_{j=1}^{k} exp\frac{-(x_i-\mu_j^t)^2}{2\sigma^2}} \qquad (2)$$

- M step: Re-estimate the parameters using the current expected values

$$\mu_j^{t+1} = \frac{\sum_{i=1}^{n} E(s_{ik})x_i}{\sum_{i=1}^{n} E(s_{ik})} \qquad (3)$$

- Convergence step: If (4) is true, finish the iteration and return to E step.

$$||\theta^{t+1} - \theta^t|| < \epsilon \qquad (4)$$

Their findings indicated that "c = 2" provided the best fit for the characteristics of the studied region. Given the distinct features of the study area, characterized by significant and variable upwelling patterns throughout the year, and drawing upon their scientific and technical expertise, [Tamim [2015], El Aouni et al. [2015]] opted to set "c = 2" to effectively differentiate the colder coastal waters from the warmer offshore waters.

2.4.4 Region-Growing algorithm

The binary image results in Fig. 2.3 show the Upwelling area, with some noise structures in offshore waters not belonging to the upwelling region. For this, we

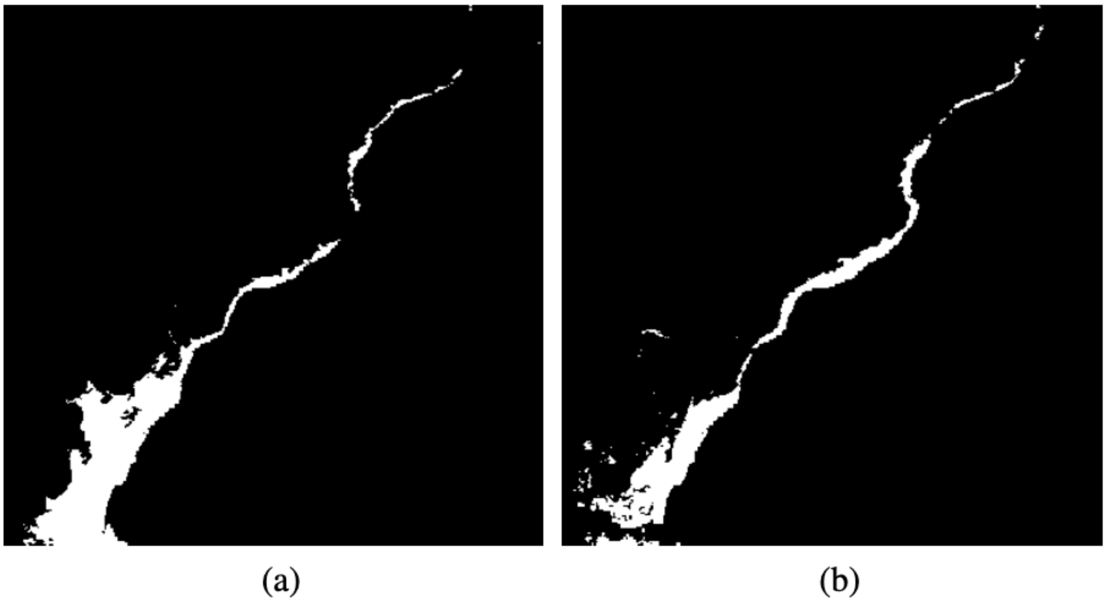

Figure 2.3: (a),(b): Upwelling area extracting by the EM method for the CHL-a images over the selected images of Fig. 2.2

apply to the binary images of upwelling detection another segmentation which consists in the application of the Region-growing algorithm to eliminate the isolated pixels in the offshore direction.

The segmentation approach is used to examine neighboring pixels of the initial seed points and to determine whether the adjacent pixel which should be added to the region Tamim et al. [2014d]. The segmentation aims at merging neighboring pixels to pixels inside the region according to homogeneity and adjacency criteria. This process is repeated until there are no more adjacent pixels to be included in a seeded region. In our case, we chose five seed points, so that each point belongs to an area of coastal upwelling of Morocco. These seeds are chosen near the coastline because all pixels pertaining to the upwelling must have connectivity to the coastline. The threshold is selected to obtain 2 regions with similar populations of pixels belonging and not belonging to the upwelling structures. The value of the threshold is fixed for all the databases. Fig. 2.4 shows the results of the proposed methodology applied on the CHL-a images in Fig. 2.2.

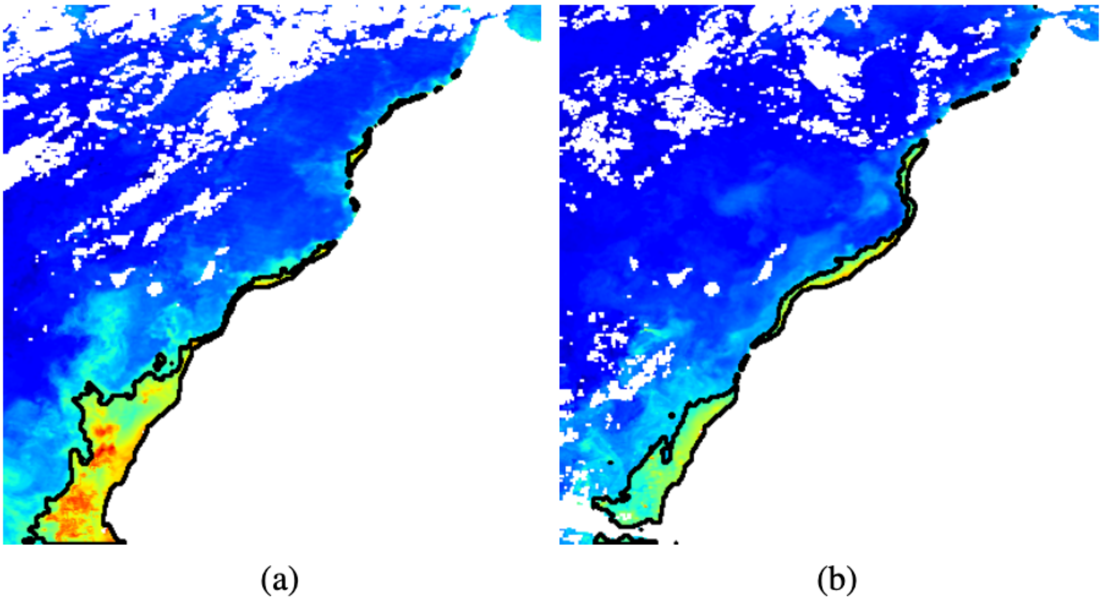

Figure 2.4: (a),(b): Upwelling region automatically contoured by edge canny using the proposed methodology over the selected images of Fig. 2.2

2.4.5 Experimental result and analysis

Based on the binary segmented CHL-a images, we explored the interannual variability of the upwelling along the Atlantic coast of Morocco. For this purpose, we computed the biological index of the upwelling.

2.4.5.1 CHL-a upwelling index

The CHL-a upwelling index (I_c) is determined as a product of the mean average of the upwelling CHL-a concentration and the extracted upwelling limit (equals the width of upwelling) over the same latitude. This approach was introduced by [Demarcq et al. [2007]]. The CHL-a index unit is expressed in ($mgm^{-3}km$).

In Fig. 2.5, we present a Hovmoller diagram illustrating the spatio-temporal resolution of the CHL-a index I_c. This visualization reveals substantial variations in the CHL-textita index I_c along the Moroccan coastline, both on an interannual and seasonal basis. It highlights instances of reduced phytoplankton biomass in specific years, such as 2018, and elevated biomass in others, notably in 2016 and 2020.

One noteworthy observation pertains to the marked latitudinal differences, consistently indicating lower I_c ($I_c < 24\, mgm^{-3}km$) values north of $33°N$ throughout the study period. Furthermore, discernible seasonal patterns emerge, with relatively modest I_c indices recorded during the summer months between $31°N$ and $27°N$. This pattern consistently manifests each year, signifying lower phytoplankton biomass and moderate upwelling intensity in this region. In sharp contrast, the zone spanning from $21°N$ to $24°N$ consistently exhibits elevated I_c values throughout most years and seasons. Notably, this region showcases some of the highest CHL-a index I_c values ($I_c > 150\, mgm^{-3}km$), characterized by distinct seasonal fluctuations when compared to other coastal areas. These elevated values of the index signify the persistent strength of upwelling throughout the study years. Remarkably, this extensive stretch of the Moroccan coast emerges as the primary hotspot for surface water phytoplankton content, with interannual variations underscoring its significance in the ecological dynamics of the region.

The I_c index accords generally the results obtained in El Aouni et al. [2019]. So, based on this index, we can validate the performance of the proposed methodology for the segmentation of the Moroccan coastal upwelling in CHL-a images. According to the findings, we can conclude that the proposed algorithm has provided satisfactory and promising results in terms of extraction and analysis of this important phenomenon.

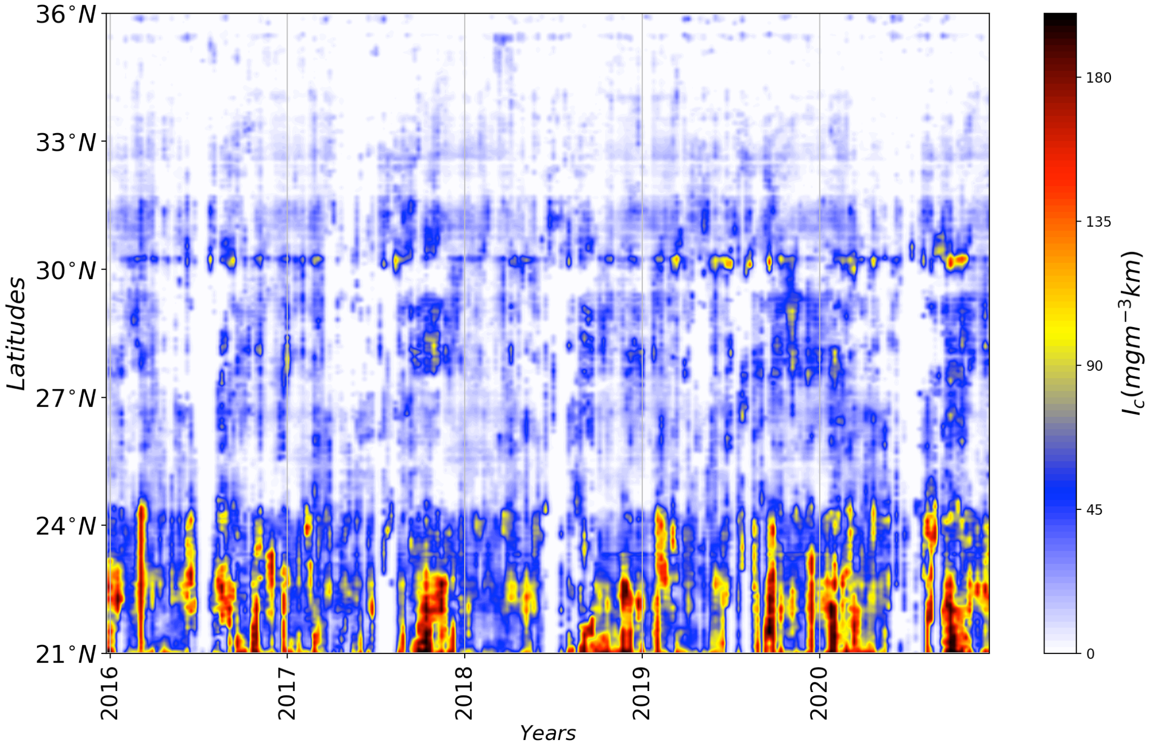

Figure 2.5: Space-time Hovmoller diagram of upwelling index (I_c) computed as CHL-a average multiplied by its extend over the $2016-2020$ period.

2.4.6 Conclusion

In this section, we proposed a segmentation method that aims to detect and extract the upwelling area in the coastal ocean of Morocco using the satellite observation of CHL-a concentration. To do this, first, we segmented the CHL-a images using the EM algorithm to effectively detect the main upwelling front along the Atlantic coast of Morocco, separating the nutrient-rich region and offshore waters. The second part consists of applying the region-growing algorithm process to eliminate isolated components,that appeared in offshore waters, not belonging to the upwelling structures. The algorithm is applied and tested over 230 CHL-a images covering the period between the years $2016-2020$. Lastly, we computed the CHL-a index (I_c) for validating quantitatively the segmentation results. Effectively, this index allowed us to study the seasonal and interannual climatology of the upwelling dynamics from biological observations.

Despite the availability of multiple methods for detecting coastal upwelling, these approaches face three primary challenges. Firstly, they tend to be time-consuming due to their reliance on optimization techniques. Secondly, their effectiveness is often highly dependent on the specific type of input data employed. Lastly, even the more recent upwelling detection method designed for the Moroccan Atlantic coast, as presented in [El Aouni et al. [2020]], encounters difficulties when accurately identifying the northern section of the Moroccan upwelling ecosystem within certain SST images.

To address these challenges and improve the ability to comprehensively monitor coastal upwelling phenomena, we are interested in integrating deep learning and artificial intelligence (AI) methodologies. These cutting-edge techniques offer a promising avenue for improving upwelling detection. By leveraging the power of deep neural networks and machine learning algorithms, we aim to overcome the limitations of conventional methods and develop a more robust, efficient, and accurate system for identifying and tracking upwelling events.

2.5 Artificial Intelligence: From Machine Learning to Deep Learning

Artificial Intelligence (AI) represents a branch of computer science with the primary objective of designing computer systems capable of performing tasks traditionally requiring human intellectual faculties. One of the most popular subfields of AI is machine learning, which is an approach based on a system's ability to learn from data without explicit programming for a specific task. Machine learning [Goodfellow et al. [2016]] is a subfield of artificial intelligence (figure. 2.6) and cognitive sciences that has evolved, transitioning from traditional methods such as decision trees, Bayesian networks, and Support Vector Machines (SVM) to more advanced and powerful approaches known as deep learning.

Deep learning, also referred to as deep neural networks, is a machine learning method based on artificial neural networks organized into multiple layers to extract complex features from input data.

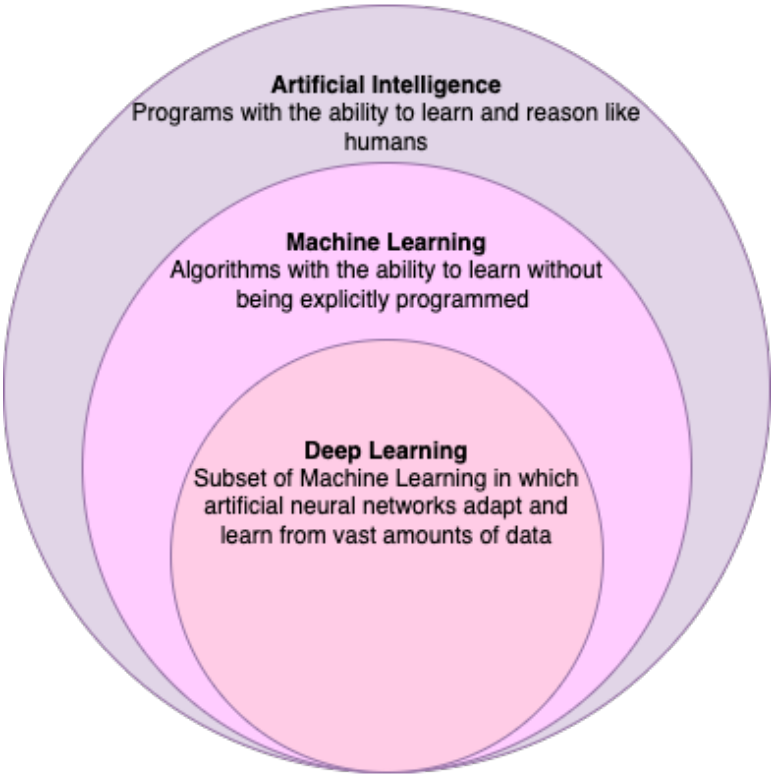

Figure 2.6: Comprehensive Visual Representation of Artificial Intelligence (AI) and Its Subfields.

2.5.1 Deep Learning: Advancing Beyond Machine Learning

Machine learning, a foundational subset of artificial intelligence (AI), is the process of employing algorithms and statistical models to enable computer systems to enhance their performance on a specific task without explicit programming. It achieves this improvement through iterative learning from data, allowing machines to make predictions, decisions, or classifications based on patterns learned from past information. Unlike traditional rule-based programming, where every instruction is explicitly provided, machine learning algorithms adapt and refine themselves as they encounter more data.

Deep learning, viewed as an evolutionary step beyond traditional machine learning, builds upon this foundation. It employs programmable neural networks to enable machines to make precise decisions autonomously, often without human intervention.

A fundamental distinction between traditional machine learning and deep learning lies in data representation. In traditional machine learning, features are manually extracted from data to train the model, while deep learning models autonomously learn relevant features from raw input data [LeCun et al. [2015]]. This autonomy renders deep learning models more adaptable and proficient at acquiring complex hierarchical representations from unprocessed data. Consequently, deep learning excels in intricate tasks such as image recognition, machine translation, speech recognition, and more.

In recent years, deep learning has undergone remarkable advancements, particularly with the Convolutional Neural Networks (CNNs) for computer vision tasks and Recurrent Neural Networks (RNNs) for natural language processing. These deep neural network architectures have consistently achieved state-of-the-art performance in various machine learning tasks, frequently outperforming traditional methods.

It is imperative to acknowledge that deep learning typically demands substantial quantities of training data to yield high-quality results, along with adequate computational resources for model training. However, ongoing advancements in computing technologies and the increasing availability of data have propelled the progress of deep learning, expanding its applications across numerous scientific, industrial, and societal domains.

In summary, machine learning forms the foundation upon which deep learning is built. Machine learning involves the use of algorithms and statistical models to enable computers to learn and improve their performance from data, while deep learning, an advanced form of machine learning, employs neural networks to autonomously learn complex hierarchical representations from raw data, leading to breakthroughs in various AI domains.

2.6 Semantic segmentation

Semantic segmentation is a specialized area within computer vision that concentrates on dividing an image into different sections, with each section representing a predetermined class or label. This approach differs from object detection, which identifies and surrounds objects with bounding boxes, and image classification, which allocates a singular label to the whole image. Instead, semantic segmentation seeks to attain a more refined comprehension by attributing a label to every individual pixel in the image. This facilitates a comprehensive depiction of objects along with their limits, rendering it an essential operation in numerous applications of computer vision.

2.6.1 Advancements in Semantic Segmentation Methods

During the initial phases of semantic segmentation, traditional computer vision methodologies were predominant, primarily focusing on the use of handcrafted features. Classical algorithms, including SVM and Random Forests, were crucial for classifying these features into various semantic categories [Shotton et al. [2008]]. Techniques like thresholding and clustering were commonly employed for initial image segmentation into potential segments, and feature selection methods were utilized to meticulously choose discriminative features for segmentation tasks. Nonetheless, these conventional methods faced limitations, notably their dependence on manual feature engineering and selection and their challenges with handling variations in lighting, orientation, and scale encountered in real-world imaging scenarios.

The advent of Neural networks marked a significant transition in semantic segmentation, bringing forth new challenges and facilitating the emergence of advanced models to address them. Within the realm of image segmentation tasks, semantic segmentation for remote sensing images has emerged as a notable subfield. Upwelling segmentation, a specialized form of semantic segmentation, finds diverse applications in scenarios like identifying and delineating upwelling zones in oceanographic data, contributing to climate research, mapping oceanographic features, and understanding marine ecosystem dynamics. These applications underscore the growing significance of upwelling segmentation within the broader landscape of image analysis and remote sensing, particularly in the domain of oceanography and environmental science.

The most successful deep learning architectures for semantic segmentation are typically characterized as encoder-decoder architectures. In this framework, the encoder is often a pre-trained classification network. Its role is to capture essential features from the input image. Subsequently, the decoder part takes on the responsibility of semantically projecting these discriminative features from the encoder onto the pixel space, enabling the dense classification of each pixel in the image.

One of the pioneering deep convolutional neural networks introduced for semantic segmentation is the Fully Convolutional Network (FCN). However, the field has witnessed the development of more advanced FCN-based approaches aimed at enhancing segmentation accuracy and robustness. Notable examples of these advanced approaches include SegNet [Badrinarayanan et al. [2017]], U-Net [Ronneberger et al. [2022]], and PSPNet [Zhao et al. [2017]], which have been proposed to address specific challenges associated with semantic segmentation. These innovations collectively represent the progression of deep learning techniques in the domain of image segmentation.

2.7 Convolutional Neural Network

Convolutional Neural Network, also known as ConvNet, is a specialized type of artificial neural network designed for processing and analyzing visual data, such as images and videos. CNNs have been remarkably successful in various computer vision tasks, including image classification, object detection, image segmentation, and more.

2.7.1 Architecture of a convolutional neural network

CNN typically consists of three components, illustrated in Figure. 2.7 a convolutional layer, a pooling layer, and a fully connected layer. CNN blocks are often repeated multiple times within a CNN architecture to form a deep neural network capable of learning complex representations of the data [Rhee [2018]].

Input layer: This layer receives the raw input data, often in the form of an image with channels. Each channel represents different features of the image.

Convolution Layer: The convolutional layer is the central building block of a Convolutional Neural Network (CNN), utilizing the convolution operation (represented by *) in place of the general matrix multiplication. Its parameters consist of a set of learnable filters, also referred to as kernels. The primary task of the convolutional layer is to detect features present in local regions of the input image that are common across the entire dataset and to match their appearance with a feature map. A feature map is obtained for each filter in the layer through repeated

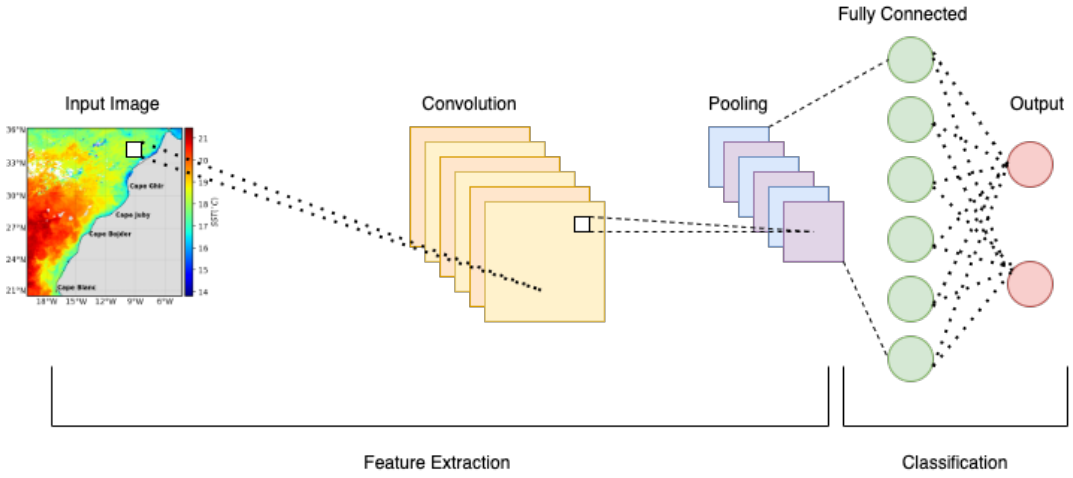

Figure 2.7: CNN Architecture.

application of the filter over subregions of the complete image, i.e., by convolving the filter with the input image, adding a bias term, and subsequently applying an activation function. The input region on which a filter is applied is referred to as the local receptive field. The size of the receptive field is the same as that of the filter. Figure 2.8 illustrates how a filter is convolved with the input to obtain the feature map. The weights of each convolutional layer specify the convolution filters, and there may be multiple filters in each convolutional layer. Each filter encapsulates a specific feature, such as an edge or a corner, etc., and during the forward pass, each filter is slid across the width and height of the input, generating the feature map for that filter.

Neural Convolutional Network Architecture involves numerous hyperparameters that are employed to control the model's behavior. Some of these hyperparameters govern the output size, while others regulate execution time and memory cost. Within the convolutional layer of ConvNets, four pivotal hyperparameters are detailed as follows:

- Filter Size: Filters can assume sizes greater than 2×2 and less than the

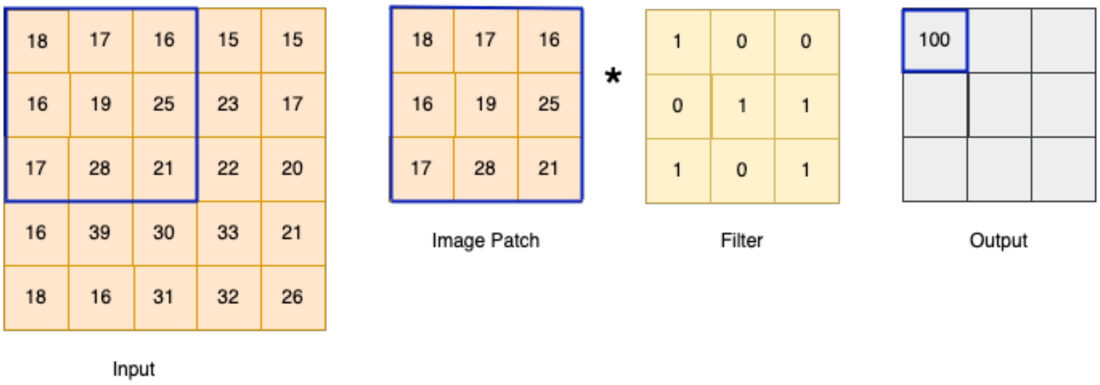

Figure 2.8: Example of the convolution operation.

input size. The filter size remains independent of the input size.

- Number of Filters: Any reasonable number of filters may be employed.
- Stride: This parameter represents the number of pixels to shift at a time to define the local receptive field of a filter. A stride of one entails a one-pixel movement from top to bottom.

  Padding: An essential hyperparameter, denotes the number of zero pixels to add to the input image. Zero padding is employed to manage the spatial size of the output volume.

Activation Function: Each convolutional layer transmits its output to an activation function layer. This layer encompasses a function that takes the feature map produced by the convolutional layer as input and generates an activation map as output. The activation function transforms the activation level of a neuron into an output signal, determining the neuron's output for a given input. Typically, an activation function performs a transformation effect, involving a mathematical operation on the input, resulting in a neuron's activation level within a value range, such as between 0 and 1 or between -1 and 1.

Several activation functions are employed with artificial neural networks (ANNs). Some commonly utilized activation functions include:

- Logistic/Sigmoid Activation Function: The sigmoid function is mathematically represented as $\sigma(x) = 1/(1 + \exp(-x))$. It compresses the input into the [0, 1] interval.

- Hyperbolic Tangent Activation Function (tanh): Similar to the sigmoid function, the tanh function maps inputs to the [-1, 1] interval. Its advantage over the sigmoid function is that negative inputs are strongly negative, and zero inputs are close to zero.

- Softmax Function (Exponential Function): Often used in the output layer of a neural network for classification tasks, it is mathematically represented as $\sigma(x_j) = \exp(x_j)/\sum_{k=1}^{n} \exp(x_k)$. The softmax function is a more generalized logistic activation function, particularly useful for multi-class classification.

- Rectified Linear Unit (ReLU): ReLU calculates activation by thresholding input at zero. In other words, a ReLU unit has an output of zero if the input is less than zero, and it outputs the input value otherwise. Mathematically, it is expressed as $f(x) = max(x, 0)$.

Pooling: In CNN, the sequence of the convolutional layer and activation function layer is typically followed by an optional layer for spatial downsampling, aimed at reducing the input's spatial dimensions and consequently, the number of network parameters. This layer is commonly referred to as a pooling or subsampling layer. In a pooling layer, each output feature map from the convolutional layer undergoes subsampling, which means that the pooling layer aggregates information within a region of neurons from the convolutional layer. Various pooling techniques exist, with max-pooling being the most prevalent. Max-pooling simply selects the maximum value within a specified input region. For instance, when the input region is 2 × 2 in size, the max-pooling unit [Sardogan and Ozen [2018]] will output the maximum value among the four input values, as illustrated in Figure2.9. Other alternatives for pooling layers include average pooling and L2-norm pooling. The pooling layer operation discards less significant data while preserving detected features in a more compact representation. The intuitive rationale behind pooling is that feature detection holds greater importance than their precise spatial locations [Sardogan and Ozen [2018]].

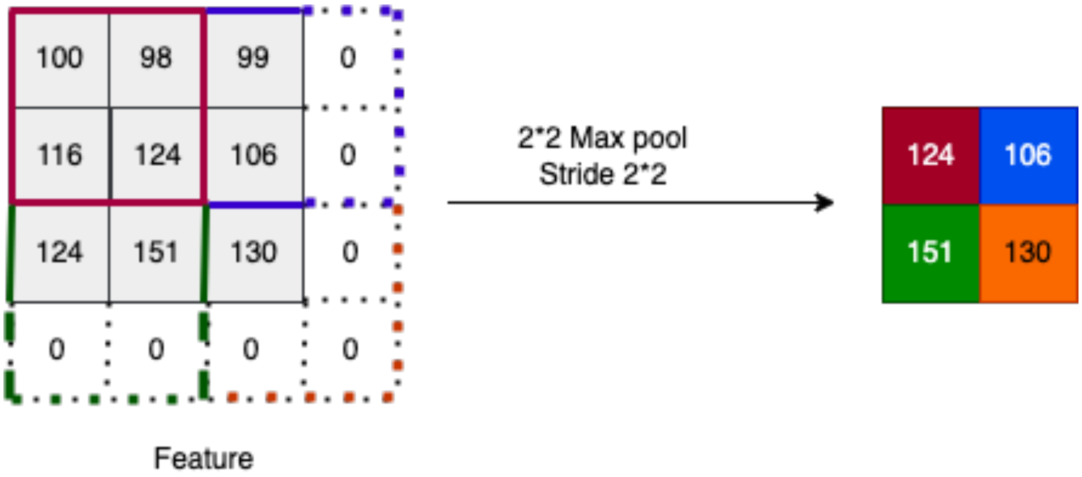

Figure 2.9: Example of Max pooling with 2 × 2 filters and stride 2.

Fully connected layer: After several convolutional and pooling layers, CNNs often include one or more fully connected layers. These layers perform high-level feature extraction and are typically followed by a softmax activation function for classification tasks.

2.7.2 Limitations of CNNs in Semantic Segmentation

Although CNNs have played an essential role in advancing the field of semantic segmentation, they present several difficulties. One of the main constraints is their computational cost. The deep nature of CNNs often requires substantial computing power, making them sub-optimal for real-time applications or implementations on devices with restricted capabilities [Carreira et al. [2012]]. In addition, managing scale and orientation is another obstacle. Although several architectures have endeavored to solve this problem, the efficient capture of contextual information at multiple scales remains a major challenge [Chen et al. [2018]]. In addition, CNNs generally require a considerable volume of annotated data to train effectively. This becomes particularly problematic in specialized fields such as satellite imagery, where acquiring such data can be both time-consuming and limited.

2.8 Fully Convolutional Neural Network

FCN [Long et al. [2015]] is a type of deep learning architecture designed for semantic segmentation and pixel-wise classification tasks in computer vision. Unlike traditional CNNs used for image classification, which output a single label or class for an entire image, FCNs preserve spatial information by producing dense pixel-wise predictions.

Key characteristics of FCNs include the absence of fully connected layers and the use of transposed convolution (also known as deconvolution or up-sampling) layers to increase the spatial resolution of feature maps [Long et al. [2015]]. FCNs take an input image and pass it through a series of convolutional and pooling layers to extract hierarchical features. Then, they use transposed convolution layers to up-sample the feature maps and generate pixel-level predictions, often in the form of segmentation masks ensuring that the output retains the original input size (see

Figure 2.10).

FCNs have been instrumental in tasks like semantic segmentation, where each pixel in an image is assigned a semantic label (e.g., ”car,” ”tree,” ”road”) to provide a detailed understanding of the scene. Their ability to produce high-resolution segmentation maps while preserving spatial information makes FCNs a powerful tool in various computer vision applications, including object detection, image segmentation, and image-to-image translation. Notable examples of semantic segmentation methods based on FCNs include ParseNet, DeconvolutionNet, and U-Net.

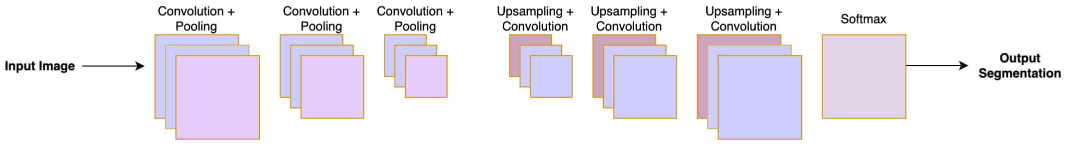

Figure 2.10: FCN Architecture.

2.8.1 Limitations of FCN in Semantic Segmentation

Despite their transformative impact, FCNs possess several limitations. One of the main challenges is the loss of spatial resolution due to layer pooling, which can lead to less precise boundary delineation. Although some [Long et al. [2015]] variants attempt to remedy this problem by using skip connections or higher sampling layers, the problem is not entirely solved [Long et al. [2015]]. In addition, FCNs can be computationally intensive, requiring significant memory and processing power, which is not always possible for real-time applications or devices with limited resources. In addition, like traditional CNNs, FCNs often depend on large sets of labeled data for learning, which can be a bottleneck in domains where such data is scarce or expensive to obtain.

2.9 Encoder-Decoder Architectures

Encoder-Decoder architectures are pivotal structures in neural networks and have emerged as a fundamental component in semantic segmentation, especially in tasks necessitating high-resolution output maps, and are also prevalent in machine translation and various applications aiming to convert input sequences to output sequences of varying lengths or structures [Sivagami et al. [2020a]]. These architectures are generally divided into two main components: the encoder and the decoder. The encoder captures semantic information using convolutional and pooling layers. It compresses this information into a condensed context vector, a compact, essential representation of the input. The decoder uses this context vector to reconstruct spatial information. It translates it into the desired output format using up-sampling and convolutional layers. This transforms the condensed representation into meaningful output, like a segmentation map. A prime example of this architecture is the U-Net in semantic segmentation. In this model, the encoder extracts hierarchical features from the input image. The decoder then uses these features to create a detailed segmentation map. This architecture often features symmetry between the encoder and the decoder. It includes skip connections to preserve spatial information and aid gradient flow during training.

2.9.1 U-Net

The U-Net architecture, introduced in 2015 by Ronneberger, Fischer, and Brox, is a seminal convolutional neural network design primarily developed for biomedical image segmentation tasks [Ronneberger et al. [2015]]. Characterized by its distinctive U-shaped architecture comprising a contracting and expansive path, U-Net has proven exceptionally effective in preserving fine-grained spatial information through the innovative use of skip connections. While originally devised for cell and tissue image analysis, its versatility has led to widespread adoption in diverse domains beyond biomedicine, and its impact continues to shape the development of deep learning models for image segmentation, making it a significant milestone in the field of computer vision and convolutional neural networks. Training a U-Net follows the general principles of training neural networks. Initially, the network's trainable parameters are initialized randomly. Subsequently, the network is presented with an input image, from which it generates a prediction map using these random parameters. This prediction map is then compared to a one-hot-encoded segmentation mask of the input image, which represents the ideal segmentation blueprint. This comparison is facilitated by a loss function, often categorical cross-entropy, to quantify the prediction error. The computed loss, serving as a measure of prediction accuracy, is propagated backward through the network to iteratively update the trainable parameters, aligning them in a direction that minimizes prediction error. This process repeats for successive input images as long as the prediction error continues to decrease. Over time, the U-Net effectively learns the capacity to process new input images and generate precise segmentation maps based on their content. In the illustration presented in Figure.2.11, we observe a representative depiction of the U-Net architecture as initially introduced by [Ronneberger et al. [2015]].

2.9.2 Advantages of U-Net Architecture for Upwelling Segmentation

The choice of U-Net architecture for upwelling segmentation stands out for its exceptional ability to preserve high resolution, its adaptability to irregular shapes and its minimal risk of excessive smoothing. Unlike other solutions, U-Net's encoder-decoder structure excels at capturing both low-level and high-level features of the input data, which is important for the variable visual characteristics of upwelling regions. Its jump connections ensure that fine-scale detail is retained, making it

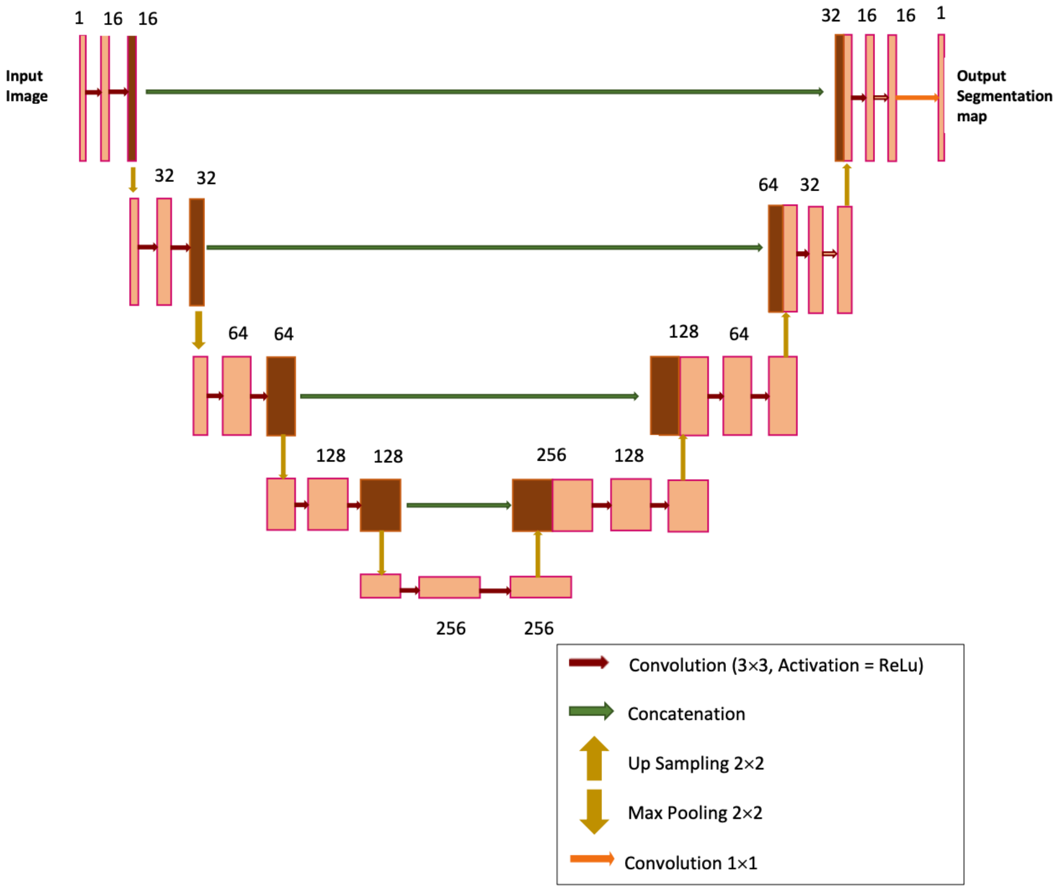

Figure 2.11: Illustration of the U-Net Architecture

ideal for accurately delineating complex upwelling boundaries. These advantages make U-Net a robust choice, adapted to the nuanced requirements of upwelling segmentation.

2.9.3 Comprehensive Review of U-Net Applications in Satellite Imagery

The U-Net architecture has been widely adopted for semantic segmentation in remote sensing and satellite imagery. [Dechesne et al. [2021]] developed a Bayesian U-Net model to estimate uncertainty in semantic segmentation of Earth observation images, achieving high accuracy on several state-of-the-art datasets. [Li et al.

[2022]] proposed a multiscale skip connected and asymmetric-convolution-based U-Net (MACU-Net) for segmentation of fine-resolution remotely sensed images, demonstrating superior performance over standard U-Net and other benchmark approaches. [Türkmenli et al. [2021]] utilized U-Net as a deep feature extractor in a superpixel-based graph convolutional network for accurate segmentation of SAR images from the Sentinel-1 satellite. [Mohajerani et al. [2019]] modified the U-Net architecture to automatically detect glacier calving front margins in satellite imagery. [Niu et al. [2022]] introduced the fusion coordinate and asymmetry-based U-Net (FCAU-Net), incorporating a coordinate attention mechanism and an asymmetric convolution block, achieving high accuracy on public datasets.

Focusing on SST and CHL-a concentration in satellite images, [Lambhate et al. [2021]] developed a W-Net, a variant of U-Net, to identify the Gulf Stream and rings from concurrent satellite images of SST and sea surface height (SSH). [Barth et al. [2022]] utilized a U-Net type network, DINCAE 2.0, to reconstruct SST, CHL-a concentration, and wind fields in satellite data. [Snoussi et al. [2023]] employed a deep residual U-Net for automatic detection of Moroccan coastal upwelling using SST images. [Yang et al. [2023]] utilized a residual network (ResNet) model to estimate chlorophyll-a concentrations from HY-1C satellite data, showcasing superior performance compared to other machine learning models. This approach, coupled with the U-Net architecture, can potentially enhance the precision of semantic segmentation tasks in detecting CHL-a concentrations and SST anomalies in global oceans. Furthermore, [Liu and Li [2023]] integrated a long time series of satellite-derived SSH and SST data using a deep learning model to study eddy-induced CHL-a variations in the Northern Indian Ocean, revealing the profound impact of mesoscale eddies on phytoplankton distribution. Moreover, a multi-modal U-Net model proposed by [Liu et al. [2020]] has been pivotal in detecting mesoscale eddies from multi-source remote sensing images, including CHL-a

images, enhancing the accuracy and efficiency of eddy detection by using fusion data of SSH and SST.

2.10 Conclusion

In conclusion, this chapter has looked at the various methodologies implemented in the segmentation of upwelling regions from SST and CHL-a images, focusing on their extensive applications in the Northwest African region. Initially, we traversed conventional image processing approaches, meticulously examining various methods to understand their capabilities and limitations in detecting upwelling phenomena. This investigation revealed that, while these conventional methodologies are largely suitable for upwelling identification, they do have certain limitations and face challenges in accurately, and efficiently identifying upwelling. To address the challenges and limitations inherent in conventional approaches, this chapter explores the vast and promising field of DL and AI. This exploration was motivated by the aspiration to leverage the advanced capabilities of deep neural networks and state-of-the-art machine learning algorithms to increase the accuracy, efficiency and robustness of upwelling detection mechanisms. This exploration has highlighted the fact that the integration of deep neural networks and artificial intelligence can significantly improve the upwelling detection process, offering more sophisticated and reliable solutions than conventional approaches.

Chapter 3

CONVOLUTIONAL NEURAL NETWORKS FOR COASTAL UPWELLING MONITORING FROM BIOLOGICAL AND PHYSICAL SATELLITE IMAGES.

3.1 Introduction

This chapter presents new deep learning techniques for monitoring and improving the identification of upwelling regions using physical and biological satellite data. Comprising three distinct contributions, this chapter begins with the implementation of a customized CNN-Unet architecture inspired by the U-Net design [Belmajdoub et al. [2023a]]. This technique focuses on the precise detection and accurate localization of upwelling regions in designated geographical areas. Subsequently, a refinement strategy involving deep residual networks (ResNets) is introduced, further improving the accuracy of upwelling detection under the name ”DeepRes-UpwellNet” [Belmajdoub and Minaoui]. The chapter culminates with the introduction of ”DeepCoast$_{up}$-Net”, an architecture designed for the complete identification of upwelling regions in major coastal areas, effectively exploiting the potential of SST satellite imagery [Belmajdoub et al.].

3.2 CNN-Unet for Upwelling extraction from SST and CHL-*a* images

In this section, we propose new deep learning tools to monitor the Moroccan upwelling from biological and physical satellite images [Belmajdoub et al. [2023a]].

The proposed method consists of a CNN based on an encoder-decoder built on the U-Net structure, to localize the upwelling regions. Using the U-Net architecture for the segmentation of Moroccan upwelling regions is advantageous over previous methods. It allows for efficient feature extraction and high-level feature recognition, resulting in more accurate predictions of the upwelling regions. It is also robust to noise and variability commonly found in satellite images of the ocean and can handle large datasets, which is essential for the segmentation of upwelling regions that require processing a large number of satellite images.

3.2.1 dataset

The focus of our study is the coastal region of the Atlantic Ocean in Morocco, spanning from latitude $21°N$ to $36°N$ and longitude $6°E$ to $19°E$. The dataset utilized in this research comprises 1818 images, including SST and CHL-a images, covering the period between [2000-2019]. Each SST/CHL-a image in the dataset consisted of 384 ×384 pixels. These images, along with their corresponding segmentation masks, serve as input data for our network. To handle terrestrial, cloudy or sparsely populated regions, we have replaced the standard fill value with zero, thus mitigating outliers. This adjustment has no impact on the upwelling detection process, as upwelling pixels are generally located in regions where the SST/CHL-a values are non-zero.

To generate the segmentation masks, we utilize a recent method proposed by [El Aouni et al. [2020]]. This method is specifically designed to identify and extract upwelling regions from both the SST and CHL-a images. It has proven to be effective in resolving the challenges faced by previous methods when attempting to identify the central part of the Canary Upwelling Ecosystem from SST images.

Figure 3.1 provides an illustrative representation of the aforementioned products used in this study. Panel (a) depicts an SST image expressed in degrees

Celsius and its corresponding mask , while panel (b) displays a CHL-*a* image, with the pixel values representing the amount of chlorophyll in milligrams per cubic meter of seawater and its corresponding mask. Both images were acquired on the same date, but the CHL-*a* image exhibits a higher presence of clouds (indicated by the white color) in comparison to the SST image. This discrepancy can be attributed to variations in wavelengths and the pre-processing algorithms employed in generating these datasets.

The aforementioned image features, along with the corresponding masks, will remain essential elements in subsequent contributions, forming the basis for learning our models.

3.2.2 Architecture

The primary goal of our study is to identify and monitor upwelling regions using SST and CHL-*a* images. To achieve this, we employed a CNN architecture known as U-Net. An overview of the proposed approach is presented in Figure 3.2. Initially, the CNN model is trained to classify the images into SST or CHL-*a* categories. Subsequently, the U-Net architecture is utilized for image segmentation purposes.

The U-Net architecture, originally designed for biomedical image segmentation, has found broad applicability, including in satellite imagery for identifying upwelling regions. This CNN-based model comprises an encoder network for down-sampling the input image and a decoder network for up-sampling the encoder's output, ultimately generating a segmentation map with the same dimensions as the input image. The encoder, constituting the first half of the architecture, is composed of multiple convolutional layers followed by a max pooling layer.

In the U-Net architecture, each convolutional layer employs a 3×3 kernel, and the number of filters starts relatively small (e.g., 16) and increases progressively

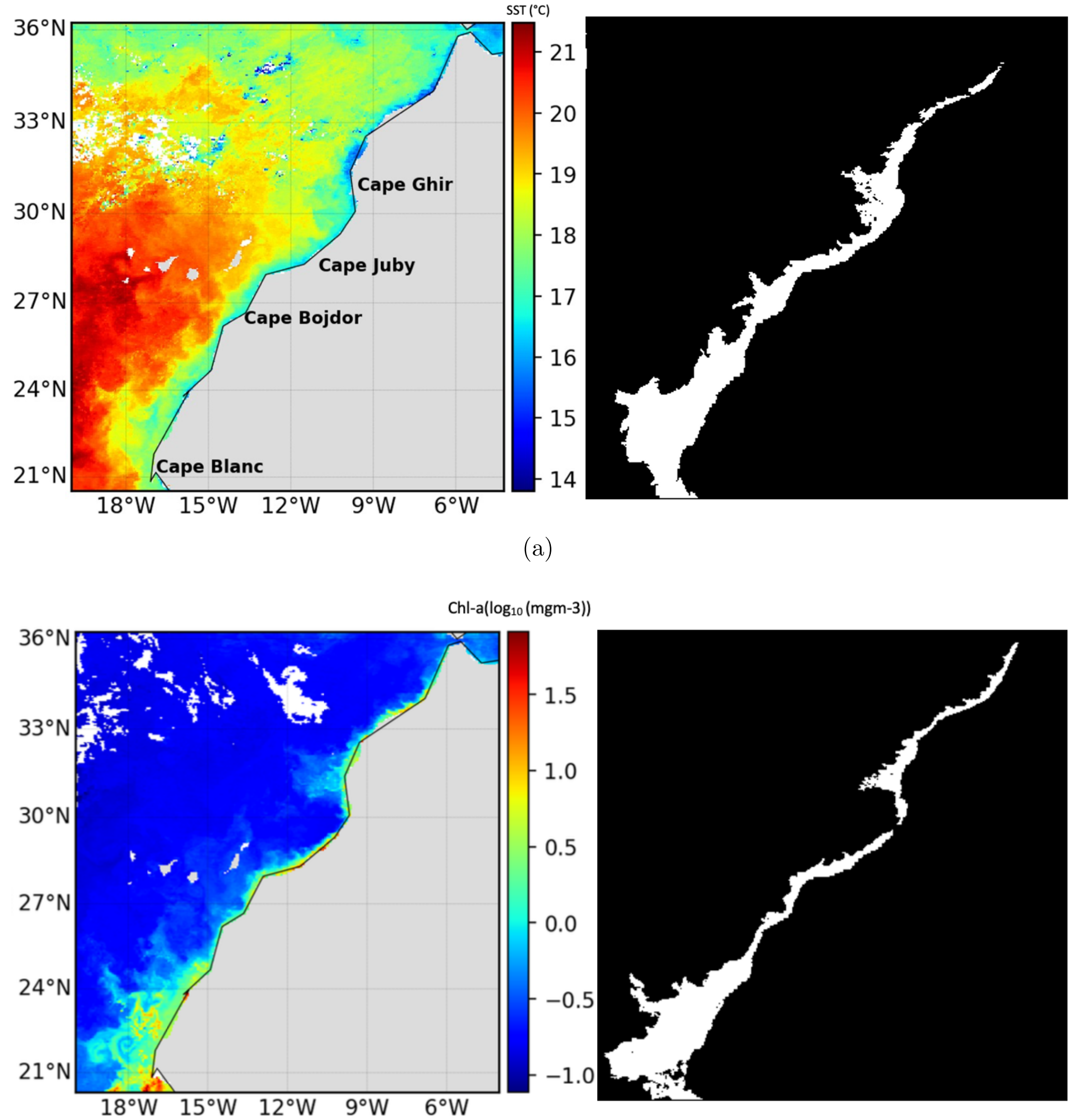

(a)

(b)

Figure 3.1: (a) SST (°C) and (b) CHL-a [$\log_{10}(mgm^{-3})$] images selected from our database.

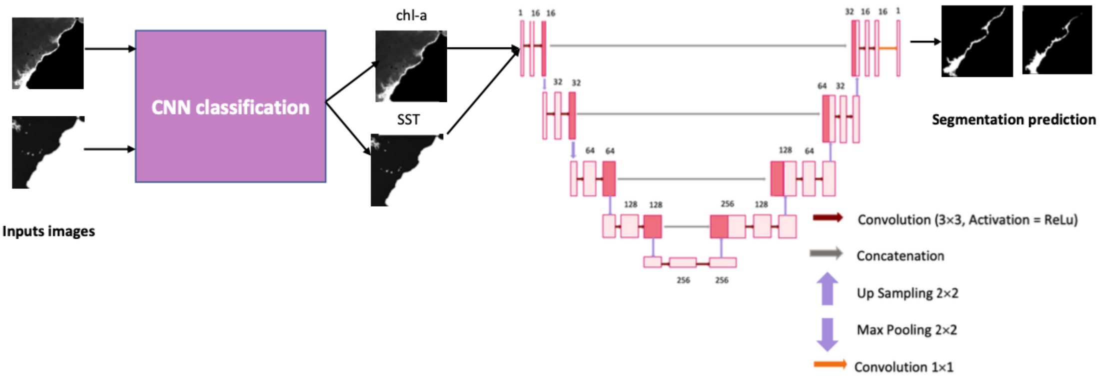

Figure 3.2: Overview of the proposed methodology using U-Net architecture to extract and identify upwelling along the Atlantic coast of Morocco from SST and CHL-a images.

by a factor of two after each max pooling operation until reaching 256. Batch normalization is applied after each convolutional layer to normalize the output and facilitate the training process [Ioffe and Szegedy [2015]]. The max pooling layer is instrumental in reducing the input image's spatial resolution, enabling the network to learn higher-level features in the deeper layers.

The output of the encoder comprises feature maps with reduced spatial resolution and increased channel count, which are subsequently fed into the decoder. The decoder includes upsampling layers, achieved using transposed convolutional layers (also called deconvolutional or fractionally strided convolutions), to increase the feature maps' spatial resolution while decreasing the number of channels. After each upsampling operation, a convolutional layer combines information from both the encoder and the decoder. These convolutional layers use 3 × 3 kernels and are followed by batch normalization and ReLU activation [Harrison et al. [2021]]. These operations aim to extract more abstract features and enhance the output's discriminative power.

Finally, a softmax function is applied to the decoder's output, resulting in a probability distribution for each pixel in the image, indicating the likelihood of belonging to either the upwelling or non-upwelling class. Thresholding the probabilities generate a binary mask, yielding the final segmentation map that identifies the upwelling regions in the input image (refer to Figure 3.3).

3.2.3 Experiment

The CNN-Unet model is trained using a dataset comprising input images and their corresponding segmentation masks. The ADAM optimization function is utilized with an initial learning rate set at 0.0001, and the training process spans 500 epochs. The dataset is partitioned into 75% for training and 25% for testing purposes.

The results depicted in Fig 3.3 demonstrate that the U-Net architecture outperforms the classical method in detecting upwelling regions for both SST and CHL-a images. Specifically, the U-Net architecture exhibits notable effectiveness in identifying upwelling in the northern region, particularly in the SST image where the classical method falls short.

3.2.4 Validation

To validate the segmentation accuracy, our algorithm, as well as the algorithm proposed by [El Aouni et al. [2020]], are applied to 92 SST images and 92 CHL-a images captured during two consecutive years (2020-2021). The assessment of the results is conducted by computing the validation upwelling index (Vup) as introduced by [El Abidi et al. [2020]]. The obtained Vup results are presented in Table 3.1.

Validation Upwelling Index Computation: Vup is defined as follows:

$$Vup = \frac{Number_{NP}}{L_I * Number_I} \tag{3.1}$$

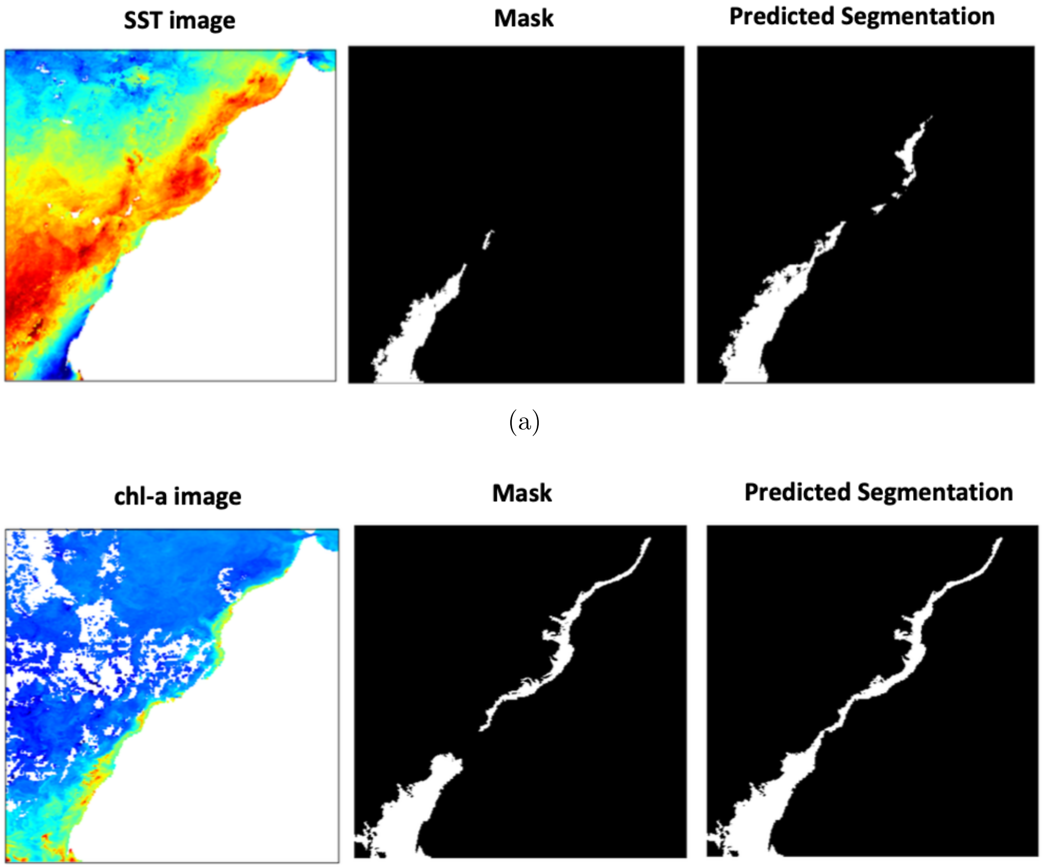

(a)

(b)

Figure 3.3: Result of segmentation obtained by applying the U-Net structure to (a) SST and (b) CHL-a images.

where ”$Number_{NP}$” is the number of correctly classified latitude steps obtained from the CHL-a and SST images. More precisely, it represents the cumulative sum of correctly classified values for all years analyzed. The ”L_I” in equation 3.1 corresponds to the number of latitude steps in the Moroccan Atlantic coast area, while ”$Number_I$” represents the total number of images processed (92). The results of the upwelling index validation (V_{up}) are presented in Table 3.1.

The index obtained strongly validates the effectiveness of our approach in accurately delineating the main Moroccan upwelling fronts. For CHL-a and SST,

	time	V_{up}
Proposed methodology	3s	SST= 78.30%; CHL-a= 78.97%
Methodology of El Aouni et al. [2020]	1min9s	SST= 76.74%; CHL-a= 77.88%

Table 3.1: Results of V_{up} on the proposed methodology and the methodology of [El Aouni et al. [2020]] on SST and CHL-a images from 2020 to 2021.

our approach produces a remarkable improvement of over 2% in the V_{up} compared to the method developed by [El Aouni et al. [2020]]. In addition, the proposed procedure effectively solves the problem of upwelling detection in the northern region, particularly for SST images where the traditional method failed to do so.

3.2.5 Conclusion

In summary, in this section, we presented a novel approach to extract and identify the upwelling region along the Atlantic coast of Morocco from SST and CHL-a images. This approach is based on the use of the U-Net architecture, which is widely used for image segmentation. We validate objectively the proposed methodology by computing the V_{up} index over the years between 2020 and 2021. The result of the quantitative validation demonstrates the outstanding performance and superiority of our proposed methodology over the classical method developed by [El Aouni et al. [2020]]. The results of the segmentation developed in this study will serve as a basic framework for establishing two new upwelling indices. These indices will be presented in the next Chapter to analyze the performance of each satellite observation, to enable further recommendations for improved monitoring and tracking of upwelling in North-West Africa (NWA). Notably, while our methodology excels in various aspects of upwelling region detection, it does encounter limitations in discerning the smallest upwelling areas. To address this constraint, the subsequent section introduces another deep learning framework designed to overcome this challenge.

3.3 Upwelling extraction based on Deep Residual U-Net from SST and CHL-*a* images

In this section, we introduce a novel and straightforward method for the identification and segmentation of upwelling zones in North West (NW) Africa using SST and CHL-*a* images [Belmajdoub and Minaoui]. This method not only effectively addresses the challenge of upwelling detection in the northern region of the Moroccan Atlantic coast but also can detect even the smallest upwelling areas.

3.3.1 Dataset

The dataset comprises a total of 909 SST images and an equivalent number of 909 CHL-*a* images. These images cover 20 years, from 2000 to 2019. The images and their associated segmentation masks are used as inputs for our network architecture. An illustrative visualization of the primary products used in this study is shown in Figure 3.1.

3.3.2 Architecture

The proposed model, DeepRes-UpwellNet, is an advanced end-to-end fully convolutional neural network designed to detect upwelling regions in sea SST and CHL-*a* satellite images. The architecture is built upon the U-Net structure [Sivagami et al. [2020b]] but with substantial improvements to handle deeper and more complex networks.

The DeepRes-UpwellNet comprises two primary pathways: an encoder path responsible for extracting upwelling features from the input SST/CHL-*a* images, and a decoder path that reconstructs these extracted features to match the original input SST/CHL-*a* map size.

Deep networks with multiple stacked layers can improve discrimination capabilities, but they often suffer from vanishing gradients, affecting convergence. To address the problem of gradient degradation during training, the core of the model employs residual units, as illustrated in Figure 3.4(b). These residual units allow direct gradient propagation during backpropagation and enhance accuracy and convergence [Yu et al. [2016]].

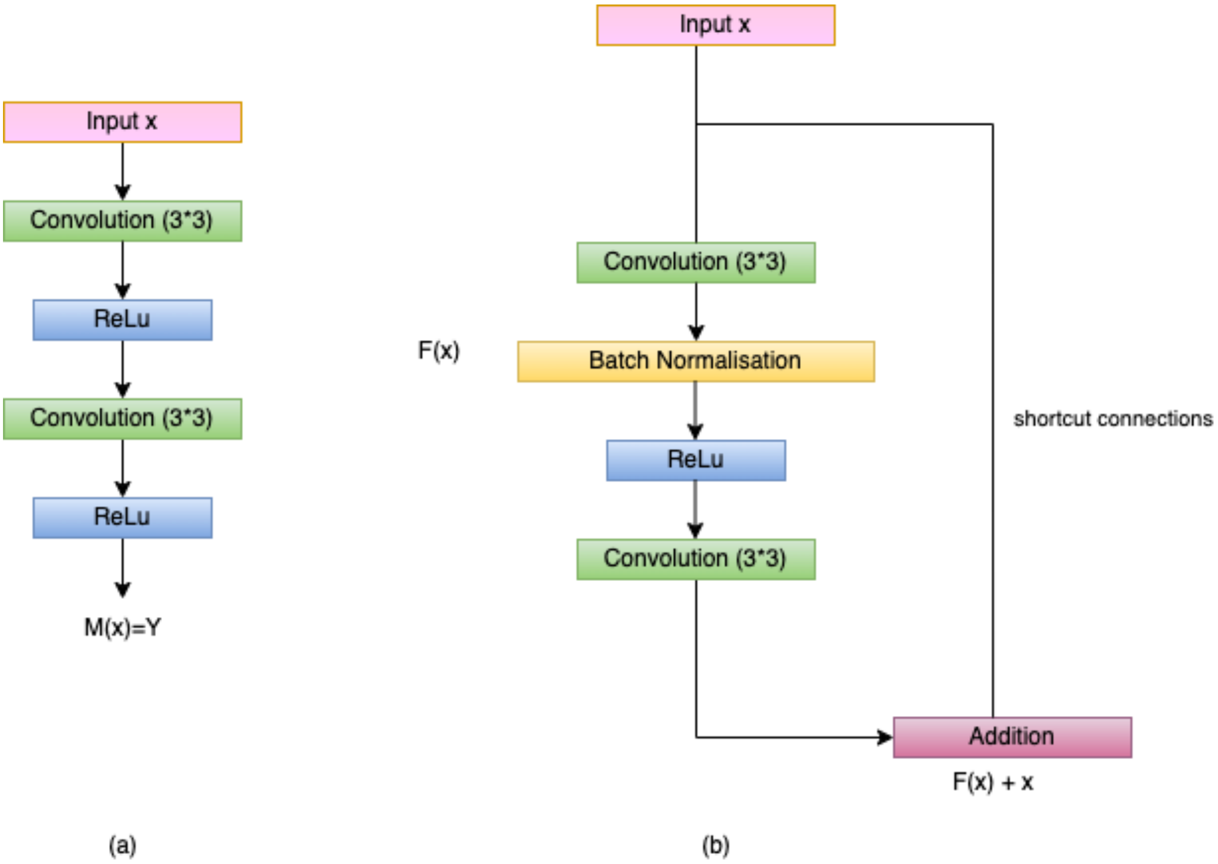

Figure 3.4: Comparing Neural Network Building Blocks: (a): Original Plain Block in the Classic U-Net Architecture. (b): Residual Unit with Identity Mapping in the Proposed Network.

Furthermore, a Softmax layer is integrated at the end of the network to generate the final binary segmentation map. Figure 3.5 provides a comprehensive representation of the detailed architecture of DeepRes-UpwellNet.

The input layer of DeepRes-UpwellNet receives an SST/CHL-a satellite images, containing temperature data in Celsius or chlorophyll-concentration in mgm^{-3}), while the output layer produces a binary segmentation map. In the segmentation map, white pixels indicate upwelling regions, while black pixels represent non-upwelling regions, including cloud and land pixels.

The design of DeepRes-UpwellNet follows a symmetric structure similar to U-Net, but with deeper layers and a key distinction: it employs residual network units instead of simple convolutional units. Each residual unit consists of a 3×3 convolutional layer, followed by batch normalization [Ioffe and Szegedy [2015]] and a ReLU activation function [Harrison et al. [2021]], which helps in capturing non-linear features effectively. The use of residual units ensures the efficient flow of information through the network and mitigates the vanishing gradient problem (Figure 3.4(b)).

Mathematically, the residual unit can be represented as follows:

let's consider a neural network block as shown in Figure 3.4(a), with input denoted as 'x' and the true underlying distribution as '$M(x)$'. The network learns the mapping from input 'x' to output 'y' which can be represented as follows:

$$M(x) = Y \tag{3.2}$$

The residual function captures the difference between the mapping applied to 'x' (i.e., '$M(x)$') and the original input 'x' instead of directly learning a direct mapping. This can be expressed as:

$$F(x) = M(x) - x \tag{3.3}$$

The concept of shortcut connections is integral to this approach. The shortcut connections are represented by:

$$M(x) = F(x) + x \tag{3.4}$$

In this architecture, feature extraction from input SST/CHL-a images is accomplished using convolutional layers. To enhance the training process, batch normalization is implemented after each convolutional layer. The convolution operations use a 3×3 filter with a stride of one, generating convolved feature maps.

To downsample the feature maps obtained from the residual units in the encoder path, a 2×2 max pooling operation is employed. This downsampling reduces feature map size, resulting in lower computational complexity while maintaining input transformation invariance.

For the decoder path, transposed convolutions are used to restore the original resolution of the feature maps. The final layer of the network consists of a 1×1 convolutional layer, followed by a Softmax activation to convert the multi-channel feature maps into the ultimate binary segmentation map. This segmentation map labels pixels as '1' and '0' for upwelling and background regions, respectively.

DeepRes-UpwellNet model represents a significant advancement in upwelling region detection from SST/CHL-a satellite images, using a combination of residual units and symmetric U-Net architecture, providing more accurate and reliable results compared to traditional methods.

3.3.3 Training the Model

The segmentation model employed for the extraction and identification of upwelling regions in SST and CHL-a images was developed using Python, TensorFlow, and Keras. Keras, serving as a high-level neural network API, operates seamlessly on top of TensorFlow. Leveraging Keras facilitates rapid experimentation without the need for extensive code development.

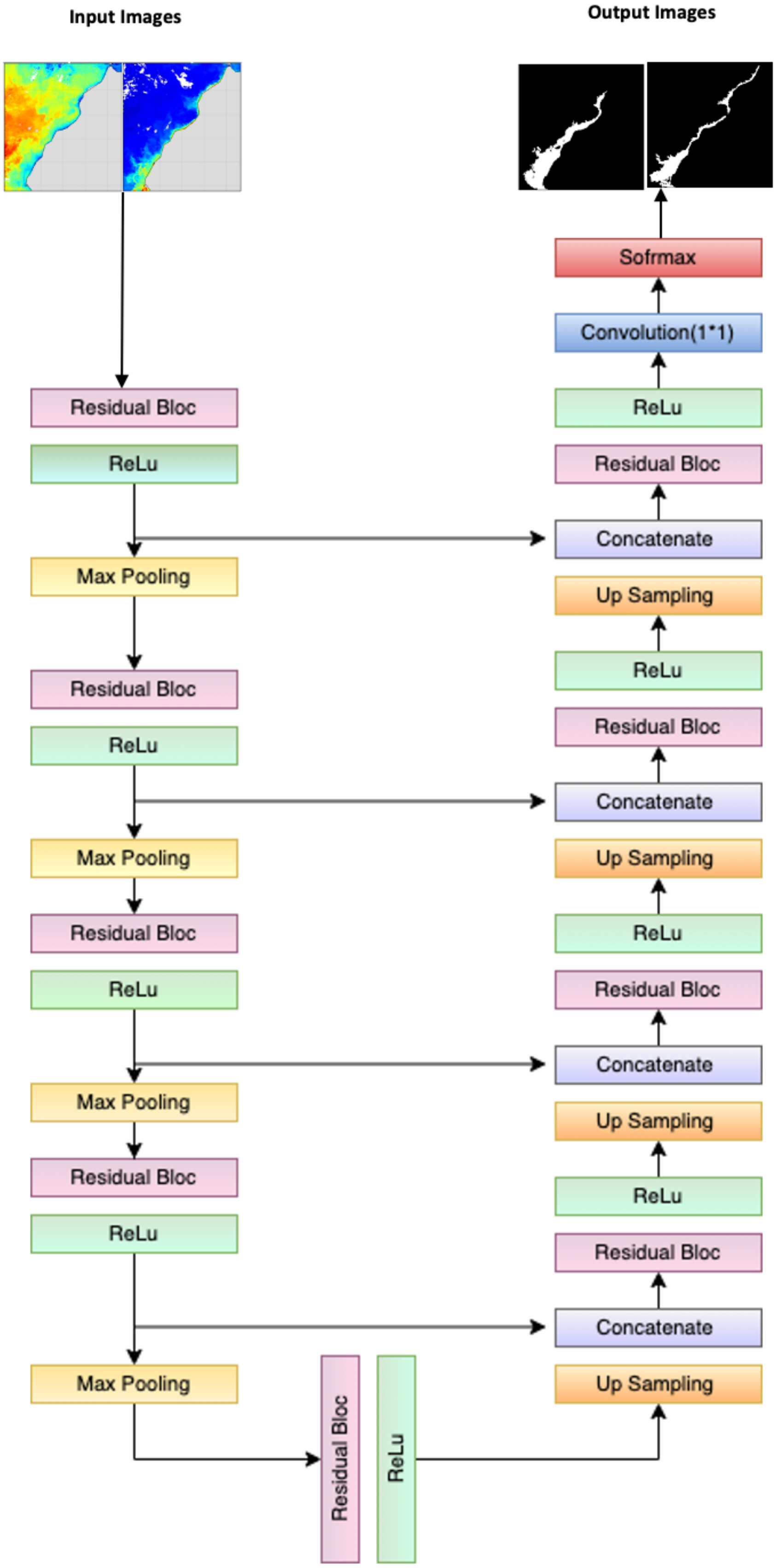

Figure 3.5: DeepRes-UpwellNet Architecture: Binary Segmentation from SST/CHL-a Images. The input layer contains temperature values in (°C) or chlorophyll-concentration in (mgm^{-3}). The left part depicts the Encoder Path, while the right part represents the Decoder Path.

The training dataset utilized in this study comprises original SST and CHL-*a* images alongside manually segmented mask images. Specifically, tThe dataset comprises 1818 sets of unmasked SST/CHL-*a* images along with their corresponding masks.which were partitioned into training and validation subsets. The training subset encompassed (75%) of the images, while the remaining (25%) were reserved for validation purposes. We use the ADAM optimization function, with an initial learning rate of 0.0001, and 500 epochs.

3.3.4 Results and Discussion

In this section, we describe the results obtained from our experiments. To evaluate the effectiveness of our method, we have chosen to compare it with the method developed by [El Aouni et al. [2020]] and the method developed in the previous section.

The results obtained from visual inspection indicate that the DeepRes-UpwellNet surpasses the other two methods in performance. Figure 3.6 demonstrates the accurate extraction of the primary upwelling area along the Moroccan Atlantic coast by the DeepRes-UpwellNet. Both the CNN-Unet and DeepRes-UpwellNet models exhibit superior effectiveness compared to the traditional method in detecting upwelling in both SST and CHL-*a* images. Notably, these models successfully detected upwelling in the northern region, particularly in the case of SST images, where the conventional method failed to do so.

Furthermore, upon visual examination, it is evident that the DeepRes-UpwellNet model outperforms the CNN-Unet framework. The DeepRes-UpwellNet successfully identifies even the smallest areas of upwelling (indicated by the red circle in Figure 3.6) that are not detectable by the CNN-Unet.

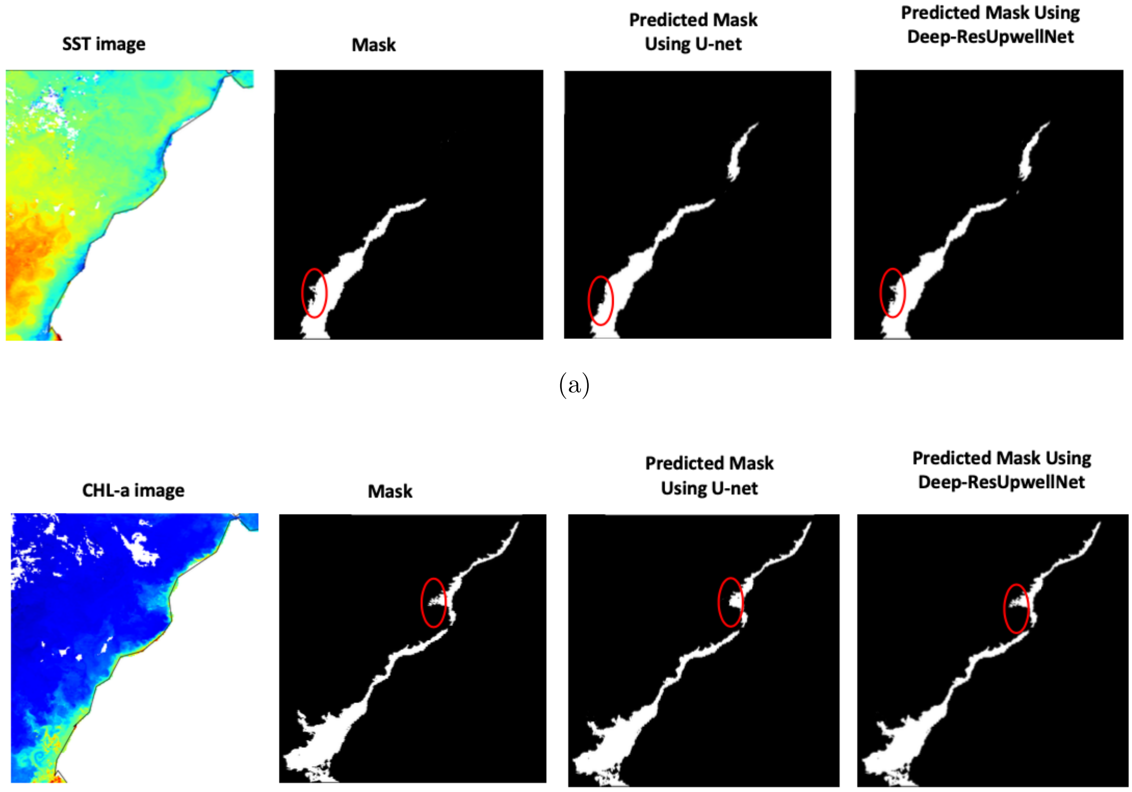

(a)

(b)

Figure 3.6: Comparative visualization of upwelling segmentation results using three approaches to (a) SST and (b) CHL-a image.

To quantitatively validate our proposed method, we calculate the V_{up} index on 92 SST images and 92 CHL-a images captured in two consecutive years (2020-2021). The results obtained for V_{up} are presented in Table 3.2 and are compared with the results obtained in the previous section (see Table 3.1).

The obtained index validates the effectiveness of our approach in accurately delineating the main Moroccan upwelling fronts. Specifically, for CHL-a and SST, our method demonstrates a significant improvement of over 1.5% in V_{up} compared to the approach developed in the previous section. This improvement showcases the superior upwelling detection capabilities of the DeepRes-UpwellNet, as it successfully identifies more upwelling regions compared to the conventional U-Net

	time	V_{up}
DeepRes-UpwellNet	3s	SST= 79.18%; CHL-a= 79.34%
CNN-Unet	3s	SST= 78.30%; CHL-a= 78.97%
Methodology of El Aouni et al. [2020]	1min9s	SST= 76.74%; CHL-a= 77.88%

Table 3.2: Results of V_{up} on the proposed methodology on SST and CHL-a images from 2020 to 2021.

method.

3.3.4.1 Evaluation Metrics

To ensure a robust ans comprehensive assessment of our model, DeepRes-UpwellNet, we employ a variety of evaluation metrics. We utilized three standard metrics, namely overall accuracy, F1-score, and Intersection over Union (IoU).

Accuracy is a measure of the overall correctness of the model. It is calculated as the ratio of the number of correct predictions to the total number of predictions made. The formula for accuracy is given by:

$$Accuracy = \frac{\text{TP} + \text{TN}}{\text{Total Predictions}} \tag{3.5}$$

Where: TP = True Positives; and TN = True Negatives

F1-Score is particularly useful when dealing with imbalanced datasets. It is a composite metric that combines Precision and Recall into a single value. The F1-score is defined as the harmonic mean of Precision and Recall and calculated as follows:

$$F1Score = \frac{2 \cdot (\text{Precision} \cdot \text{Recall})}{\text{Precision} + \text{Recall}} \tag{3.6}$$

where: $\text{Precision} = \text{TP}/\text{TP} + \text{FP}$ and $Recall = \text{TP}/\text{TP} + \text{FN}$; FP = False Positives; FN = False Negatives.

IoU is a primary measure of segmentation efficiency. It quantifies the degree of overlap between predicted segments and ground truth. predicted segments and ground truth segments. The formula is as follows:

$$IoU = \frac{TP}{TP + FP + FN} \tag{3.7}$$

In our comparative analysis, we evaluated our proposed DeepRes-UpwellNet,. We compared it against a CNN-Unet model. The quantitative results are presented in Table 3.3 , revealing that DeepRes-UpwellNet outperformed across all performance metrics. Notably, our model achieved an overall accuracy of 99.10%, an IoU of 85.66%, and an F1-score of 90.75%.

A more in-depth examination of Table 3.3 demonstrates that DeepRes-UpwellNet significantly outperforms the baseline architecture,CNN-Unet, in terms of accuracy, IoU, and F1-Score. These finding results highlight the superior performance of our model, which can be attributed to the use of skipped connections. These skipped connections facilitate feature extraction, improved gradient flow and superior generalization capabilities.

Method	Accuracy (%)	IoU (%)	F1-Score (%)
DeepRes-UpwellNet	99.10%	85.66%	90.75%
CNN-Unet	97.80%	81.23%	86.12%

Table 3.3: Performance models.

3.4 Conclusion

In conclusion, this chapter presented and developed a series of deep learning methodologies aimed at advancing the monitoring and refinement of upwelling region identification using physical and biological satellite data. The first contribution presented a new approach based on the U-Net architecture, which extracted and identified upwelling regions along the Moroccan Atlantic coast from SST and CHL-a satellite images. This approach demonstrated an exceptional ability not only to detect upwelling regions, but also to locate them accurately within predefined geographical areas. Building on this, the second contribution introduced DeepRes-UpwellNet, a specialized deep learning tool designed to accurately detect and locate upwelling regions in SST and CHL-a images along the Moroccan Atlantic coast. DeepRes-UpwellNet demonstrated superior performance to traditional segmentation methods and U-Net architecture. Its ability to identify even the smallest areas of upwelling further enhanced its effectiveness as a tool for objective analysis of this oceanic phenomenon. The third contribution broadened the scope of application by presenting the DeepCoast$_{up}$-Net, a deep learning approach designed to extract and accurately identify upwelling regions using SST satellite imagery. The method relies on an integration of three key information channels - sea surface temperature, distance from shore, and latitudinal position - to comprehensively capture the complex interactions governing upwelling dynamics. Thanks to the U-Net architecture-based training process, DeepCoast$_{up}$-Net has demonstrated its ability to recognize and characterize upwelling patterns, making it a tool for studying upwelling phenomena in various coastal zones. Collectively, these contributions mark significant advances in the detection and analysis of upwelling regions, offering improved methodologies for detecting, characterizing and understanding the dynamics of upwelling regions. While each method has demonstrated remarkable capabilities, it is essential to recognize their limitations, including the challenges of detecting even the smallest upwelling regions. The search for accurate segmentation in various coastal contexts remains an ongoing undertaking. These proposed methods not only enhance understanding of upwelling phenomena but also improve the monitoring and tracking of upwelling events along the Moroccan Atlantic coast and beyond. The next chapter will focus on the presentation of new upwelling indices, to quantify and analyze the spatio-temporal dynamics of upwelling in NWA.

Chapter

4

NEW INDICES BASED ON BIOLOGICAL AND PHYSICAL SATELLITE OBSERVATIONS FOR UPWELLING DYNAMICS.

4.1 Introduction

This chapter undertakes a comprehensive study of upwelling activity along the Moroccan Atlantic coast. It begins with a thorough review of established indices widespread in the literature, designed to quantitatively analyze seasonal and interannual fluctuations in upwelling dynamics. Subsequently, building on the upwelling extraction method presented in Chapter 3, a new upwelling index is formulated, based on SST images [Belmajdoub et al. [2023b]]. This index aims to provide a more detailed understanding of upwelling dynamics in this region. In addition, based on this proposed new index, a comprehensive study is underway to examine spatio-temporal variations in upwelling dynamics in Morocco. Finally, based on the same upwelling extraction method, we are developing two additional indices using both SST and CHL-textita images [Belmajdoub et al. [2023a]]. A full comparative study based on these indices will be presented.

4.2 Review of Existing Indices

Understanding the spatial and temporal variability of the upwelling phenomenon is of utmost significance for comprehending the marine ecosystem's productivity and its influence on fluctuations in fisheries resources. The dynamics of upwelling play a pivotal role in shaping the spatial and temporal evolution of these resources, making it a crucial aspect to study.

However, monitoring the temporal evolution of upwelling through satellite measurements poses challenges, as it necessitates the systematic analysis of daily or even weekly images. To facilitate operational and efficient monitoring, various methods, ranging from simple to complex, have been developed to synthesize the upwelling locations along the coast for specific time periods. These methods aim to streamline the process and enhance the effectiveness of upwelling monitoring, which is vital for studying its impact on marine environments and associated resources.

Upwelling detection methods primarily rely on thermal differences between coastal and offshore waters. Normally, the temperature distribution along the longitude direction remains relatively consistent in both areas. However, the presence of coastal upwelling disrupts this homogenization, resulting in noticeable thermal contrasts between cooler coastal waters and warmer offshore waters. This causes the isotherms to take distinct meridional patterns, roughly parallel to the coastline. Consequently, the negative thermal difference between inshore and offshore waters serves as a reliable indicator not only for detecting upwelling at different latitudes but also for gauging its intensity and strength.

Building upon this understanding, several methods have been developed to calculate upwelling indices, formulated into practical applications that synthesize data over specific time periods. These approaches offer valuable information about the occurrence and characteristics of upwelling events. Noteworthy studies in this field include works by [Van Camp et al. [1991]], [NYKJAER and VANCAMP [1992]], [Nykjær and Van Camp [1994]], and [Demarcq and Faure [2000]] .

4.2.1 Ekman transport index (I_E)

The Cross-shore Ekman transport (CSET) is a fundamental calculation used to estimate the theoretical water flux transported offshore by wind stress, which is obtained from satellite data and acts on the coastal upward flow of colder water. This concept was originally introduced by Ekman in 1905. The calculation of the offshore Ekman transport per unit length (represented as ν, in the x direction) is based on the assumption of alongshore balance between the Coriolis force and alongshore wind stress.

The expression for the Cross-shore Ekman transport (ν) is given by:

$$\nu = \frac{\tau_y}{\rho f} \tag{4.1}$$

where: τ_y represents the alongshore surface wind stress (in the y direction) measured in Pascal units, f denotes the Coriolis parameter in Newton units, and ρ indicates the surface water density measured in (g/cm^3).

This index serves as an indicator of the volume of upwelled flow and is typically presented in units of $(m^2.s^{-1})$. The magnitude of the Cross-shore Ekman transport depends on latitude and wind stress, both of which significantly influence the coastal dynamics and the intensity of upwelling.

To calculate the drag coefficient of the wind on the sea surface, a nonlinear formula proposed by [Trenberth et al. [1990]] is employed. This coefficient plays a role in understanding the impact of wind on the upwelling process and contributes to a comprehensive analysis of marine ecosystems and coastal environments.

4.2.2 SST based upwelling index

Several studies, such as those conducted by [Wooster et al. [1976]], [Nykjær and Van Camp [1994]], have defined SST-based upwelling indices as a straightforward thermal difference between the maximum SST value (representing warm offshore waters) denoted as SST_{max}, and the minimum SST value (representing the upwelling waters) denoted as SST_{min}, encountered along the same Latitude. The purpose of these indices is to quantify the presence of upwelling and provide estimates of its intensity and strength. This thermal index is practically computed using two different data sources: satellite data (Mittelstaedt [1991]; Lathuiliere et al. [2008]; Marcello et al. [2011] and Santos et al. [2011]) and in-situ measurements (Speth [1982]; Speth and Köhne [1983]; and Van Camp et al. [1991]).

The computation of the thermal index follows the formula:

$$CUI_{SST} = SST_{max} - SST_{min} \tag{4.2}$$

The results obtained from this thermal index show significant correlation with those obtained through the Cross-Shore Ekman Transport method.

A different approach to measuring coastal upwelling, known as the normalized coastal upwelling index, was developed by Demarcq and Faure [2000]. The index is calculated using the following formula:

$$CUI_{SST} = \frac{SST_{max} - SST_{min}}{SST_{max} - SST_{up}} \tag{4.3}$$

However, this index encounters challenges when applied to the latitudinally varying patterns of the West African region, where different water masses, such as South and North Atlantic Central Waters, are present. The lack of a precise measure for SST_{up}, which represents the original temperature of the upwelled water before reaching the sea surface, makes normalization problematic for the Moroccan region and introduces a seasonal bias.

A more accurate and robust method for calculating the upwelling index has been proposed in [Benazzouz et al. [2014]]. This method stands out due to its comprehensive statistical study, analyzing a 30-year historical dataset of SST data.

4.3 Data and Area for Interest

Our study focuses on investigating upwelling fluctuations along the Moroccan Atlantic coast, which spans from ($21°N$ to $36°N$ and $6°W$ to $19°W$). This region experiences diverse and significant upwelling activity throughout the year Tamim et al. [2014d]. Fig 4.1 illustrates this coastal area, along with a climatological image of SST obtained from the Group for High-Resolution Sea Surface Temperature (GHRSST) multi-product satellite-based ensemble (GMPE) dataset, which is accessible through the climate data store website `https://cds.climate.copernicus.eu/`. Each satellite image represents a $315 * 315$ pixel map with a spatial resolution of 4×4 kilometers. Our extensive database includes 1778 eight-day SST images, covering the time period from 1982 to 2021. Additionally, we obtained daily wind data from 1987 to 2021, with $1/4°$ resolution, utilizing the QuikSCAT and ASCAT wind estimates. This wind data is essential for computing the cross-shore Ekman Transport Index.

4.4 New SST based Upwelling Index

In the field of characterizing and discerning spatial and temporal patterns of upwelling, upwelling indices have been widely applied. In this section, we present a novel and intuitive approach to establishing a latitudinal upwelling index Belmajdoub et al. [2023b]. Our method builds on the segmentation framework presented in the previous chapter, and opens the way to a new perspective on upwelling evaluation.

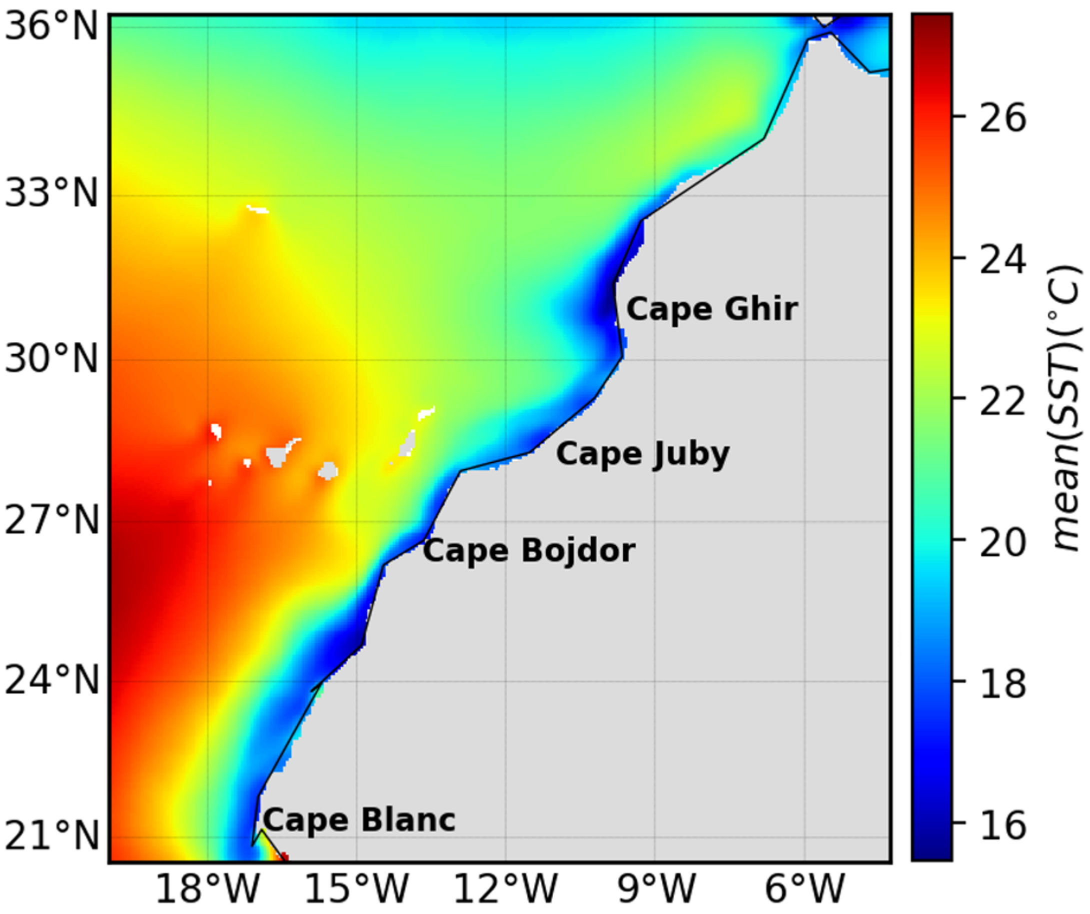

Figure 4.1: Climatological means of SST images over the Moroccan coast. Each pixel of the infrared image contains temperature information expressed in Celsius degrees(°C) Between ([1982 – 2021]).

4.4.1 Radials configuration

As coastal upwelling is mainly influenced by the width of the continental shelf [Atillah et al. [2005]], an effective method is used to cover the entire width of the Moroccan coastal shelf. This approach consists of tracing radials perpendicular to the general direction of the shelf. The methodology for drawing these radials involves establishing a virtual line, visually represented by a black line in Figure 4.2, parallel to the coastline. Subsequently,, the radials, represented by red lines in Figure 4.2, are positioned perpendicular to the virtual line, aligned with the general direction of the coastline. This orientation was chosen to ensure complete coverage of the width of the continental shelf.

Consequently, upwelling indices are computed along the radials, consistently aligned in a fixed direction relative to the coast.

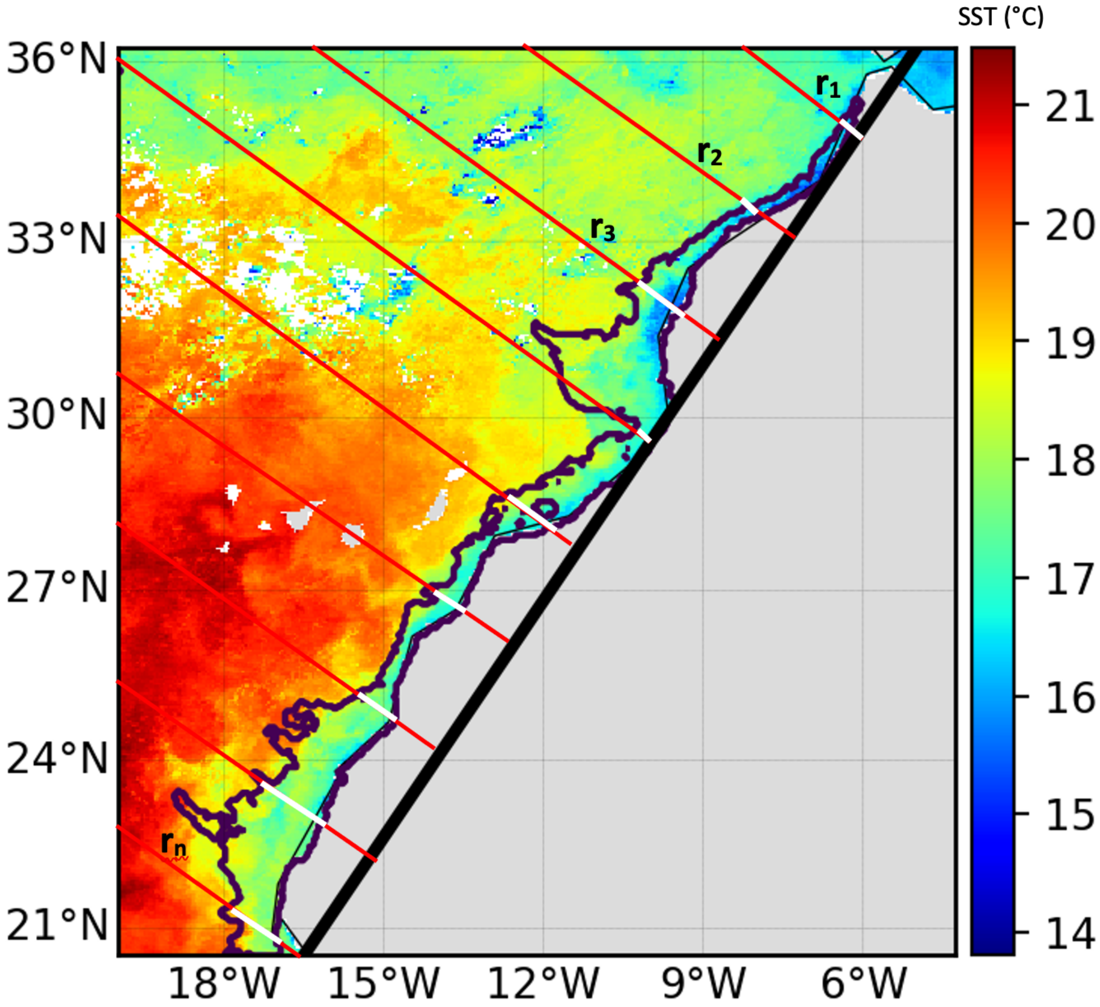

Figure 4.2: Example the configuration used to compute the upwelling index.

4.4.2 New Upwelling Index calculation

Various studies have commonly employed a straightforward concept to delineate such indices by calculating the thermal contrast between coastal and offshore temperatures at identical latitudes [Demarcq and Faure [2000]], [Van Camp et al. [1991]]. Notably, Benazzouz et al. [2014] and [[El Aouni et al., 2019]] demonstrated the suitability of this type of index for assessing the Moroccan upwelling phenomenon.

The calculation of the novel upwelling index involves determining the thermal difference between the highest recorded temperature within the upwelling area and the colder upwelling water present along the same radial direction within the extracted upwelling region. This index is represented by the equation:

$$I^{r}_{sst_{up}} = SST^{up}_{max} - SST^{up}_{min} \tag{4.4}$$

it is important to note that we consider latitudes as radials (r), which are perpendicular to the coastline. The next step is to provide definitions for two key parameters, SST^{up}_{max} and SST^{up}_{min}.

4.4.3 SST^{up}_{min} and SST^{up}_{max} identification

The commonly adopted methodology involves defining SST_{min} as the minimum temperature occurring between the coast and the continental slope, while SST_{max} corresponds to the offshore temperature. Notably, different studies have made distinct choices regarding the specific locations for SST_{min} and SST_{max}.

For instance, in the work by [Nykjær and Van Camp [1994]], SST_{min} was determined between the coast and the 200 m depth contour, with SST_{max} set at 500 km from the coast. In contrast, [Santos et al. [2005]] selected SST_{min} within a range of 20 km to 40 km from the coastal area, while SST_{max} was identified between 400 to 1000 km offshore. Another study conducted by [Benazzouz et al. [2014]] involved a statistical analysis of a 30-year SST database to find SST_{min}, which was then averaged with the eight surrounding pixels to reduce local noise. For SST_{max}, they extracted it up to 3000 km offshore. Furthermore, [El Aouni et al. [2019]] defined SST_{min} as the minimum temperature within the extracted upwelling zone, and SST_{max} was identified similarly to the approach in [Benazzouz et al. [2014]], representing the maximum temperature outside the upwelling zone up to 3000 km offshore.

In our study, we propose a novel approach to determine SST_{max} and SST_{min}. Unlike previous fixed-band methods that only consider SST_{min} near the coast, our new upwelling index selects SST_{min} as the minimum temperature within the upwelling zone, ensuring a more comprehensive calculation that accounts for all essential low temperatures. Additionally, we define SST_{max} as the maximum temperature within the upwelling zone, eliminating any arbitrary positional choices and focusing solely on the upwelling region. Consequently, SST_{min}^{up} and SST_{max}^{up} respectively represent the highest and lowest coastal temperatures within the upwelling zone.

Starting from North to south (Fig 4.2), each segmented upwelling region $S_{up} \epsilon \{1.....length(data)\}$ includes radials, and each radial $r \epsilon \{1.....n\}$ contains temperature values $r = \{T_i^r ; i = 1.....n\}$. Therefore, over each radial, the SST_{min}^{up} and SST_{max}^{up} are defined as:

$$SST_{max}^{up} = \max_{S_{up}}(T_i^r) \tag{4.5}$$

$$SST_{min}^{up} = \min_{S_{up}}(T_i^r) \tag{4.6}$$

The Figure 4.2 Shows an example where we look for SST_{max}^{up} and SST_{min}^{up} (white color).

4.4.4 The Advantages of our New Upwelling Index

As stated earlier, the upwelling index introduced in [Benazzouz et al. [2014]] and [El Aouni et al. [2019]] are regarded as the most accurate method available thus far. However, we now highlight the distinct advantages of our novel upwelling index in comparison to the one proposed in [Benazzouz et al. [2014]] and in [El Aouni et al. [2019]]:

Simplicity and Computational Efficiency: Our index offers a simple and intuitive approach compared to Benazzouz et al. [2014], significantly improving computational efficiency.

Comprehensive Temperature Consideration: Unlike the fixed-band approach of [Benazzouz et al. [2014]], which might overlook certain low temperatures in the estimation, our index ensures the inclusion of all necessary low temperatures in the calculation.

Dynamic Nature: the index in [Benazzouz et al. [2014]] is static and tailored for historical studies within specific periods, our index is dynamic and can be applied to historical data at any point in time as well as new data at any temporal resolution, including single acquisitions. This enables easy and efficient upwelling analysis without the need for repeated complicated statistical analysis.

Precision and Reliability: The new index ensures that the highest temperature within the upwelling zone is precisely captured, providing a more comprehensive understanding of the thermal characteristics in this critical area. By avoiding arbitrary selection of SST_{max} from various locations, our index achieves greater consistency and reliability in assessing upwelling events, setting our method apart from [Benazzouz et al. [2014]] and [Benazzouz et al. [2014]].

Focused Scope: one of the most significant advantages of our approach is its limitation solely to the upwelling region. This focused scope allowed us to improve the quantification and analysis of the seasonal and interannual variability of the upwelling dynamics. By concentrating on the specific area of interest, our index can better discern subtle temperature variations and capture essential patterns in upwelling behavior, leading to more accurate and insightful results.

To assess the effectiveness of our index, we will conduct an interannual analysis of the Moroccan upwelling. The obtained results will be compared with those obtained by [El Aouni et al. [2019]] and the Ekman transport index. This comparative study aims to showcase the strengths and advantages of our novel upwelling index in accurately assessing the dynamics of the Moroccan upwelling system.

4.4.5 Comparative Assessment of Seasonal and Interannual Upwelling Intensity

Employing the newly proposed upwelling index, we present a comprehensive analysis of the seasonal and interannual variability of the Moroccan upwelling. The Hovmoller-diagrams are constructed at a spatio-temporal resolution of 4km/8-day, derived from SST data spanning the latitude range of $21°N$ to $36°N$ over the period from 1982 to 2021 (refer to Figure 4.3). To gain insights into its performance, the spatio-temporal variability of our new upwelling index ($I^r_{sst_{up}}$) (Figure 4.3(a)) is compared with the cross-shore Ekman transport index (I_E) and the upwelling index (I_r) developped in [El Aouni et al. [2019]] calculated over the same period (see Figure 4.3(b) and Figure 4.3(c)).

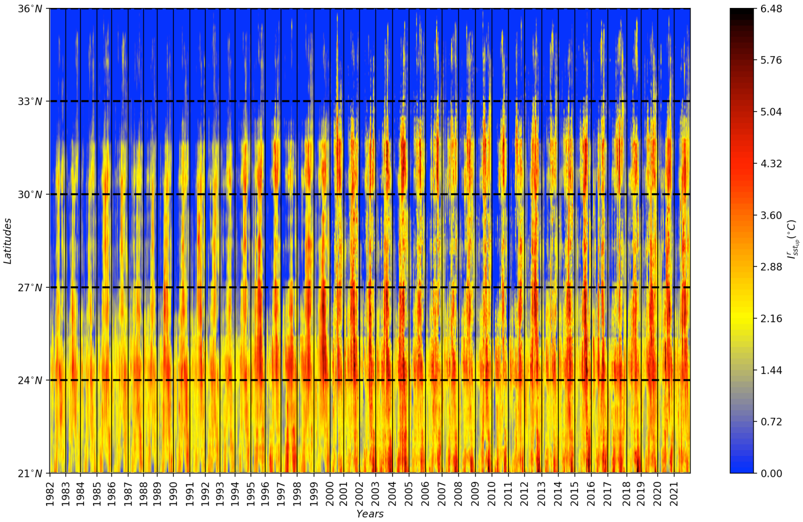

(a)

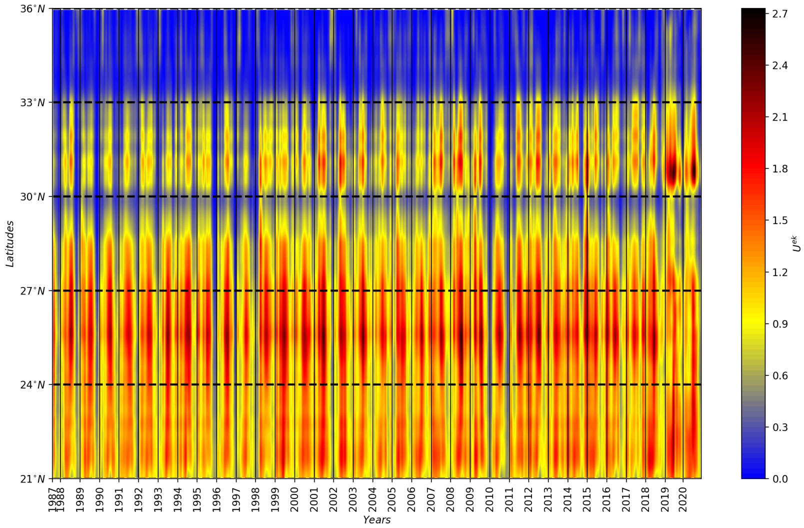

(b)

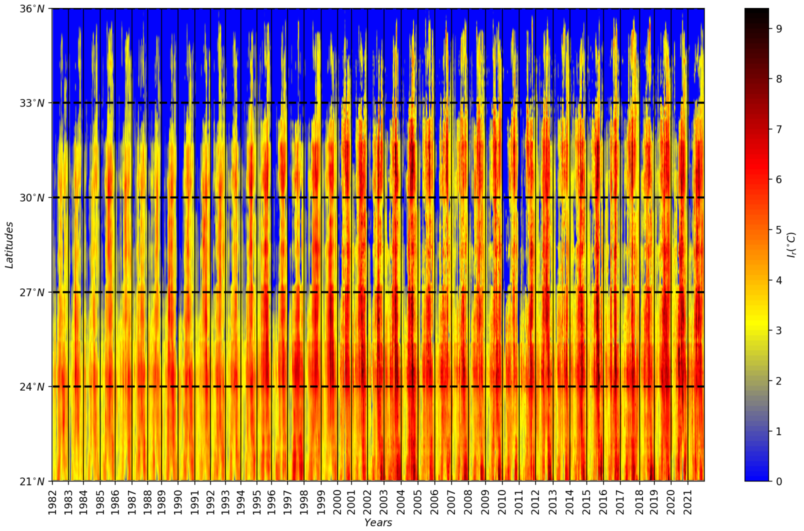

(c)

Figure 4.3: Space-time Hovmoller diagram: (a): new Upwelling index ($I^r_{sst_{up}}$), (b): Cross-Shore Ekman Transport (I_E), (c): Upwelling index (I^r) developed by El Aouni et al. [2019] , over the period between $1982 - 2021$.

The new SST upwelling index varies from 0 degrees to 6.5 degrees. The primary upwelling patterns derived from physical and biological observation are largely the same, and they are very similar to the cross-shore Ekman transport (see Figure 4.3(b)). This agreement with the wind-based upwelling index confirms our novel upwelling index and enables further analysis of sub-mesoscale oscillations that the new upwelling index does record but are not caught by the wind.

The northern region, bounded by $(33^{circ}N, 36^{circ}N)$, exhibits the lowest coastal temperatures throughout the 40-year time span, as opposed to what is depicted in (fig. 4.3(c)). These low values are due to the weaker winds and unfavorable coastline orientation in this region (winds are not parallel to the coastline) [El Aouni et al. [2019]] (figure 4.3(a)) and (fig 4.3(b)).

Moving to the central area between latitudes $(27°N, 33°N)$, the presence of a giant filament around Cape Ghir significantly influences the upwelling index in this zone. While (figure 4.3(c)) suggests a lack of upwelling during winter, our new index (figure 4.3(a)) reveals distinct patterns. It indicates the absence of upwelling during winter, and there are also intermittent periods in spring and summer when no upwelling is observed. Notable periods where upwelling is absent are 1989-1997, 2005, 2010-2011, as well as 2013 and 2017.

Globally, the $I^r_{sst_{up}}$ in the central area experiences significant upwelling year-round, with the most intense values (ranging from 3°C to 5°C) observed at latitudes $28°N$, $29°N$, $31°N$, and $32°N$, where considerable upwelling filaments occur [Nieto et al. [2012]]. Analyzing the interannual and seasonal fluctuations of upwelling intensity (fig.4.3(b)) through the I_E index, we find a strong relationship between the patterns of $I^r_{sst_{up}}$ and I_E. Specifically, between April and November of most years, the primary wind pattern that favors upwelling in the central zone is primarily between latitudes $28°N$ and $31°N$.

In the southern part between latitudes $(21°N, 27°N)$, the interannual and seasonal thermal variability indicates consistently strong upwelling according to (figure 4.3(c)). However, our analysis using the new index (figure 4.3(a)) reveals that while upwelling is generally stronger in this region, its intensity and consistency vary across seasons. Specifically, upwelling activity remains strong and continuous between latitudes $24°N$ and $26°N$ throughout the year, with peak values of $I^r_{sst_{up}}$, particularly from summer to autumn (figure 4.3(a)). On the contrary, upwelling is absent or reduced during all winters. The intensity of $I^r_{sst_{up}}$ is highest from spring to autumn, with temperatures ranging from 3 to 6 degrees Celsius in the southern region, largely due to the strong trade winds near the shore (figure 4.3(b)). Notably, several intriguing discontinuities in upwelling were observed, especially near latitude $27°N$, with its presence not consistent every year from June to September (figure 4.3(a)). The decrease in the new upwelling index during the years 1990-1996 and 2010-2011 can be attributed to extremely negative values of the North Atlantic Oscillation. Overall, the $I^r_{sst_{up}}$ and I_E models show remarkable similarity, confirming the efficacy of assessing upwelling intensity based on the radial thermal difference between coastal minimum and maximum temperatures.

Through a comparison between our newly developed upwelling index, $I^r_{sst_{up}}$ (figure 4.3(a)), and the one presented in [El Aouni et al. [2019]] (figure 4.3(c)), as well as the cross-shore Ekman transport index, I_E (figure 4.3(b)), we have observed that our index offers a more accurate depiction of upwelling dynamics. On a larger scale, $I^r_{sst_{up}}$ aligns more closely with I_E than with I_r. Furthermore, both $I^r_{sst_{up}}$ and I_E exhibit similar seasonal patterns of high and low values in the three regions under analysis. However, on a smaller scale, I_r shows consistently high intensity throughout the year in the southern region between latitudes $21°N$ and $27°N$, while $I^r_{sst_{up}}$ and I_E demonstrate significantly lower intensity during winter and spring. In the central region, between latitudes $27°N$ and $33°N$, I_r exhibits moderate intensity near latitude $30°N$, while $I^r_{sst_{up}}$ and I_E show very low intensity. The most notable difference in intensity is observed in the northern region, between latitudes 33°N and 36°N, where I_r is relatively high despite the near absence of upwelling. Conversely, $I^r_{sst_{up}}$ and I_E demonstrate the expected lack of intensity in this area.

To summarize, our newly developed upwelling index indicates an average upwelling intensity in three distinct zones. Specifically, upwelling intensity decreases from the southern to the northern region, with temperatures ranging from approximately 3°C to 6.5°C in the south, 2°C to 4.5°C in the central zone, and below 1°C in the northern zone throughout the year. Additionally, the seasonal variability follows a noticeable pattern: upwelling is minimal or absent during winter and gradually intensifies throughout the year, reaching its peak during the summer season.

4.4.6 Interannual Variability of the Upwelling Dynamics from SST images

In order to investigate upwelling activity more comprehensively, we present our novel upwelling index $I^r_{sst_{up}}$, at three specific sites located at latitudes 24°N, 29°N, and 31°N. Figure 4.4 illustrates the interannual variations in upwelling activity at these three selected sites for the period from 1982 to 2021.

Analysis of the results reveals a consistent trend across all three latitudes, wherein maximum upwelling activity peaks are observed during certain periods. The latitude 24°N, situated in the southern region of Morocco, exhibits higher upwelling activity compared to latitudes 29°N and 31°N in the northern part. Notably, during the summer seasons of 2001 to 2004 and 2015 to 2017, there is a substantial upwelling activity at 24°N, indicated by the maximum upwelling index exceeding 5 degrees (Figure 4.3). Conversely, in the same season, the years 1982 to 1989, 2005, and 2010 show average upwelling activity, while the lowest upwelling index values are recorded in autumn and winter during the years 2000, 2002, 2007, and 2011 (Figure 4.3).

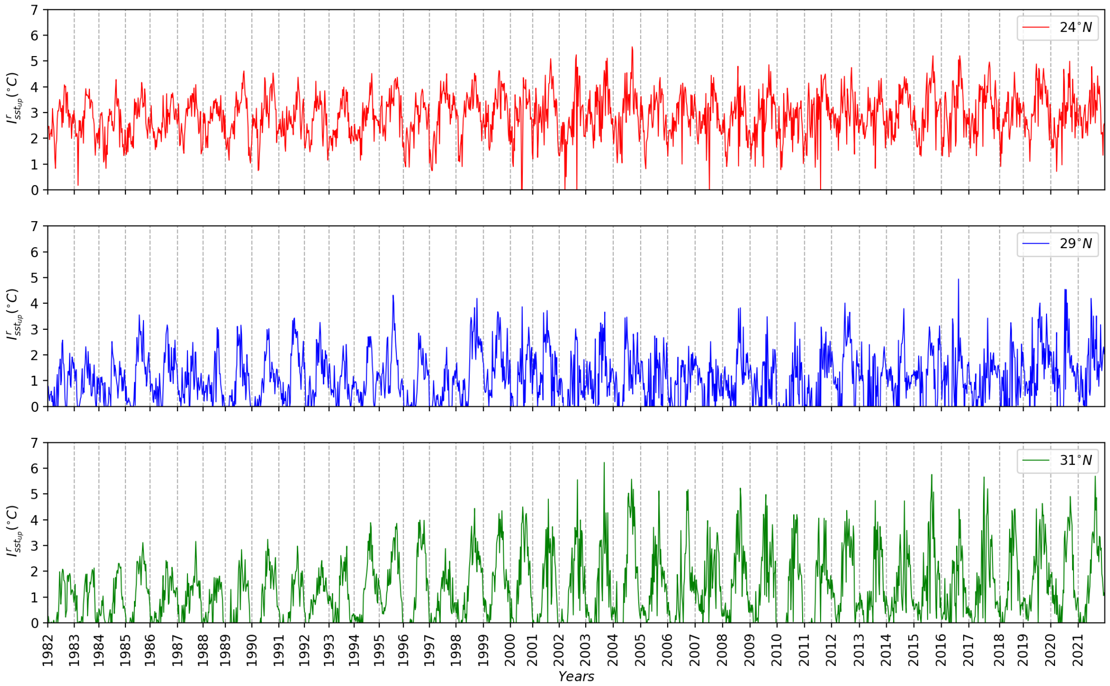

Figure 4.4: New Upwelling Index ($I^r_{sst_{up}}$) at the 3 selected stations over the years 1982-2021: 24°N (red color), 29°N (blue color), and 31°N (green color).

At latitude 29°N, the strongest upwelling activities occur in the summer seasons of 1995, 1998, 2012, 2016, and 2019 to 2021, with the upwelling index reaching its maximum (between 4 and 5 degrees) (Figure 4.4). Conversely, the autumn and winter seasons at this latitude exhibit lower upwelling activity, and the years 1982 to 1985, 1996 to 1998, 2006 to 2007, and 2013 show the lowest minimum upwelling index values (Figure 4.4).

The latitude 31°N displays significant upwelling activities during the summer seasons in the periods 2002 to 2006, 2008 to 2009, 2015, 2017, and 2021, with the upwelling index exceeding 5 degrees (Figure 4.4). Conversely, the winter seasons during the years 1982 to 1985, 1988, and 1992 show low upwelling activity at this latitude (Figure 4.4).

Collectively, the observations from these three stations highlight the strong seasonal dynamics of upwelling activity along Morocco's Atlantic coast. The intensity and occurrence of upwelling events demonstrate significant variations throughout the year. Moreover, there is a distinct north-to-south increase in upwelling activity along the coast, aligning with the pattern of upwelling seasonality. The southern regions experience a more pronounced and quasi-permanent upwelling, characterized by consistently high upwelling index values. In contrast, the northern part of the coast exhibits a decrease in the upwelling index, indicating a higher influence of non-upwelling processes in this area.

These findings suggest that the upwelling phenomenon in this region is influenced not only by seasonal factors but also by additional processes that impact biological productivity. One possible contributing factor could be the presence of mesoscale instabilities, which can influence the distribution and intensity of upwelling events [HILMI et al. [2021]]. Furthermore, marine life activities in the area may also contribute to the variations in upwelling patterns and associated productivity.

In conclusion, the study reveals distinct oceanographic and climatic characteristics between the northern and southern regions of the study area, which result in varying upwelling dynamics. The southern region appears to offer a more favorable environment for upwelling, leading to enhanced biological productivity, while the northern region is more susceptible to non-upwelling processes that can limit the benefits associated with upwelling-related activities.

4.4.7 Interannual variability of the $I^{r}_{sst_{up}}$ and I_E anomalies

4.4.7.1 Anomalies Computation

- Spatial anomalies are calculated as the difference between the new upwelling index values and its corresponding mean values for each image. A positive spatial anomaly signifies an anomalous increase in upwelling activity during that period. Conversely, a negative spatial anomaly indicates an anomalous decrease in upwelling activity (Figure 4.5(a)).

- Temporal anomalies are determined as the difference between the new upwelling index value and its corresponding mean value for each latitude. A positive temporal anomaly indicates an anomalous increase in upwelling activity at a specific latitude. Conversely, a negative temporal anomaly suggests an anomalous decrease in upwelling activity, which may imply weaker upwelling or deviations from typical seasonal patterns (Figure 4.6(a)).

4.4.8 Discussion

We present a detailed space-time Hovmoller diagram illustrating spatial and temporal anomalies from 1982 to 2021 in the upwelling index $I^r_{sst_{up}}$ along the Atlantic coast of Morocco (Figure. 4.5 and Figure. 4.6).

The investigation of interannual variability in spatial and temporal anomalies of the upwelling index $I^r_{sst_{up}}$ along Morocco's Atlantic coast provides valuable insights into annual fluctuations in upwelling intensity and patterns. Through the analysis of these anomalies, we can observe the variations in upwelling conditions over time. The spatial and temporal analysis reveals alternating periods of high and low upwelling intensity throughout the study period (Figure 4.5, Figure. 4.6). This significant interannual variability indicates distinct phases of both strong and weak upwelling along the coast.

Specifically, the years 1995-1996, 1998-2009, and 2012-2021 exhibit notable vertical velocity transport, corresponding to stronger periods in the $I^r_{sst_{up}}$ records. These pronounced anomalies are linked to the collapse of the regional sardine stock between 1996 and 1997, as well as a very low number of juveniles in 1996 and

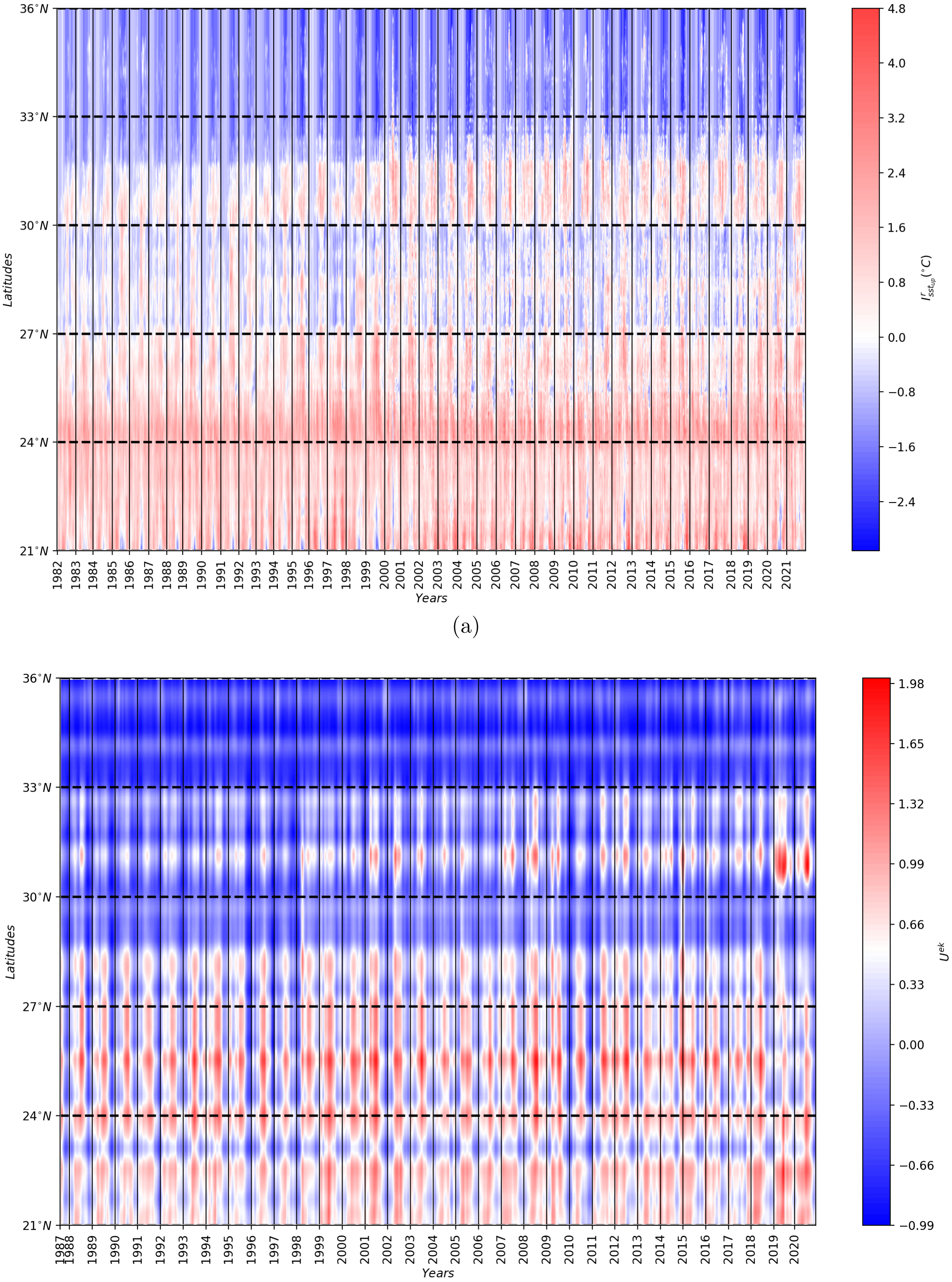

(a)

(b)

Figure 4.5: Space-Time Hovmoller diagram presenting spatial anomalies of: (a): New Upwelling index ($I^r_{sst_{up}}$), (b): Cross-Shore Ekman Transport (I_E), over the period between 1982 − 2021

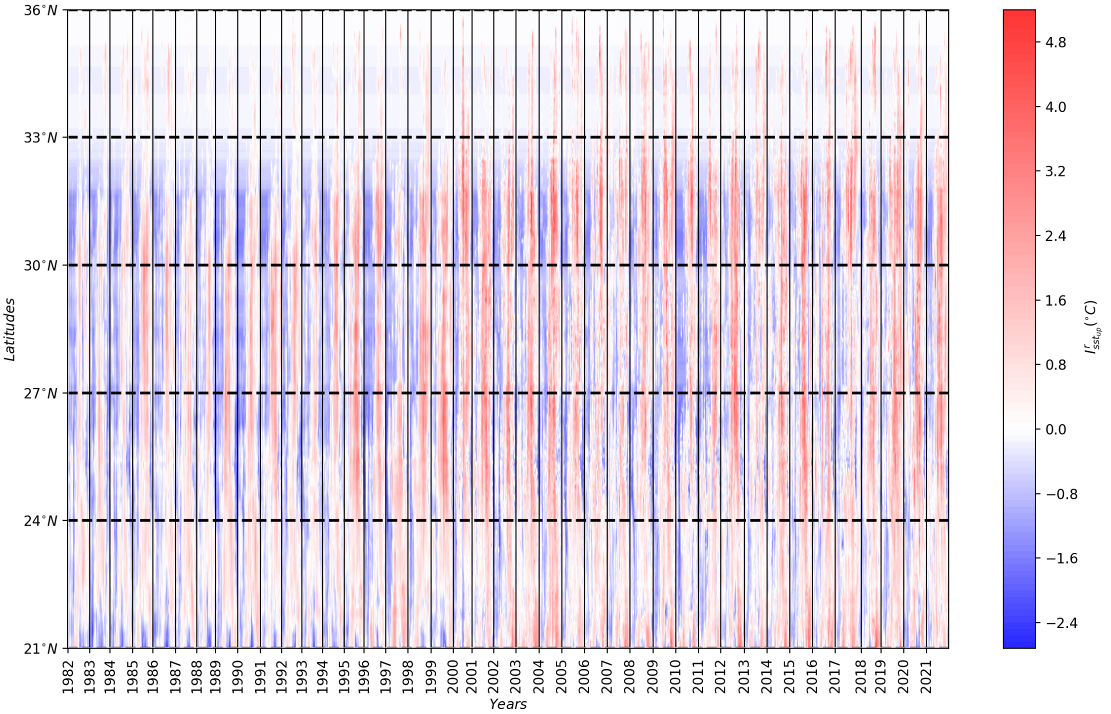

(a)

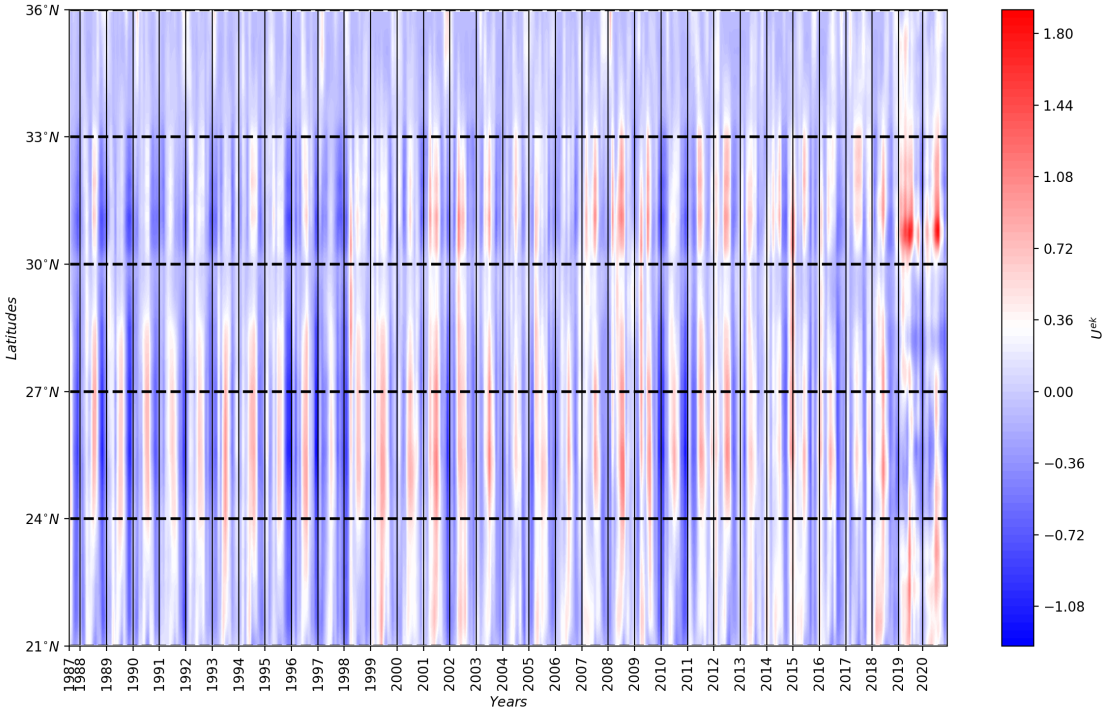

(b)

Figure 4.6: Space-time Hovmoller diagram presenting temporal anomalies of: (a): New Upwelling index ($I^r_{sst_{up}}$), (b): Cross-Shore Ekman Transport (I_E), over the period between $1982 - 2021$

1998 [Machu et al. [2009]] (Figure 4.6a) (Figure. 4.4). On the contrary, certain years display abnormally low yields (Figure 4.6a). The years 1983 to 1994 and 2010 to 2011 stand out as periods of weaker upwelling intensity, accompanied by exceptionally low winds (Figure. 4.6b). Additionally, a distinct zone of very weak upwelling is identified between latitudes $26°N$ and $33°N$ during the years 1996 to 1997 and 2010 to 2011. This weak upwelling is attributed to an exceptional easing of the trade winds during these periods, as shown by Ekman's cross-shore transport data (Figure. 4.6b) [Benazzouz et al. [2015]].

Examining the spatial distribution of upwelling anomalies reveals marked variability along the Moroccan coast (Figure. 4.5a). The southern part consistently experiences higher upwelling intensity compared to other regions. Anomalies in this region suggest a persistent pattern of strong upwelling, particularly during the summer months (June to September), which coincide with stronger winds along the Moroccan coast (Figure 4.5b). These winds are often associated with the intensification of the trade winds. Moving towards the central part of the coast, between latitudes $27°N$ and $33°N$, we observe intermediate levels of upwelling intensity (Figure 4.5a), although they are not as pronounced as in the southern region. The spring (March to May) and autumn (October to November) seasons in this central region can be characterized by a weakening of the trade winds (Figure 4.5b), resulting in reduced upwelling intensity along the coast. In contrast, the northern part of the Moroccan coast exhibits little or no upwelling, indicating weak or sporadic upwelling and relatively low upwelling intensity.

The interannual variability of spatial and temporal anomalies highlights the dynamic nature of upwelling along Morocco's Atlantic coast. These fluctuations can have significant impacts on the productivity and distribution of marine organisms, including fish populations and phytoplankton blooms.

4.4.9 Conclusion

In this section, we developed a novel upwelling index that combines physical and biological observations, aimed at studying upwelling activity along the Moroccan Atlantic coast, spanning from ($21°N$ to $36°N$ and $6°E$ to $19°E$). Our analysis involved two upwelling indices: the 'new upwelling index' ($I^r_{sst_{up}}$) and the 'Ekman transport' index (I_E). We examined their spatial and temporal anomalies at each latitude, capturing the interannual variability. Utilizing 40 years (1982-2021) of satellite images, we investigated and analyzed upwelling activity in the Moroccan region. For better organization, we divided the study area into three distinct sub-regions, each exhibiting unique characteristics. An imprtant aspect of our research involved comparing our new upwelling index with a previously developed index from another study [El Aouni et al. [2019]], as well as the Ekman transport index. Our findings revealed that our new upwelling index offers notably enhanced precision in portraying upwelling dynamics. Unlike the other index, our approach proves to be more effective in analyzing upwelling and is adaptable to varying time resolutions. Moreover, the methodology we developed can be easily customized for examining upwelling phenomena in different regions worldwide. To gain deeper insights into the patterns of low and high upwelling activity, we selected three specific sites ($24°N$, $29°N$, $31°N$) from the new upwelling index. Additionally, we evaluated the effectiveness of each satellite observation within each sub-region, providing valuable recommendations for improved monitoring and tracking of upwelling events.

4.5 Identification of new SST and CHL-*a* indices: A comparative study for improved upwelling monitoring in Northwest Africa.

In this section, we develop new indices based on SST and CHL-*a* images [Belmajdoub et al. [2023a]]. The first to evaluate the variability of the cold-nutrient upwelling water, and the second to assess its presence. These indices are simple and intuitive and aim to revolutionize upwelling monitoring in the dynamic region of North-West Africa. A comprehensive comparative study is carried out on the basis of these indices, meticulously examining their effectiveness and accuracy in detecting and monitoring upwelling events.

4.5.1 Indices calculation

The first index is defined as the mean average of the upwelling temperature and CHL-*a* concentration for each radial. This average is calculated within the the extracted upwelling regions (up) indicated by the white line in Figure 3.3. Starting from North to South, each radial $r \epsilon \{1.....n\}$ contains temperature values $r = \{T_i^r; i = 1.....n\}$, and CHL-*a* concentration values $r = \{C_i^r; i = 1.....n\}$. Therefore, over each radial, this index is defined as:

$$I_{\text{s}}^r = \text{mean}(T_{i_{up}}^r) \ (1) \qquad I_{\text{c}}^r = \text{mean}(\log_{10}(C_{i_{up}}^r)) \ (2)$$

The result of I_{s}^r and I_{c}^r are represented in figure 4.7.

The second upwelling index is based on the use of the binary images of SST and CHL-*a* (White color in predicted segmentation represents the upwelling area). The goal of this index is to verify the upwelling existence over each radial, taking into account false-positive cold and high CHL-*a* concentration water, and it is computed as described in the Algorithm 1.

Algorithm 1 upwelling existence

```
  Input $SI_{SST}$, $SI_{chl-a}$        Output $I^r_{bs}$, $I^r_{bc}$
for $r$ in $\{1.....n\}$ do
    if (any($SI^r_{SST}$)) ==1 || (any($SI^r_{chl-a}$)) ==1 then
        $I^r_{bs}$, $I^r_{bc}$ are upwelling
    else
        if (any($SI^r_{SST}$)) == -1 || (any($SI^r_{chl-a}$)) ==-1 then
            $I^r_{bs}$ , $I^r_{bc}$ are cloud
        else    $I^r_{bs}$, $I^r_{bc}$ are no-upwelling
        end if
    end if
end for
```

The input for the algorithm is denoted by SI_{SST} and SI_{CHL-a}, which correspond to the SST and CHL-a images, respectively. Additionally, I^r_{bs} and I^r_{bc} represent the calculated indices for SST and CHL-a respectively. The resulting index values are visualized via a Hovmoller diagram showing the presence of upwelling (see (fig.4.8)).

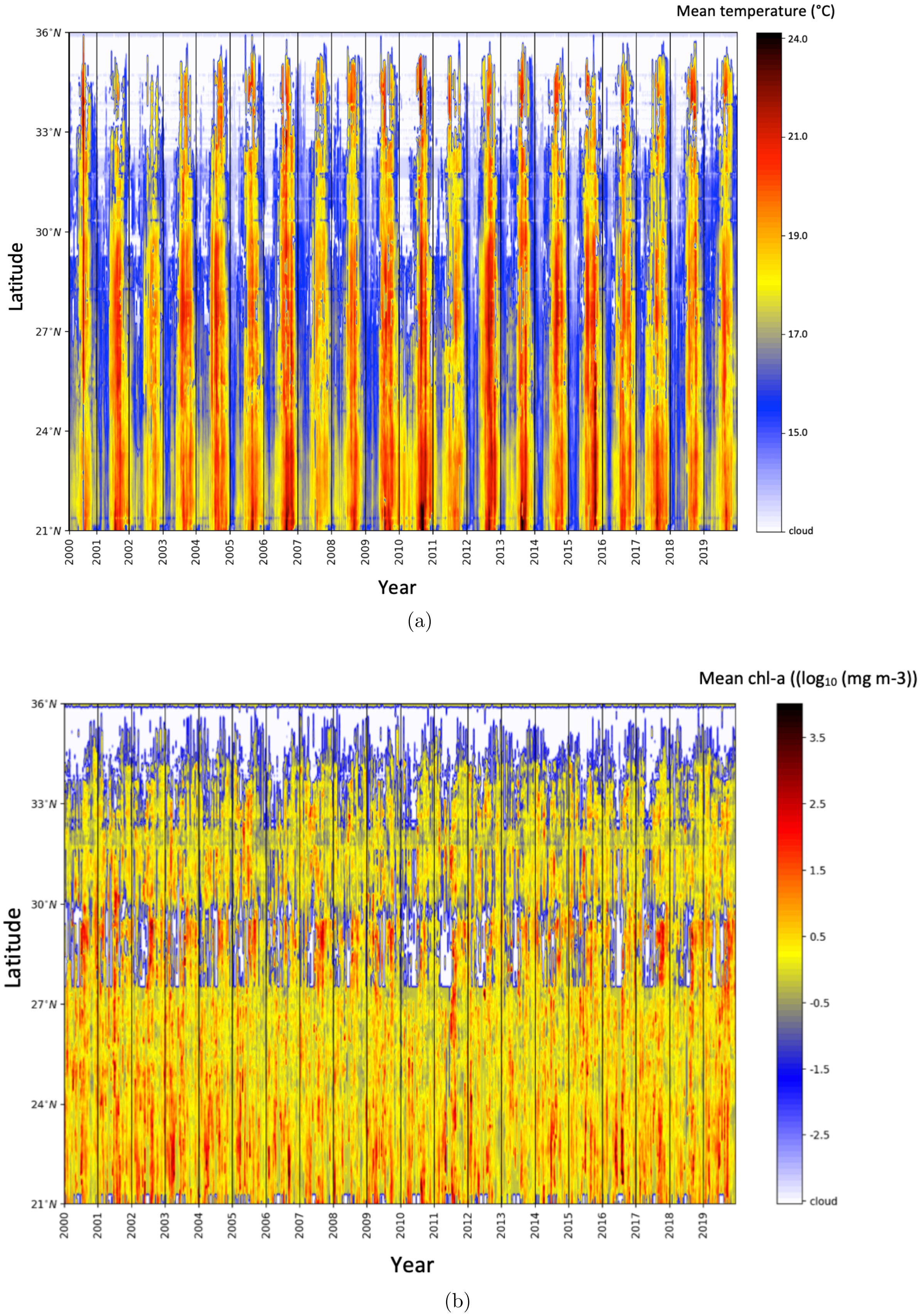

Figure 4.7: Space-time Hovmoller diagram of (a) mean-averaged temperature computed from SST images, (b) mean-averaged CHL-a concentration computed from CHL-a images.

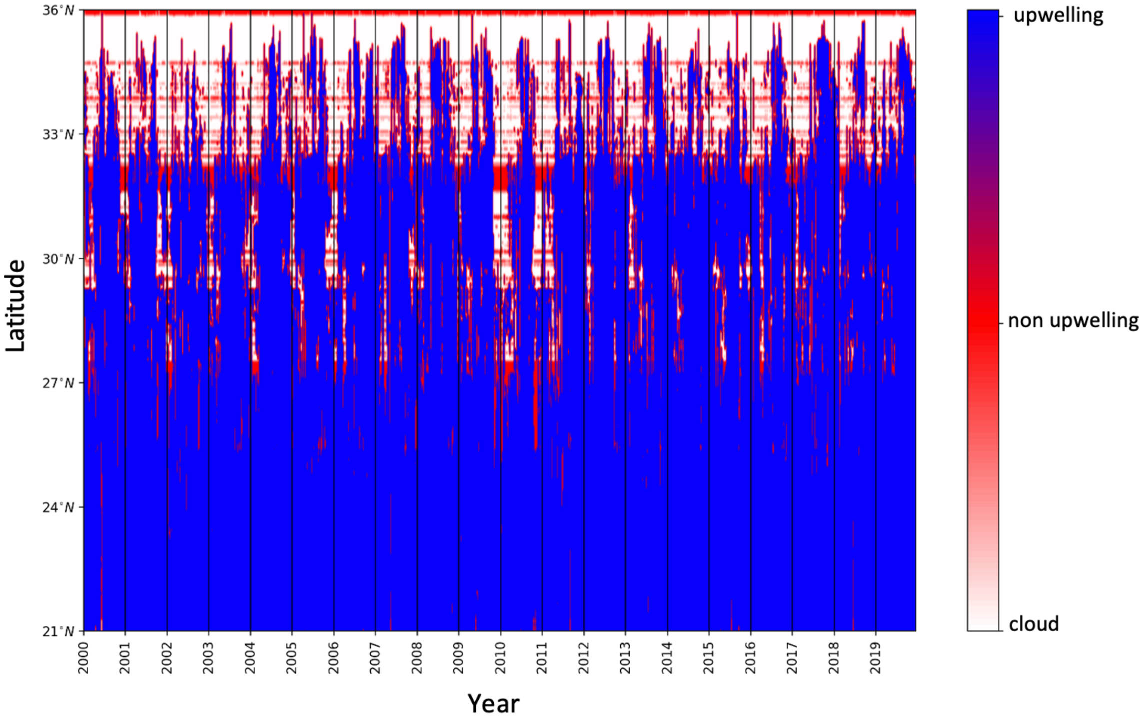

(a)

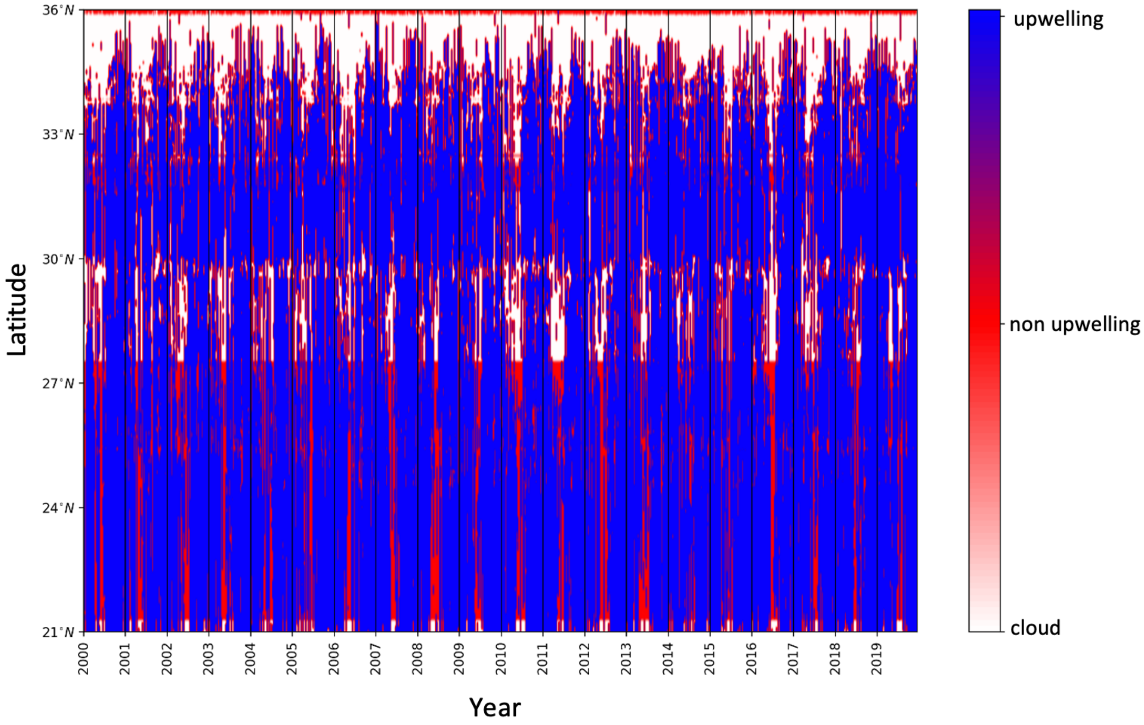

(b)

Figure 4.8: Hovmoller diagram showing the presence of upwelling, none-upwelling, and cloud, (a) from SST images, and (b) over CHL-a images.

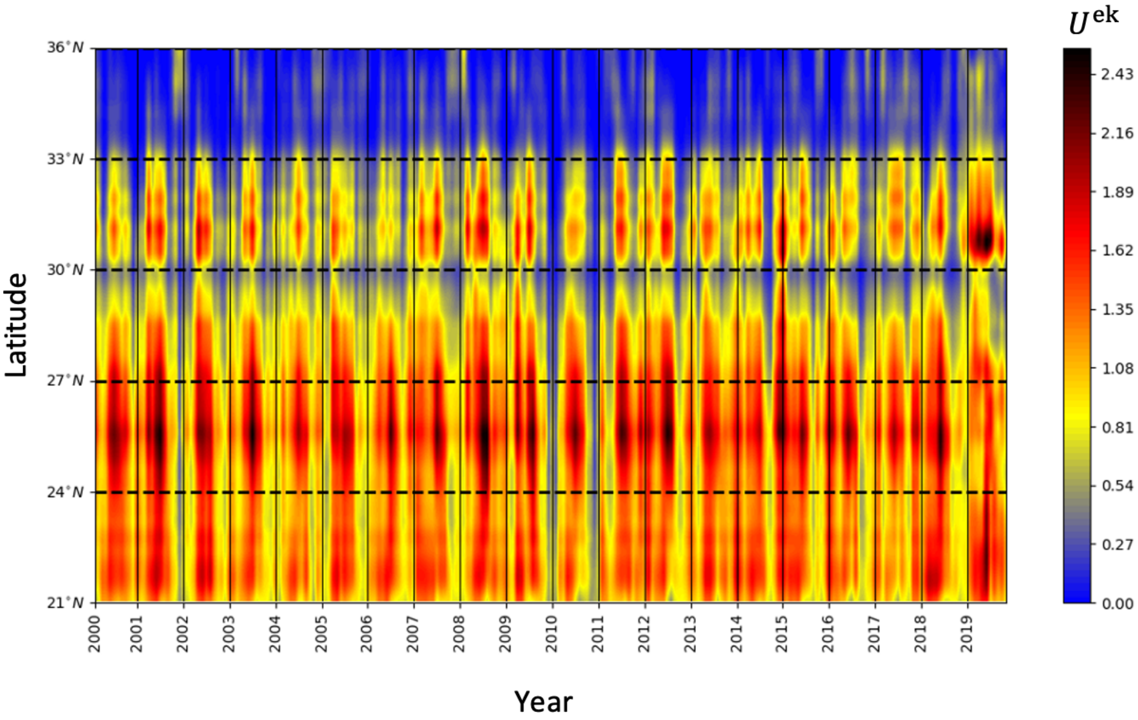

Figure 4.9: Hovemoller diagram of the Cross-Shore Ekman Transport between 2000 and 2019.

4.5.2 Discussion

The proposed indices are used to study the seasonal and interannual variability of the upwelling dynamics via Hovmoller-diagrams computed from SST (figure 4.7) and CHL-a (figure 4.8) for the period between 2000-2019.

The main upwelling patterns computed from physical and biological observation are generally the same, and they are very comparable to that of the Cross-shore Ekman transport (Figure 4.9). This alignment with the wind-based upwelling index validates our new indices, and allows to further analyze sub-mesoscale fluctuations which are not captured by the wind (25km) but are indeed captured by the new indices(4km). Our results suggest that our system can be synthesized into four distinguished regions:

Southern part between (21°N, 27°N): the thermal interannual and seasonal variability of the upwelling confirms its presence and strength throughout the years (fig.4.8.a) with maximum temperature from summer to autumn, especially during the years of 2010 and 2012, and it decreases by $2 \sim 8$ in spring.(figure 4.7.a). In the biological side, interesting discontinuities of upwelling presence were observed. Indeed, it is absent from June to September in all years, except the years 2000 and 2001 where the upwelling is absent also in spring (figure 4.8.b). The maximum CHL-a concentration is between November and May, with few weeks delays from year to year, with extreme event being recorded during the years 2011 and 2018. (figure 4.7.b). In this region, the physical observations detect more upwelling and therefore are more reliable than the CHL-a.

Part between (27°N, 30°N): the upwelling temperature is quite comparable to the one above, with the appearance of some parts of the cloud in winter and spring near Cape Ghir (30°N) (figure 4.7.a). On the other side, the CHL-a images show even further more clouds, mainly from February to December (figure 4.8.b), with a winter pattern quite similar to that observed in Ekman transport, which can explain the presence of the clouds during that particular period of the year which is associated with decrease of the wind intensity and changes in their direction. The overall finding makes this area characterized by intense upwelling with moderate presence. Similar to the region above, the SST parameter detects more upwelling than the CHL-a parameter.

Part between (30°N, 33°N): it is characterized by moderate temperature throughout the years (figure 4.7.a), with a seasonality in the upwelling presence varying both yearly and meridionally with interesting anomalies, particular in 2010 (figure 4.8.a). For the CHL-a images, the upwelling is present in all years, with few weeks where upwelling is absent. (fig.4.8.b), with a general moderate CHL-a concentration throughout the years (figure 4.7.b). Contrary to the aforementioned regions, this one clearly shown the upwelling is more present in the biological observation and this is mainly related to surface mixing and stirring associated with high jets (strong ocean currents that occur close to the surface) and other instabilities that are often developed in the region.

The northern part between ($33°N$, $36°N$): all the years suggest low upwelling in the SST images with intense presence of clouds, which decreases in the CHL-*a* images, but it still remains generally low compared to the rest of the system (figure 4.8.b).

4.5.3 Conclusion

In this section we have proposed new upwelling indices based both on physical and biological observations. These indices are computed based on our proposed method developed in previous chapter which takes into account the physics creating the phenomenon, therefore it gives more insight into its dynamics. Moreover, the new indices are very comparable to the classical one, based on the Ekman transport, but now they allow observation of submesoscale fluctuations which is not the case in the wind data. We used these indices over a period of 20 years worth of satellite images to study and analyze the upwelling activity in the region. Moreover, we analyzed the performance of each satellite observation over each sub-region, to allow further recommendations for better upwelling monitoring and tracking.

CHAPTER

5

GENERAL CONCLUSION AND OUTLOOK

5.1 Introduction

The Eastern Boundary Upwelling Zones encompass some of the world's most productive ecosystems, with a notable example being the Canary Current upwelling system, which represents a globally important upwelling region. This thesis strives to undertake an interdisciplinary exploration of coastal upwelling systems, addressing various objectives that include improving automated detection and retrieval of upwelling events along the Moroccan Atlantic coast. In addition, it aimed to advance coastal upwelling monitoring in various coastal regions, using satellite-derived SST images. Furthermore, it presented a comprehensive statistical analysis of spatio-temporal variations in upwelling in the NWA region, introducing and examining a series of new upwelling-related indices.

The current chapter serves as a recapitulation and synthesis of the key concepts presented in the preceding chapters. It enables us to draw pertinent conclusions and underscore the substantial contributions made by the research detailed in this thesis. Furthermore, it offers insights into future research prospects, with a specific focus on advancing the functionality and efficiency of deep learning models for tracking, extracting, and identifying upwelling regions.

5.2 Synthesis of the main ideas from previous chapters

This thesis explored in detail previous methodologies developed for the specific task of delineating upwelling regions within the Moroccan context reveals a common approach in Chapter 2. These methods typically start by applying a clustering algorithm to SST images with a specified cluster number, denoted as ”c = 2.” This initial step serves to segregate the colder upwelling waters from the warmer offshore waters. The cluster with the minimum centroid value is subsequently labeled as the upwelling water cluster. Following this, a regional growth algorithm is employed to eliminate noisy structures within the offshore waters. This procedure operates under the assumption that all pixels belonging to the upwelling region must exhibit connectivity with the coastline. Nevertheless, these techniques have proven effective primarily in the southern sector of the system. This limited success can be attributed to the substantial variability in temperature distribution along the latitudinal axis. The disparity in solar energy distribution across the entire system results in temperatures near the northern coastline often resembling those in the southern upwelling zones. A critical point to note is that conventional clustering algorithms primarily consider pixel temperatures, neglecting their geographical context. Consequently, these algorithms tend to misclassify northern offshore temperatures as indicative of upwelling water without taking into account their actual geographic location. In an effort to resolve this challenge, two distinct approaches have emerged in the literature for the identification and extraction of upwelling regions along the entirety of the Moroccan Atlantic coast. The first method involves the application of latitudinal normalization, leveraging offshore temperatures as a key reference point. Meanwhile, the second approach adopts a region-specific clustering strategy tailored to the unique characteristics of each region.

Despite the existence of numerous methods for detecting coastal upwelling, they encounter three primary challenges. Firstly, they are frequently time-consuming due to their reliance on optimization techniques. Secondly, their effectiveness often depends significantly on the specific type of input data utilized. Lastly, even the most recently developed method for identifying upwelling along the Moroccan Atlantic coast, as detailed in [El Aouni et al. [2020]] study, encounters difficulties in accurately identifying the northern segment of the Moroccan upwelling ecosystem within certain SST images. It's important to note that there is no universally applicable method for detecting upwelling in major coastal areas.

To address these limitations and improve global monitoring of coastal upwelling phenomena, we have proposed in Chapter 3 new deep learning techniques to improve the identification of upwelling regions using physical and biological satellite data. Our approach incorporated a convolutional neural network (CNN) structured on an encoder-decoder framework inspired by the U-Net architecture, adapted to the localization of upwelling regions. The U-Net architecture offers distinct advantages over previous methodologies, such as efficient feature extraction and high-level feature recognition, enabling more accurate predictions of upwelling regions. It has also demonstrated robustness in dealing with the noise and variability commonly found in satellite images of the oceans, and adapts to the large datasets essential for the segmentation of upwelling regions, where it is imperative to process many satellite images.

In addition, we have introduced a refinement model based on deep residual networks (ResNets), known as "DeepRes-UpwellNet". This fully end-to-end convolutional neural network is specifically designed to detect upwelling regions in SST and CHL-a satellite images of the sea. Although based on the U-Net structure, it incorporates substantial enhancements to support deeper and more complex networks. Our method not only successfully meets the challenge of upwelling detection in the northern region of the Moroccan Atlantic coast, but also identifies the smallest upwelling zones.

Finally, we presented the "DeepCoast$_{up}$-Net" architecture, a complete solution for identifying upwelling regions in major coastal areas, effectively exploiting the potential of SST satellite imagery. A significant contribution of this work is the development of a model exclusively trained on SST data collected along the Atlantic coast of Morocco. Although trained on a specific region, this model has demonstrated its ability to accurately segment upwelling regions in diverse coastal zone. The model is fed by images captured along Morocco's Atlantic coast, with each pixel represented by three distinct channels: SST, latitudinal position, and distance from the coast. These channels collectively serve as input to the U-Net model, which is trained with the corresponding masks to acquire the ability to segment upwelling regions within the supplied dataset. Once trained, the model demonstrated an exceptional ability to generalize its knowledge beyond the boundaries of the Moroccan region. When tasked with segmenting new regions, it skilfully delineates and extracts upwelling patterns, even in regions it has not been explicitly trained on.

In the last chapter of our study, we leverage the upwelling extraction method outlined in Chapter 3 to formulate new indices. The initial section introduced an enhancement to the classical coastal upwelling index. This index traditionally relies on a basic thermal disparity between coastal and nearshore temperatures, measured at a specific latitude denoted as $CUI_{SST} = SST_{max}$ - SST_{min} Various approaches to determining the SST_{min} and SST_{max} have been suggested in prior literature. Our novel approach introduces a distinct perspective.

In contrast to the conventional fixed-band methods that solely consider SST_{min} in proximity to the coast, our revised upwelling index identifies SST_{min} as the minimum temperature within the upwelling zone. This approach provides a more comprehensive calculation, encompassing all crucial low temperatures, as SST_{min}

inherently belongs to the Upwelling region. Moreover, we depart from established practices in the literature where SST_{max} is designated as the offshore temperature, assuming negligible Upwelling influence. We define SST_{max} as the maximum temperature within the Upwelling region, eliminating arbitrary position selection and focusing solely on the Upwelling zone. Consequently, SST^{up}_{min} and SST^{up}_{max} represent the lowest and highest coastal temperatures within the upwelling zone, respectively. This methodology underpins our 40-year historical analysis of upwelling intensity variations.

In the subsequent section, we formulate new indices utilizing SST and CHL-a images. The first index quantifies the variability of cold, nutrient-rich upwelling water, while the second assesses its presence. These indices are straightforward and intuitive, marking a significant advancement in upwelling monitoring within the dynamic Northwest Africa region. Over a two-decade period of satellite imagery, we employed these indices to scrutinize and comprehend upwelling activity in the area. Additionally, we evaluated the performance of each satellite observation within distinct sub-regions, enabling us to provide recommendations for better upwelling monitoring and tracking methodologies.

5.3 Outlook

Given the progress made during this thesis in identifying upwelling zones using deep learning models, and in defining new upwelling indices, this work has deepened our understanding of the various aspects of the NWA upwelling system. In terms of future prospects, and as an extension of this study, several avenues of research have been put forward to deepen the analysis and understanding of the upwelling phenomenon.

As a future work, we are considering the use of transformer models to improve the precision and efficiency of our analyses. Indeed, transformers were initially designed for natural language processing tasks but have since found applications in various domains, including computer vision. The architecture is particularly renowned for its ability to capture long-term dependencies through self-attention mechanisms, making it a promising candidate for tasks such as semantic segmentation. These models could facilitate a better interpretation of data and a more accurate identification of upwelling zones. The potential directions for integrating transformer-based models in the study of upwelling regions are described below:

- Develop transformation models capable of better understanding the information contained in SST images, enabling more precise delineation of upwelling regions.
- Train transformer models on various datasets collected in different coastal zones around the world to assess their global applicability and ability to adapt to different geographical contexts and upwelling characteristics.
- Investigate the potential of transformer models in the analysis of long-term historical data to study variations in upwelling intensity and predict future trends.

By examining the spatial extent of Moroccan upwelling through physical and biological observations, we have noted that upwelling is detectable in CHLa images in the northern region, but not in the SST images in this specific area. Therefore, it would be relevant to develop models capable of simultaneously processing SST and CHL-a satellite images. This would allow for the capture of complex relationships between different types of data.

BIBLIOGRAPHY

Rolf Adams and Leanne Bischof. Seeded region growing. *IEEE Transactions on pattern analysis and machine intelligence*, 16(6):641–647, 1994.

RF Anderson, S Ali, LI Bradtmiller, SHH Nielsen, MQ Fleisher, BE Anderson, and LH Burckle. Wind-driven upwelling in the southern ocean and the deglacial rise in atmospheric co2. *science*, 323(5920):1443–1448, 2009.

Abderrahmane Atillah, Abdellatif Orbi, Karim Hilmi, and Antoine Mangin. Produits opérationnels dâocéanographie spatiale pour le suivi et lâanalyse du phénomene dâupwelling marocain. *Geo Observateur*, 14:49–62, 2005.

Vijay Badrinarayanan, Alex Kendall, and Roberto Cipolla. Segnet: A deep convolutional encoder-decoder architecture for image segmentation. *IEEE transactions on pattern analysis and machine intelligence*, 39(12):2481–2495, 2017.

Andrew Bakun. Global climate change and intensification of coastal ocean upwelling. *Science*, 247(4939):198–201, 1990.

Alexander Barth, Aida Alvera-Azcárate, Charles Troupin, and Jean-Marie Beckers. Dincae 2.0: multivariate convolutional neural network with error estimates to reconstruct sea surface temperature satellite and altimetry observations. *Geoscientific Model Development*, 15(5):2183–2196, 2022.

Eric D Barton and Javier Arístegui. The canary islands coastal transition zone–upwelling, eddies and filaments. 2004.

Hanae Belmajdoub and Khalid Minaoui. Deepres-upwellnet: A robust framework for coastal upwelling monitoring along the moroccan atlantic coast. In *submited to :International Conference on Advances in Data-Driven Analytics and Intelligent Systems (ADACIS2023)*.

Hanae Belmajdoub, Khalid Minaoui, Anass El Aouni, and El Abidi Zineb. Deep learning monitoring of upwelling regions in major coastal zones using satellite images of sea surface temperature. *submited to : International Journal of Remote Sensing.*

Hanae Belmajdoub, Zineb Elabidi, and Khalid Minaoui. Automatic detection of moroccan coastal upwelling from chlorophyll-a concentration images using the expectation-maximization method. In *2022 11th International Symposium on Signal, Image, Video and Communications (ISIVC)*, pages 1–5. IEEE, 2022.

Hanae Belmajdoub, Anass El Aouni, and Khalid Minaoui. Convolutional neural networks for coastal upwelling monitoring along the atlantic coast of morocco. *Remote Sensing Letters*, 14(8):775–785, 2023a.

Hanae Belmajdoub, Khalid Minaoui, Anass El Aouni, Karim Hilmi, Rachid Saadane, and Abdellah Chehri. A new upwelling index for the moroccan atlantic coast for the period between 1982–2021. *Remote Sensing*, 15(14):3459, 2023b.

Aïssa Benazzouz, Soumia Mordane, Abdellatif Orbi, Mohamed Chagdali, Karim Hilmi, Abderrahman Atillah, Josep Lluís Pelegrí, and Demarcq Hervé. An improved coastal upwelling index from sea surface temperature using satellite-based approach–the case of the canary current upwelling system. *Continental Shelf Research*, 81:38–54, 2014.

Aïssa Benazzouz, Hervé Demarcq, and Gonzalo González-Nuevo. Recent changes and trends of the upwelling intensity in the canary current large marine ecosystem. 2015.

D Boyd. Physical basis of remote sensing. *Journal of Geoinformatics*, 1:67–81, 2005.

P Bradley, U Fayyad, and C Reina. Scaling em (expectation-maximization) clustering to large databases. microsoft research. Technical report, MSR-TR-98-35, 1998.

John Canny. A computational approach to edge detection. *IEEE Transactions on pattern analysis and machine intelligence*, (6):679–698, 1986.

K Ll Carder, FR Chen, JP Cannizzaro, JW Campbell, and BG Mitchell. Performance of the modis semi-analytical ocean color algorithm for chlorophyll-a. *Advances in Space research*, 33(7):1152–1159, 2004.

Joao Carreira, Rui Caseiro, Jorge Batista, and Cristian Sminchisescu. Semantic segmentation with second-order pooling. In *Computer Vision–ECCV 2012: 12th European Conference on Computer Vision, Florence, Italy, October 7-13, 2012, Proceedings, Part VII 12*, pages 430–443. Springer, 2012.

Jean-Francois Cayula and Peter Cornillon. Edge detection algorithm for sst images. *Journal of atmospheric and oceanic technology*, 9(1):67–80, 1992.

Jean-François Cayula and Peter Cornillon. Multi-image edge detection for sst images. *Journal of Atmospheric and Oceanic Technology*, 12(4):821–829, 1995.

Emmanuel Chassot, Sylvain Bonhommeau, Gabriel Reygondeau, Karen Nieto, Jeffrey J Polovina, Martin Huret, Nicholas K Dulvy, and Herve Demarcq. Satellite remote sensing for an ecosystem approach to fisheries management. *ICES Journal of Marine Science*, 68(4):651–666, 2011.

Liang-Chieh Chen, Yukun Zhu, George Papandreou, Florian Schroff, and Hartwig Adam. Encoder-decoder with atrous separable convolution for semantic image segmentation. In *Proceedings of the European conference on computer vision (ECCV)*, pages 801–818, 2018.

Zhaoyun Chen, Xiao-Hai Yan, Yuwu Jiang, Lide Jiang, and Young-Heon Jo. A study of cross-shore maximum upwelling intensity along the northwest africa coast. *Journal of oceanography*, 69:443–450, 2013.

Angela Colling. *Ocean circulation*, volume 3. Butterworth-Heinemann, 2001.

Russell G Congalton. Remote sensing: an overview. *GIScience & Remote Sensing*, 47(4):443–459, 2010.

Clément Dechesne, Pierre Lassalle, and Sébastien Lefèvre. Bayesian u-net: Estimating uncertainty in semantic segmentation of earth observation images. *Remote Sensing*, 13(19):3836, 2021.

Hervé Demarcq and Valérie Faure. Coastal upwelling and associated retention indices derived from satellite sst. application to octopus vulgaris recruitment. *Oceanologica Acta*, 23(4):391–408, 2000.

Hervé Demarcq, R Barlow, and L Hutchings. Application of a chlorophyll index derived from satellite data to investigate the variability of phytoplankton in the benguela ecosystem. *African Journal of Marine Science*, 29(2):271–282, 2007.

Vagn Walfrid Ekman. On the influence of the earth's rotation on ocean-currents. 1905.

Zineb El Abidi, Khalid Minaoui, Anass El Aouni, Ayoub Tamim, and Hicham Laanaya. An efficient detection of moroccan coastal upwelling based on fusion of chlorophyll-a and sea surface temperature images with a new validation index. *IEEE Geoscience and Remote Sensing Letters*, 2020.

Anass El Aouni, Khalid Minaoui, Ayoub Tamim, Khalid Daoudi, Hussein Yahia, Abderrahman Atillah, and Driss Aboutajdine. Detection of moroccan coastal upwelling using sea surface chlorophyll concentration. In *2015 IEEE/ACS 12th International Conference of Computer Systems and Applications (AICCSA)*, pages 1–4. IEEE, 2015.

Anass El Aouni, Véronique Garçon, Joël Sudre, Hussein Yahia, Khalid Daoudi, and Khalid Minaoui. Physical and biological satellite observations of the northwest african upwelling: Spatial extent and dynamics. *IEEE Transactions on Geoscience and Remote Sensing*, 58(2):1409–1421, 2019.

Anass El Aouni, Khalid Daoudi, Khalid Minaoui, and Hussein Yahia. Robust detection of the north-west african upwelling from sst images. *IEEE Geoscience and Remote Sensing Letters*, 18(4):573–576, 2020.

Hani El Assaad, Allou Samé, Gérard Govaert, and Patrice Aknin. A variational expectation–maximization algorithm for temporal data clustering. *Computational Statistics & Data Analysis*, 103:206–228, 2016.

Reham Elshamy, Osama Abu-Elnasr, Mohamed Elhoseny, and Samir Elmougy. Improving the efficiency of rmsprop optimizer by utilizing nestrove in deep learning. *Scientific Reports*, 13(1):8814, 2023.

Nathan R Evans, Dana L Woodruff, and Vera L Trainer. Development of coastal upwelling edge detection algorithms associated with harmful algal blooms off the washington coast using sea surface temperature imagery. In *Remote Sensing of the Coastal Oceanic Environment*, volume 5885, pages 168–173. SPIE, 2005.

Jianping Fan, Guihua Zeng, Mathurin Body, and Mohand-Said Hacid. Seeded region growing: an extensive and comparative study. *Pattern recognition letters*, 26(8):1139–1156, 2005.

Richard A Feely, Christopher L Sabine, J Martin Hernandez-Ayon, Debby Ianson, and Burke Hales. Evidence for upwelling of corrosive" acidified" water onto the continental shelf. *science*, 320(5882):1490–1492, 2008.

RC Gonzalez and RE Woods. Digital image processing prentice hall, upper saddle river. *NJ, USA,*, 2002.

Ian Goodfellow, Yoshua Bengio, and Aaron Courville. *Deep learning*. MIT press, 2016.

Annalisa Griffa, AD Kirwan Jr, Arthur J Mariano, Tamay Özgökmen, and H Thomas Rossby. *Lagrangian analysis and prediction of coastal and ocean dynamics*. Cambridge University Press, 2007.

Belmajdoub Hanae, Minaoui Khalid, El Aouni Anass, Hilmi Karim, Saadane Rachid, and Chehri Abdellah. A new upwelling index for the moroccan atlantic coast for the period between 1982–2021. *Remote Sensing*, 15(14):3459, 2023.

Dominica Harrison, Fabio Cabrera De Leo, Warren J Gallin, Farin Mir, Simone Marini, and Sally P Leys. Machine learning applications of convolutional neural networks and unet architecture to predict and classify demosponge behavior. *Water*, 13(18):2512, 2021.

R Haynes, Eric D Barton, and I Pilling. Development, persistence, and variability of upwelling filaments off the atlantic coast of the iberian peninsula. *Journal of Geophysical Research: Oceans*, 98(C12):22681–22692, 1993.

Karim HILMI, Ismail BESSA, Ahmed MAKAOUI, Rachid HOUSSA, Mohammed IDRISSI, Omar ETTAHIRI, and Anass EL AOUNI. Long term upwelling activity along the moroccan atlantic coast. *Frontiers in Science and Engineering*, 11(1), 2021.

Soe Hlaing, Tristan Harmel, Alexander Gilerson, Robert Foster, Alan Weidemann, Robert Arnone, Menghua Wang, and Samir Ahmed. Evaluation of the viirs ocean color monitoring performance in coastal regions. *Remote Sensing of Environment*, 139:398–414, 2013.

Ronald J Holyer and Sarah H Peckinpaugh. Edge detection applied to satellite imagery of the oceans. *IEEE transactions on geoscience and remote sensing*, 27 (1):46–56, 1989.

A Huete, K Didan, T Miuraa, EP Rodrigueza, X Gaoa, and LG Ferreirab. The moderate resolution imaging spectroradiometer (modis): a new generation of land surface monitoring. *Remote Sensing of Environment*, 83:195–213, 2002.

Adriana Huyer. Coastal upwelling in the california current system. *Progress in oceanography*, 12(3):259–284, 1983.

Sergey Ioffe and Christian Szegedy. Batch normalization: Accelerating deep network training by reducing internal covariate shift. In *International conference on machine learning*, pages 448–456. PMLR, 2015.

Jochen Kämpf and Piers Chapman. *Upwelling systems of the world.* Springer, 2016.

Minaoui Khalid et al. A simple tool for automatic extraction of the moroccan coastal upwelling from sea surface chlorophyll images. In *2017 Intelligent Systems and Computer Vision (ISCV)*, pages 1–4. IEEE, 2017.

JFC Kingman. G. matheron, random sets and integral geometry. 1975.

Devyani Lambhate, Raghav Sharma, Jenifer Clark, Avijit Gangopadhyay, and Deepak Subramani. W-net: A deep network for simultaneous identification of gulf stream and rings from concurrent satellite images of sea surface temperature and height. *IEEE Transactions on Geoscience and Remote Sensing*, 60:1–13, 2021.

Cyril Lathuiliere, Vincent Echevin, and Marina Lévy. Seasonal and intraseasonal surface chlorophyll-a variability along the northwest african coast. *Journal of Geophysical Research: Oceans*, 113(C5), 2008.

Yann LeCun, Yoshua Bengio, and Geoffrey Hinton. Deep learning. *nature*, 521 (7553):436–444, 2015.

Rui Li, Chenxi Duan, Shunyi Zheng, Ce Zhang, and Peter M. Atkinson. Macu-net for semantic segmentation of fine-resolution remotely sensed images. *IEEE Geoscience and Remote Sensing Letters*, 19:1–5, 2022. doi: 10.1109/LGRS.2021.3052886.

Thomas Lillesand, Ralph W Kiefer, and Jonathan Chipman. *Remote sensing and image interpretation.* John Wiley & Sons, 2015.

Thomas M Lillisand, Ralph W Kiefer, and Jonathan W Chipman. Remote sensing and image interpretation, 2000.

W Timothy Liu. Progress in scatterometer application. *Journal of Oceanography*, 58:121–136, 2002.

Yingjie Liu and Xiaofeng Li. Eddy-induced chlorophyll-a variations in the northern indian ocean: A study using multi-source satellite data and deep learning. *EGUsphere*, 2023:1–24, 2023.

Yingjie Liu, Xiaofeng Li, and Yibin Ren. A deep learning model for oceanic mesoscale eddy detection based on multi-source remote sensing imagery. In *IGARSS 2020-2020 IEEE International Geoscience and Remote Sensing Symposium*, pages 6762–6765. IEEE, 2020.

Jonathan Long, Evan Shelhamer, and Trevor Darrell. Fully convolutional networks for semantic segmentation. In *Proceedings of the IEEE conference on computer vision and pattern recognition*, pages 3431–3440, 2015.

Eric Machu, O Ettahiri, S Kifani, A Benazzouz, A Makaoui, and Hervé Demarcq. Environmental control of the recruitment of sardines (sardina pilchardus) over the western saharan shelf between 1995 and 2002: a coupled physical/biogeochemical modelling experiment. *Fisheries Oceanography*, 18(5):287–300, 2009.

Raman Maini and Himanshu Aggarwal. Study and comparison of various image edge detection techniques. *International journal of image processing (IJIP)*, 3 (1):1–11, 2009.

Javier Marcello, Ferran Marqués, and Francisco Eugenio. Automatic tool for the precise detection of upwelling and filaments in remote sensing imagery. *IEEE Transactions on Geoscience and Remote Sensing*, 43(7):1605–1616, 2005.

Javier Marcello, Alonso Hernandez-Guerra, Francisco Eugenio, and Abenauara Fonte. Seasonal and temporal study of the northwest african upwelling system. *International Journal of Remote Sensing*, 32(7):1843–1859, 2011.

Ramón Margalef. Phytoplankton communities in upwelling areas. the example of nw africa. *Oecologia aquatica*, 3(3):97–132, 1978.

F Milletari, N Navab, SA Ahmadi, and V-net. Fully convolutional neural networks for volumetric medical image segmentation. In *2016 Fourth International Conference on 3D Vision (3DV)*, pages 565–571.

PJ Minnett. Sea surface temperature measurements from the moderate-resolution imaging spectroradiometer (modis) on aqua. In *AGU Fall Meeting Abstracts*, volume 2003, pages H22H–03, 2003.

Abhijit Mitra and Sufia Zaman. *Environmental Science-A ground zero observation on the Indian subcontinent.* Springer, 2020.

Ekkehard Mittelstaedt. The ocean boundary along the northwest african coast: Circulation and oceanographic properties at the sea surface. *Progress in Oceanography*, 26(4):307–355, 1991.

Yara Mohajerani, Michael Wood, Isabella Velicogna, and Eric Rignot. Detection of glacier calving margins with convolutional neural networks: A case study. *Remote Sensing*, 11(1):74, 2019.

Susana Nascimento and Pedro Franco. Segmentation of upwelling regions in sea surface temperature images via unsupervised fuzzy clustering. In *International Conference on Intelligent Data Engineering and Automated Learning*, pages 543–553. Springer, 2009a.

Susana Nascimento and Pedro Franco. Unsupervised fuzzy clustering for the segmentation and annotation of upwelling regions in sea surface temperature images. In *International Conference on Discovery Science*, pages 212–226. Springer, 2009b.

K Nieto, Hervé Demarcq, and S McClatchie. Mesoscale frontal structures in the canary upwelling system: New front and filament detection algorithms applied to spatial and temporal patterns. *Remote Sensing of Environment*, 123:339–346, 2012.

Nikos Nikolaou and Nikos Papamarkos. Color reduction for complex document images. *International Journal of Imaging Systems and Technology*, 19(1):14–26, 2009.

Xuerui Niu, Qiaolin Zeng, Xiaobo Luo, and Liangfu Chen. Fcau-net for the semantic segmentation of fine-resolution remotely sensed images. *Remote Sensing*, 14(1):215, 2022.

Leo Nykjær and Lieve Van Camp. Seasonal and interannual variability of coastal upwelling along northwest africa and portugal from 1981 to 1991. *Journal of Geophysical Research: Oceans*, 99(C7):14197–14207, 1994.

LEO NYKJAER and LIEVE VANCAMP. Seasonal sst and upwelling indices along the northwest african coast. *ESA, Environment Observation and Climate Modelling Through International Space Projects.*, 1, 1992.

James J O'Brien and HE Hurlburt. A numerical model of coastal upwelling. *Journal of Physical Oceanography*, 2(1):14–26, 1972.

John J Oram, James C McWilliams, and Keith D Stolzenbach. Gradient-based edge detection and feature classification of sea-surface images of the southern california bight. *Remote Sensing of Environment*, 112(5):2397–2415, 2008.

Nobuyuki Otsu. A threshold selection method from gray-level histograms. *IEEE transactions on systems, man, and cybernetics*, 9(1):62–66, 1979.

Nikhil R Pal and Sankar K Pal. A review on image segmentation techniques. *Pattern recognition*, 26(9):1277–1294, 1993.

C Parkinson and E Wollack. Tour of the electromagnetic spectrum. *NASA, Winner*, 22, 2010.

JL Pelegrí, A Marrero-Díaz, A Ratsimandresy, A Antoranz, J Cisneros-Aguirre, C Gordo, D Grisolía, A Hernández-Guerra, I Láiz, A Martínez, et al. Hydrographic cruises off northwest africa: the canary current and the cape ghir region. *Journal of Marine Systems*, 54(1-4):39–63, 2005.

Anders Persson. The coriolis effect. *History of Meteorology*, 2:1–24, 2005.

Joël Picaut. Propagation of the seasonal upwelling in the eastern equatorial atlantic. *Journal of Physical Oceanography*, 13(1):18–37, 1983.

Claire Pottier. *Combinaison multi-capteurs de données de couleur de l'eau: application en océanographie opérationnelle.* PhD thesis, Université Paul Sabatier-Toulouse III, 2006.

Claire Pottier, Antonio Turiel, and Véronique Garçon. Inferring missing data in satellite chlorophyll maps using turbulent cascading. *Remote Sensing of Environment*, 112(12):4242–4260, 2008.

NAA Rayner, De E Parker, EB Horton, Chris K Folland, Lisa V Alexander, DP Rowell, Elizabeth C Kent, and A Kaplan. Global analyses of sea surface temperature, sea ice, and night marine air temperature since the late nineteenth century. *Journal of Geophysical Research: Atmospheres*, 108(D14), 2003.

Eun Joo. Rhee. A deep learning approach for classification of cloud image patches on small datasets. *Journal of information and communication convergence engineering*, pages 173–178, 2018.

Craig M Risien and Dudley B Chelton. A global climatology of surface wind and wind stress fields from eight years of quikscat scatterometer data. *Journal of Physical Oceanography*, 38(11):2379–2413, 2008.

O Ronneberger, P Fischer, and T Brox. Convolutional networks for biomedical image segmentation. In *Medical Image Computing and Computer-Assisted Intervention–MICCAI 2015 Conference Proceedings*, 2022.

Olaf Ronneberger, Philipp Fischer, and Thomas Brox. U-net: Convolutional networks for biomedical image segmentation. In *International Conference on Medical image computing and computer-assisted intervention*, pages 234–241. Springer, 2015.

Digna T Rueda-Roa and Frank E Muller-Karger. The southern caribbean upwelling system: Sea surface temperature, wind forcing and chlorophyll concentration patterns. *Deep Sea Research Part I: Oceanographic Research Papers*, 78:102–114, 2013.

John H Ryther. Photosynthesis and fish production in the sea: The production of organic matter and its conversion to higher forms of life vary throughout the world ocean. *Science*, 166(3901):72–76, 1969.

A Miguel P Santos, Alexander S Kazmin, and Alvaro Peliz. Decadal changes in the canary upwelling system as revealed by satellite observations: Their impact on productivity. *Journal of Marine Research*, 63(2):359–379, 2005.

F Santos, M Gómez-Gesteira, M DeCastro, and I Álvarez. Upwelling along the western coast of the iberian peninsula: dependence of trends on fitting strategy. *Climate Research*, 48(2-3):213–218, 2011.

F Santos, M Gomez-Gesteira, M Decastro, and I Alvarez. Differences in coastal and oceanic sst trends due to the strengthening of coastal upwelling along the benguela current system. *Continental Shelf Research*, 34:79–86, 2012.

Adem Tuncer Sardogan, Melike and Yunus Ozen. Plant leaf disease detection and classification based on cnn with lvq algorithm. In *international conference on computer science and engineering (UBMK)*. IEEE, 2018.

Robert A Schowengerdt. *Remote sensing: models and methods for image processing*. elsevier, 2006.

Jean Serra. Image analysis and mathematical morphol-ogy. *(No Title)*, 1982.

Jean Serra and Pierre Soille. *Mathematical morphology and its applications to image processing*, volume 2. Springer Science & Business Media, 2012.

Kenneth Sherman and Gotthilf Hempel. The unep large marine ecosystem report: A perspective on changing conditions in lmes of the world's regional seas. 2008.

Jiancheng Shi, Yang Du, Jinyang Du, LingMei Jiang, LinNa Chai, KeBiao Mao, Peng Xu, WenJian Ni, Chuan Xiong, Qiang Liu, et al. Progresses on microwave remote sensing of land surface parameters. *Science China Earth Sciences*, 55: 1052–1078, 2012.

Yus Sholva, Benhard Sitohang, and Ketut Wikantika. New approach to locate upwelling and thermal-front from satellite imagery data. *Procedia Technology*, 11:317–326, 2013.

Jamie Shotton, Matthew Johnson, and Roberto Cipolla. Semantic texton forests for image categorization and segmentation. In *2008 IEEE conference on computer vision and pattern recognition*, pages 1–8. IEEE, 2008.

R Sivagami, J Srihari, and KS Ravichandran. Analysis of encoder-decoder based deep learning architectures for semantic segmentation in remote sensing images. In *Intelligent Systems Design and Applications: 18th International Conference* *on Intelligent Systems Design and Applications (ISDA 2018) held in Vellore, India, December 6-8, 2018, Volume 2*, pages 332–341. Springer, 2020a.

S Sivagami, P Chitra, G Sri Ram Kailash, and SR Muralidharan. Unet architecture based dental panoramic image segmentation. In *2020 International Conference on Wireless Communications Signal Processing and Networking (WiSPNET)*, pages 187–191. IEEE, 2020b.

Mohamed Snoussi, Ayoub Tamim, Salma El Fellah, and Mohamed El Ansari. Deep residual u-net for automatic detection of moroccan coastal upwelling using sst images. *Multimedia Tools and Applications*, 82(5):7491–7507, 2023.

Fatima M Sousa, Susana Nascimento, Hugo Casimiro, and Dmitri Boutov. Identification of upwelling areas on sea surface temperature images using fuzzy clustering. *Remote Sensing of Environment*, 112(6):2817–2823, 2008.

P Speth. Meteorological influences on upwelling off northwest africa. *Rapp. P.-V. Reun. Cons. Int. Explor. Mer*, 180:29–34, 1982.

P Speth and A Köhne. The relationship between sea surface temperatures and winds off northwest africa and portugal. *Océanographie tropicale*, 18(1):69–80, 1983.

Robert H Stewart. *Introduction to physical oceanography.* Robert H. Stewart, 2008.

Volker H Strass. Chlorophyll patchiness caused by mesoscale upwelling at fronts. *Deep Sea Research Part A. Oceanographic Research Papers*, 39(1):75–96, 1992.

Ayoub Tamim. *Segmentation et classification des images satellitaires: application à la détection des zones dâupwelling côtier marocain et mise en place dâun logiciel de suivi spatiotemporel.* PhD thesis, UNIVERSITÉ MOHAMMED V FACULTÉ DES SCIENCES Rabat, 2015.

Ayoub Tamim, Khalid Minaoui, Khalid Daoudi, Hussein Yahia, Abderrahman Atillah, Mohammed Faouzi Smiej, and Driss Aboutajdine. A simple and efficient approach for coarse segmentation of moroccan coastal upwelling. In *21st European Signal Processing Conference (EUSIPCO 2013)*, pages 1–5. IEEE, 2013.

Ayoub Tamim, Khalid Minaoui, Khalid Daoudi, Abderrahman Atillah, and Driss Aboutajdine. On detectability of moroccan coastal upwelling in sea surface temperature satellite images. In *International Symposium on Visual Computing*, pages 386–395. Springer, 2014a.

Ayoub Tamim, Khalid Minaoui, Khalid Daoudi, Abderrahman Atillah, Hussein Yahia, and Driss Aboutajdine. Upwelling detection in sst images using fuzzy clustering with adaptive cluster merging. In *ISIVC 2014*, 2014b.

Ayoub Tamim, Khalid Minaoui, Khalid Daoudi, Abderrahman Atillah, Hussein Yahia, Driss Aboutajdine, and Mohammed Faouzi Smiej. A simple tool for automatic extraction of moroccan coastal upwelling from sea surface temperature images. In *2014 9th International Conference on Intelligent Systems: Theories and Applications (SITA-14)*, pages 1–4. IEEE, 2014c.

Ayoub Tamim, Khalid Minaoui, Khalid Daoudi, Hussein Yahia, Abderrahman Atillah, and Driss Aboutajdine. An efficient tool for automatic delimitation of moroccan coastal upwelling using sst images. *IEEE Geoscience and Remote Sensing Letters*, 12(4):875–879, 2014d.

Ayoub Tamim, Khalid Minaoui, Khalid Daoudi, Abderrahman Atillah, and Driss Aboutajdine. Detection of moroccan coastal upwelling in sst images using the expectation-maximization. In *2015 Intelligent Systems and Computer Vision (ISCV)*, pages 1–5. IEEE, 2015.

Ayoub Tamim, Khalid Minaoui, Khalid Daoudi, Hussein Yahia, Abderrahman Atillah, Salma El Fellah, Driss Aboutajdine, and Mohamed El Ansari. Automatic detection of moroccan coastal upwelling zones using sea surface temperature images. *International Journal of Remote Sensing*, 40(7):2648–2666, 2019.

Kevin E Trenberth, William G Large, and Jerry G Olson. The mean annual cycle in global ocean wind stress. *Journal of Physical Oceanography*, 20(11):1742–1760, 1990.

Charles Troupin. Study of the cape ghir upwelling filament using variational data analysis and regional numerical model. 2011.

Charles Troupin, Evan Mason, Jean-Marie Beckers, and Pablo Sangrà. Generation of the cape ghir upwelling filament: A numerical study. *Ocean Modelling*, 41: 1–15, 2012.

Ilter Türkmenli, Erchan Aptoula, and Koray Kayabol. Superpixel based graph convolutional neural network for sar image segmentation. In *Image and Signal Processing for Remote Sensing XXVII*, volume 11862, pages 148–153. SPIE, 2021.

Tanya S Unger Holtz. Introductory digital image processing: A remote sensing perspective, 2007.

L Van Camp, L Nykjaer, E Mittelstaedt, and P Schlittenhardt. Upwelling and boundary circulation off northwest africa as depicted by infrared and visible satellite observations. *Progress in Oceanography*, 26(4):357–402, 1991.

JJ Walker, KM De Beurs, RH Wynne, and Feng Gao. Evaluation of landsat and modis data fusion products for analysis of dryland forest phenology. *Remote Sensing of Environment*, 117:381–393, 2012.

Frank J Wentz. Measurement of oceanic wind vector using satellite microwave radiometers. *IEEE Transactions on Geoscience and Remote Sensing*, 30(5): 960–972, 1992.

Warren S Wooster, Andrew Bakun, and Douglas R McLain. The seasonal upwelling cycle along the eastern boundary of the north atlantic. 1976.

Klaus Wyrtki. An estimate of equatorial upwelling in the pacific. *Journal of Physical Oceanography*, 11(9):1205–1214, 1981.

Guiying Yang, Xiaomin Ye, Qing Xu, Xiaobin Yin, and Siyang Xu. Sea surface chlorophyll-a concentration retrieval from hy-1c satellite data based on residual network. *Remote Sensing*, 15(14):3696, 2023.

Lequan Yu, Hao Chen, Qi Dou, Jing Qin, and Pheng-Ann Heng. Automated melanoma recognition in dermoscopy images via very deep residual networks. *IEEE transactions on medical imaging*, 36(4):994–1004, 2016.

Yanwu Zhang, Michael A Godin, James G Bellingham, and John P Ryan. Using an autonomous underwater vehicle to track a coastal upwelling front. *IEEE Journal of Oceanic Engineering*, 37(3):338–347, 2012.

Hengshuang Zhao, Jianping Shi, Xiaojuan Qi, Xiaogang Wang, and Jiaya Jia. Pyramid scene parsing network. In *Proceedings of the IEEE conference on computer vision and pattern recognition*, pages 2881–2890, 2017.

ROYAUME DU MAROC
Université Mohammed V
- RABAT -
جامعة محمد الخامس
– الرباط –
Faculté des sciences
كلية العلوم

CENTRE D'ETUDES DOCTORALES - SCIENCES ET TECHNOLOGIES

Résumé

L'analyse des processus physiques au sein d'un système d'upwelling est essentielle pour comprendre sa variabilité actuelle ainsi que ses évolutions passées et futures. Ce phénomène naturel, modué par des variables dynamiques, fait partie intégrante de la régulation des conditions océaniques et du maintien des ressources marines vitales. Parallélement, les progrés de l'intelligence artificielle et du traitement des signaux ouvrent de nouvelles voies pour une compréhension, une surveillance et une gestion plus précises et plus efficaces des sysèmes de remontée d'eau. Cette thèse pésente une recherche interdisciplinaire centrée sur la détection automatique des systémes de remontée d'eau. Elle s'appuie sur le traitement des images et des signaux et utilise diverses données provenant de différentes sources satellitaires. Les objectifs de cette étude sont les suivants: (1) Améliorer l'identification automatique et l'extraction du phénoméne de remontée des eaux le long de la côte atlantique marocaine. Pour ce faire, des algorithmes d'intelligence artificielle sont appliqués à des données satellitaires biologiques et physiques. (2) L'utilisation de l'apprentissage profond pour surveiller l'upwelling côtier dans différentes zones, en utilisant des images satellitaires de la température de surface de la mer (SST). (3) Réalisation d'une analyse statistique sur la variation spatio-temporelle de la remontée des eaux dans la région de l'Afrique du Nord-Ouest (NWA). Cela implique de proposer et d'examiner divers nouveaux indices associés à l'upwelling. Cette recherche vise à fusionner les connaissances de l'océanographie, de l'intelligence artificielle, du traitement des images et du traitement des signaux pour favoriser une compréhension globale des systèmes d'upwelling et de leurs impacts à multiples facettes.

Mots clés : Système d'upwelling, Traitement d'image, Intelligence artificielle, côte atlantique Marocaine, Extraction automatique de l'upwelling, température de surface de la mer, Traitement de signal, Nouveaux Indices.

Abstract

Analyzing the physical processes within an upwelling system is pivotal for comprehending its current variability as well as its past and future developments. This natural phenomenon, modulated by dynamic variables, is integral to regulating oceanic conditions and maintaining vital marine resources. Concurrently, advancements in artificial intelligence and signal processing are forging new paths for a more precise and efficient understanding, monitoring, and management of upwelling systems. This thesis introduces interdisciplinary research centered on the automatic detection of upwelling systems. It leverages image and signal processing and utilizes diverse data from various satellite sources. The goals of this study include: (1) Enhancing the automatic identification and extraction of the upwelling phenomenon along the Moroccan Atlantic coast. This is achieved by applying artificial intelligence algorithms to biological and physical satellite data. (2) Employing deep learning to monitor coastal upwelling in different areas, utilizing satellite images of sea surface temperature (SST). (3) Conducting statistical analysis on the spatio-temporal variation of upwelling in the North West Africa (NWA) region. This involves proposing and scrutinizing various new indices associated with upwelling. This research aims to amalgamate insights from oceanography, artificial intelligence, image processing, and signal processing to foster a comprehensive understanding of upwelling systems and their multifaceted impacts.

Keywords: Upwelling system, Image processing, Artificial intelligence, Moroccan Atlantic coast, Automatic extraction of the upwelling, Sea surface temperature, Signal processing, New indices.

✉ Faculté des Sciences, avenue Ibn Battouta, BP. 1014 RP, Rabat –Maroc
☎ 00212 (05) 37 77 18 76 📠 00212(05) 37 77 42 61; http://www. fsr.um5.ac.ma